2020

Gating Mechanism Comparison Between The Trkah And Mthk Ion Channels

Valentina Simeonova Dimitrova
University of Pennsylvania

Recommended Citation

Dimitrova, Valentina Simeonova, "Gating Mechanism Comparison Between The Trkah And Mthk Ion Channels" (2020). *Publicly Accessible Penn Dissertations*. 4054.
https://repository.upenn.edu/edissertations/4054

Gating Mechanism Comparison Between The Trkah And Mthk Ion Channels

Abstract

TrkAH and MthK are bacterial ligand-gated K+ channels with no sequence similarity and remarkably different structural and functional properties. TrkAH has a two-pore module with non-zero basal open probability that can be up- or downregulated in response to cytosolic ATP or ADP, respectively. In MthK, the open probability of a single pore is increased from zero to one by cytosolic Ca2+. Due to their different pore and selectivity filter architectures, the two channels are predicted to have distinct gating mechanisms. The only common feature between TrkAH and MthK is that in each system the effect of ligand on the open probability is exerted through a cytosolic regulatory module, composed of eight structurally conserved Regulator of Conductance for K+ (RCK) motifs, harboring the ligand binding sites. We hypothesized that, despite their pronounced differences, TrkAH and MthK have similar gating energetics, dictated by the primary involvement of their RCK motifs in ligand recognition and pore regulation. To test this hypothesis, we studied the energetics of ligand-induced conformational changes of individual RCK motifs in each regulatory module by implementing a recently reported single-molecule fluorescence-based technique, in which the conformational state of a target protein is deduced from the measured polarization of a bifunctional rhodamine fluorophore attached to a suitable reporter a-helix. From the RCK energetics in each regulatory module we derived an analytic model, which quantitatively predicts the experimentally observed ligand dependence of each channel's open probability. Our findings demonstrate that, in each regulatory module type, the structurally conserved RCK motif visits one of three states with comparable probabilities, related by similar equilibrium constants, thus exhibiting essentially the same intrinsic energetics in Trk as in MthK. Furthermore, the gating energetics of each system are governed by a unifying principle, whereby the channel's opening is conditioned upon a particular combination of RCK subunit states and ligand binding affects the probability of observing this combination by regulating the degree of inter-subunit coupling.

Degree Type

Dissertation

Degree Name

Doctor of Philosophy (PhD)

Graduate Group

Biochemistry & Molecular Biophysics

First Advisor

Zhe Lu

Keywords

fluorescence polarization, MthK, potassium ion channel, RCK, single-molecule, TrkAH

Subject Categories

Biochemistry | Biophysics

GATING MECHANISM COMPARISON BETWEEN THE TRKAH AND MTHK ION CHANNELS

Valentina S. Dimitrova

A DISSERTATION

in

Biochemistry and Molecular Biophysics

Presented to the Faculties of the University of Pennsylvania

in

Partial Fulfillment of the Requirements for the

Degree of Doctor of Philosophy

2020

Supervisor of Dissertation

____

Zhe Lu, M.D., Ph.D., Professor of Physiology

Graduate Group Chairperson

____

Kim A. Sharp, Ph.D., Associate Professor of Biochemistry and Biophysics

Dissertation Committee

Brian M. Salzberg, Ph.D., Professor of Neuroscience and Physiology

Gregory D. Van Duyne, Ph.D., Jacob Gershon-Cohen Professor of Medical Science

Toshinori Hoshi, Ph.D., Professor of Physiology

Kenton J. Swartz, Ph.D., Senior Investigator, Molecular Physiology and Biophysics Section, Porter Neuroscience Research Center, National Institute of Neurological Disorders and Stroke, National Institute of Health

To my family, my mentors, and my friends

ACKNOWLEDGMENTS

It has been an honor to pursue my Ph.D. degree at the University of Pennsylvania, an institution with an established reputation for supporting exceptional scientific research. I am particularly grateful to the Department of Biochemistry and Biophysics at the Perelman School of Medicine for admitting me into its graduate program and trusting me with the immense responsibility of measuring up to its high standards of scientific excellence. Most of all, I am thankful for the opportunity to learn from the most brilliant, kind and supportive scientists I have ever had the pleasure of knowing.

My training in the laboratory of Dr. Zhe Lu has been both highly demanding and incredibly rewarding. Dr. Lu's unique mentoring style has emphasized the importance of scientific rigor and intellectual independence, teaching me to remain confident while facing the many unknowns that saturate a researcher's daily existence. My countless interactions with the members of the Lu Lab have helped me reach emotional maturity by balancing my eagerness with patience, my perfectionism with practicality and my childlike enthusiasm with structure and discipline. Importantly, in the Lu Lab I have obtained extensive training in a range of challenging techniques with the instrumental involvement of Drs. Yufeng (Fenny) Zhou and John Lewis. While Fenny generously shared with me her vast knowledge in the field of protein biochemistry, John has expertly guided me through the complex field of single-molecule research and has been indispensable for my growth as a scientist and for the completion of this thesis.

The interactive environment, fostered at the Perelman School of Medicine, has allowed me to gain wisdom from multiple experienced scientists and build many lasting friendships with fellow graduate students. The members of my thesis committee Drs. Brian Salzberg, Gregory Van Duyne and Toshinori Hoshi, have enthusiastically encouraged my research efforts over the years. My conversations with Drs. Carol Deutch, Steve Baylor, Yale Goldman, Jody Dantzig and Kim Sharp have made me feel like a valuable part of the Penn scientific community. Finally, my friends Shufei (Sophie) Mostert, Gözde Eskici, Delaine Zayas-Bazán Burgos and Melina Gyparaki have inspired me to be a proud and confident female biophysicist and taught me the importance of taking a few moments to relax and bond with my peers.

I have been blessed with an incredibly supportive family who kept me humble in times of success and motivated during the occasional bouts of struggle and exhaustion. My parents Alla Dimitrova and Simeon Dimitrov have instilled in me the empowering belief that anything is possible through hard work and dedication. My brother Evgeni Dimitrov has provided me with lots of pragmatic advice to help me navigate the Ph.D. experience rationally and level-headedly. Most importantly, I want to thank my husband Alejandro Curiel, for keeping me strong and optimistic with his love, wisdom, humor and patience.

ABSTRACT

GATING MECHANISM COMPARISON BETWEEN THE TRKAH AND MTHK ION CHANNELS

Valentina S. Dimitrova

Zhe Lu, M.D., Ph.D.

TrkAH and MthK are bacterial ligand-gated K^+ channels with no sequence similarity and remarkably different structural and functional properties. TrkAH has a two-pore module with non-zero basal open probability that can be up- or downregulated in response to cytosolic ATP or ADP, respectively. In MthK, the open probability of a single pore is increased from zero to one by cytosolic Ca^{2+}. Due to their different pore and selectivity filter architectures, the two channels are predicted to have distinct gating mechanisms. The only common feature between TrkAH and MthK is that in each system the effect of ligand on the open probability is exerted through a cytosolic regulatory module, composed of eight structurally conserved Regulator of Conductance for K^+ (RCK) motifs, harboring the ligand binding sites. We hypothesized that, despite their pronounced differences, TrkAH and MthK have similar gating energetics, dictated by the primary involvement of their RCK motifs in ligand recognition and pore regulation. To test this hypothesis, we studied the energetics of ligand-induced conformational changes of individual RCK motifs in each regulatory module by implementing a recently reported single-molecule fluorescence-based technique, in which the conformational state of a target protein is deduced from the measured polarization of a bifunctional rhodamine fluorophore attached to a suitable reporter α-helix. From the RCK energetics in each regulatory module we derived an analytic model, which quantitatively predicts the experimentally observed ligand dependence of each channel's open probability. Our

findings demonstrate that, in each regulatory module type, the structurally conserved RCK motif visits one of three states with comparable probabilities, related by similar equilibrium constants, thus exhibiting essentially the same intrinsic energetics in Trk as in MthK. Furthermore, the gating energetics of each system are governed by a unifying principle, whereby the channel's opening is conditioned upon a particular combination of RCK subunit states and ligand binding affects the probability of observing this combination by regulating the degree of inter-subunit coupling.

TABLE OF CONTENTS

LIST OF TABLES

LIST OF ILLUSTRATIONS

LIST OF MAIN EQUATIONS USED

CHAPTER 1: INTRODUCTION

1.1 Bacterial potassium homeostasis

Potassium (K^+) is the major inorganic cation in living cells. Universally, K^+ is more concentrated in the cytosol than the immediate surroundings of cells. This concentration disparity is essential for life on Earth and perhaps arose very early in evolution, soon after macromolecules and phosphates were first enclosed in small lipid-bound compartments (Armstrong, 2015). In bacteria, K^+ is typically ~10^3 times more concentrated inside than outside the cell, thus contributing to an osmotic imbalance that gives rise to an outwardly directed turgor pressure, required for cellular growth, shape maintenance, and ultimately, survival (Schultz and Solomon, 1961). In addition to being critical for the structural integrity of bacteria, K^+ is an important regulator of intracellular processes as it activates proteins involved in cellular adaptation, and controls intracellular pH by displacing protons from the various cytosolic buffer anions, mainly nucleic acids and negatively charged amino acid residues (Epstein, 2003).

In prokaryotes, the transmembrane K^+ ratio must be dynamically regulated to ensure adequate adaptation to unpredictable environmental changes such as sudden floods, droughts, nutrient deprivation or chemical stimulation. K^+ must therefore be able to traverse the membrane in a controlled manner. Since the cell membrane is a dielectric, the direct passage of K^+ is extremely energetically costly. Instead, transmembrane K^+ flux is facilitated by specialized membrane-embedded proteinaceous pores that connect the cell interior and exterior (Hille, 2001; Figure 1.1A). Most such K^+-conducting pores are selective for K^+ relative to other biologically relevant cations. Importantly, each pore exhibits at least two states, open and closed. In the open state, K^+ passage through the pore is permitted, and in the closed state, K^+ passage is denied. Thus, the membrane's overall K$^+$ conductance can be adjusted by regulating the open probability of K$^+$-selective pores. By regulating K$^+$ flux across the cell membrane, bacteria can tune their turgor pressure, cytosolic pH, metabolic rate and gene expression to meet the current environmental demands.

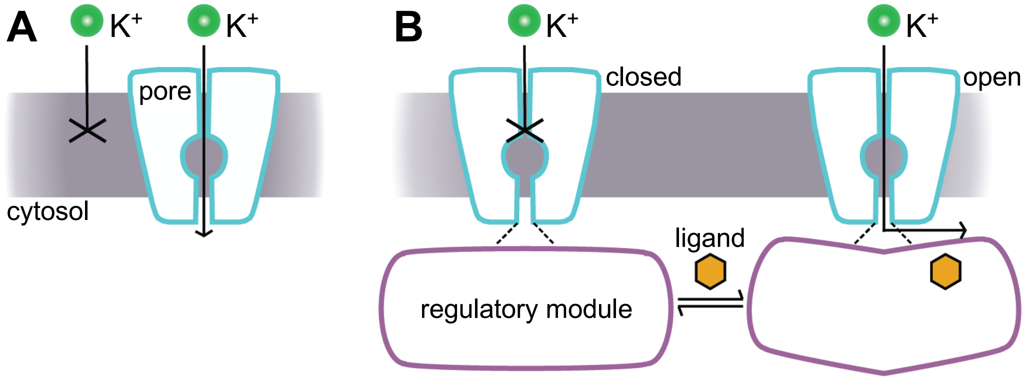

Figure 1. 1 – Basic principle of ligand-gated K$^+$-selective systems in bacteria

(A) A proteinaceous pore is necessary to facilitate K$^+$ passage across the cell membrane. **(B)** In ligand-gated K$^+$ channels, the opening of the pore module is controlled by ligand-induced conformational changes in an associated cytosolic regulatory module.

Prokaryotes address many different problems with the same general approach of altering the membrane K$^+$ conductance. In order to tailor this general approach to the specific challenge faced by the cell, various K$^+$-selective systems exist with different architecture, conductance, kinetics and regulation. These systems employ fundamentally similar pore modules, but differ in the type of stimulus that leads to pore opening. Most prokaryotic K$^+$-selective systems open in response to a chemical stimulus sensed via a cytosolic regulatory module abutting the pore module (Figure 1.1B). By undergoing ligand-induced conformational changes the regulatory module can exert force on the pore and control its opening. Commonly, such bacterial regulatory modules are assembled from Regulator of Conductance for K$^+$ (RCK) units.

1.2 Multimeric assemblies of RCK units

The RCK unit is a common building block in the regulatory modules for most prokaryotic and some eukaryotic ligand-gated K^+-selective pores (Jiang et al., 2001). The RCK unit has three essential properties: (1) it contains key interfaces for homo-oligomerization and pore docking; (2) it can interact with a specific ligand; and (3) it can change conformation upon ligand binding. Equipped with these main attributes, RCK units can, in a ligand-specific fashion, convert the chemical energy of ligand binding into mechanical work to open the associated pore module.

RCK units assemble into functionally relevant homo-oligomers (Albright et al., 2006; Cao et al., 2013; Hite et al., 2017; Jiang et al., 2002a; Kong et al., 2012; Roosild et al., 2009; Vieira-Pires et al., 2013). All RCK units contain a structurally conserved N-terminal motif, henceforth referred to as the *RCK motif*, and a variable C-terminal region (Figure 1.2A). The RCK motif is comprised of a ligand-binding globular core and a rigid hinge helix. RCK units form domain-swapped homodimers, whereby the hinge helix of the first RCK motif associates with the core of the second RCK motif and vice versa (Dong et al., 2005; Jiang et al., 2001; Roosild et al., 2002; Figure 1.2B, C). Between the two RCK cores, a cleft is formed cradling the two ligand binding sites. The RCK dimer interface is stabilized by a so-called peripheral subdomain in many cases constructed from the nonconserved C-terminal portions of the dimerized RCK units themselves and in some instances provided by a separate protein. For an RCK dimer, a plane can be imagined that contains the roughly coplanar centers of gravity of the two RCK unit cores and the peripheral subdomain; we will refer to this plane as the *dimer plane*.

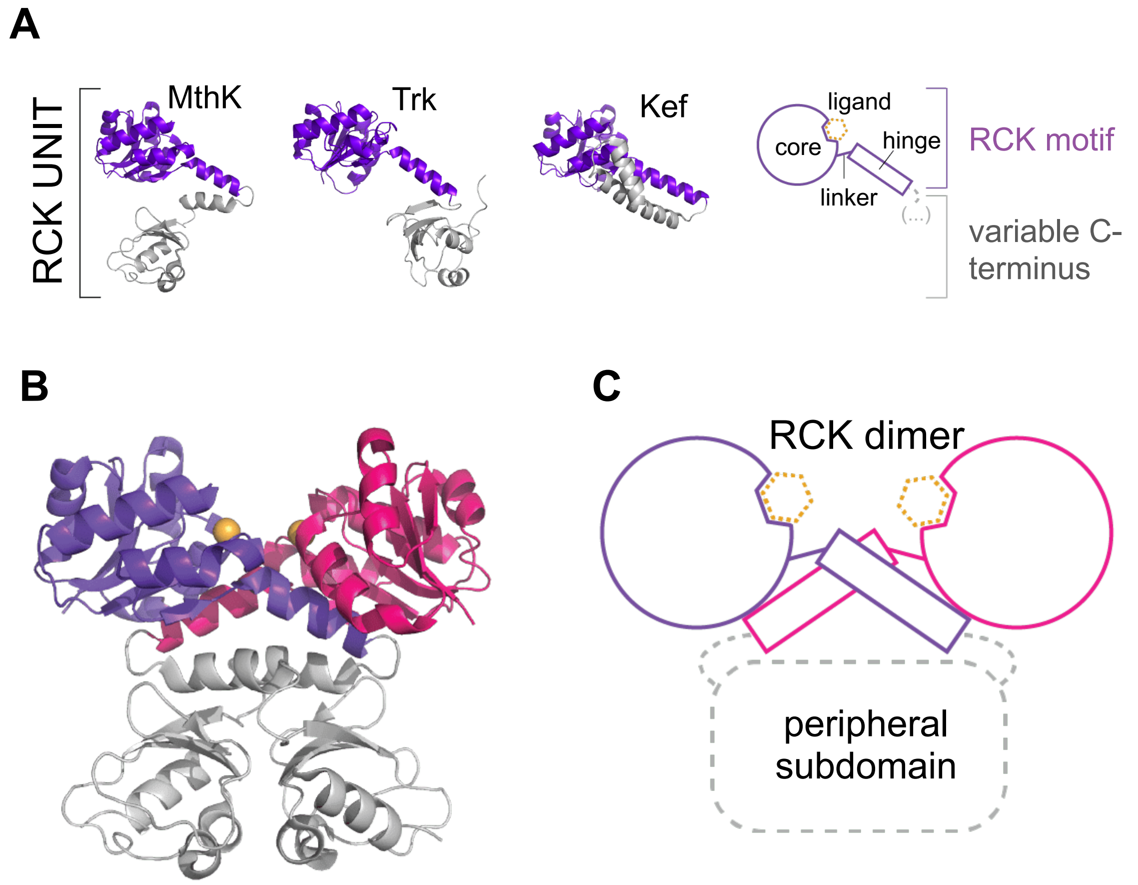

Figure 1. 2 – The RCK unit

(A) Cartoon models for the atomic resolution structures of the MthK, Trk and Kef RCK units, generated from PDB codes 4J9U, 1lnq and 3eyw, respectively. **(B)** Structure of the Ca^{2+}-bound RCK dimer from MthK (PDB: 1lnq). The Ca^{2+} ions' van der Waals diameters are exaggerated for illustration purposes. (C) Schematic diagram of the RCK dimer.

To build the fully operational regulatory module, 4 RCK dimers assemble in a ring configuration through core/core connections, placing all 8 ligand binding sites along the inner circumference (Figure 1.3A). The centers of gravity of the 4 dimers define a transverse plane, which divides the ring into identical top and bottom halves. Each dimer plane is tilted at ~45° relative to the transverse plane, so the top ring half contains 4 RCK unit cores and the bottom half contains the cores of the respective dimerization partners. For clarity, we will refer to two interacting RCK units as *sisters* when they belong to the same dimer, and *neighbors* when they engage in an interdimer connection. Hence, within the functional RCK octamer each RCK core participates in two distinct types of interfaces: a core/hinge-helix interface with a sister RCK unit and a core/core interface with a neighbor RCK unit. In addition, a subset of the RCK cores also interacts with the pore module, covalently or through a shared interface, as the pore docks onto the regulatory module with the ion permeation pathway perpendicular to the ring's transverse plane (Figure 1.3B). The peripheral subdomains are evenly positioned around the outer ring perimeter and do not interact with the pore directly.

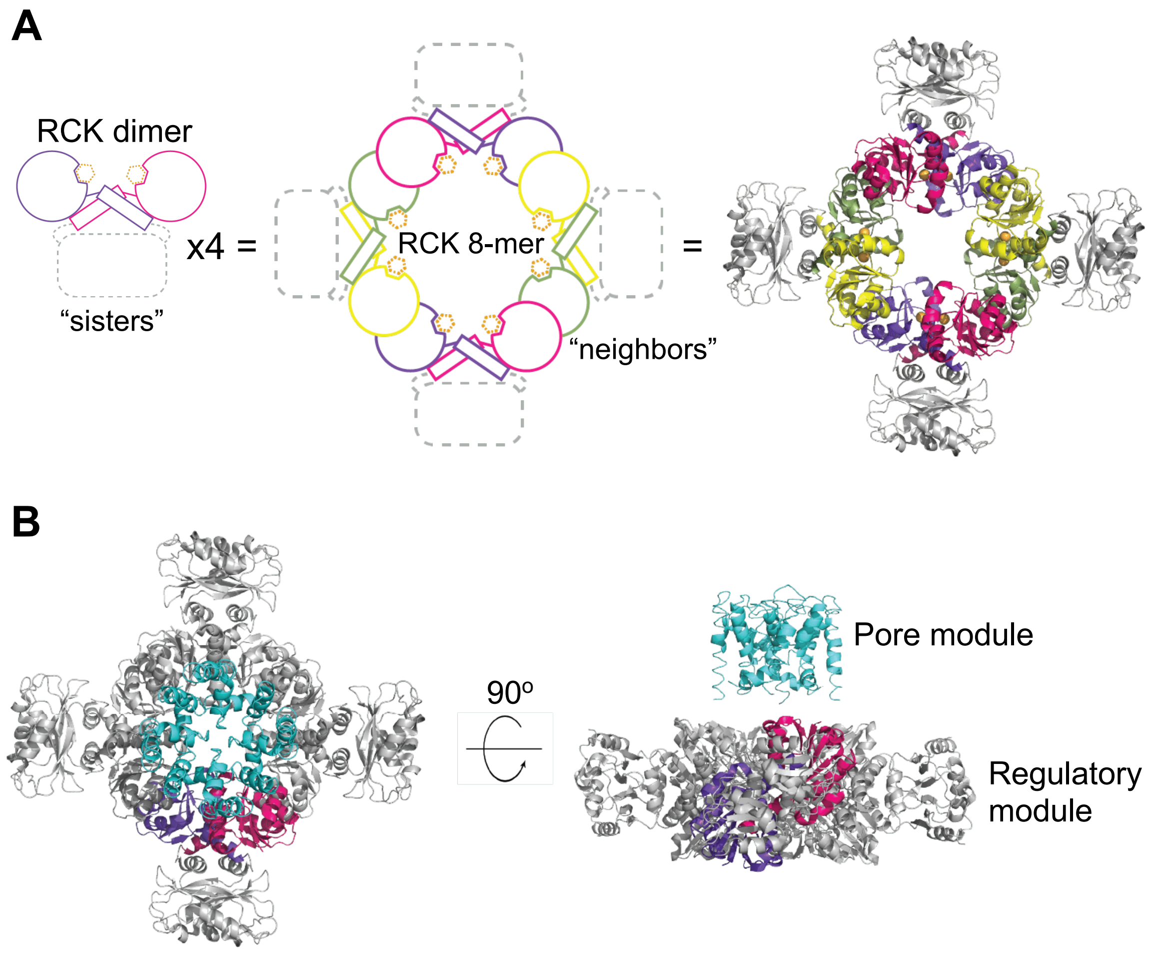

Figure 1. 3 – Multimeric assemblies of RCK units

(A) Four RCK dimers assemble the functional regulatory module; "sister" RCK units participate in domain-swap interactions and "neighbor" RCK units experience core-core interactions. **(B)** Atomic resolution structure for the whole MthK ion channel (PDB: 1lnq).

1.3 Ligand-induced conformational changes in RCK oligomers

The RCK motif consists of six α-helices (αA-F) and six β-strands (βA-F) in a characteristic three-dimensional arrangement, whereby an αβ core and a rigid hinge helix are linked via a short flexible linker. The αβ core exhibits a Rossmann fold with a six-stranded parallel β-sheet bordered by two α-helices on one side (αA and αB) and three α-helices on the other (αC, αD and αE) (Rao and Rossmann, 1973; Shin and Kihara, 2019; Figure 1.4).

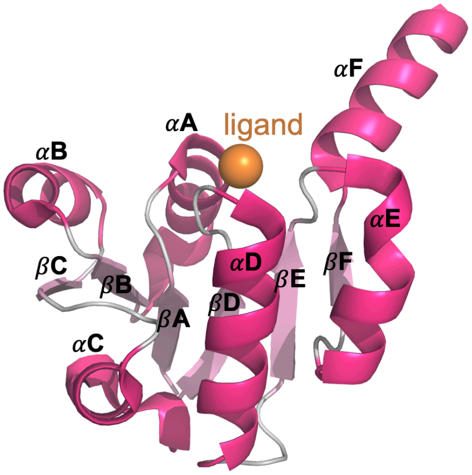

Figure 1. 4 – RCK motif ligand binding site

Ca^{2+}-bound RCK motif from MthK (PDB: 1lnq), illustrating the typical Rossmann fold of RCKs. The Ca^{2+} ion's van der Waals diameter is exaggerated for illustration purposes.

The N-terminal tips of αA-E and the C-terminal tips of βA-F point towards the ligand binding site, and together with their connecting loops, confer ligand specificity to the binding pocket. The functionally relevant ligand type varies depending on the regulatory module considered (Table 1.1). The N-terminal half of the RCK motif (strands βA-D and helices αA and αB) is an ancient core topology, commonly found in dehydrogenase enzymes, where it is the minimum structure necessary to bind nicotinamide dinucleotide (Bellamacina, 1996). In dehydrogenases, the first 30-35 amino acids of the core topology comprise a fingerprint region with several conserved residues involved in co-factor binding, among which a phosphate binding consensus sequence GXGXXG. Although the fingerprint region is not always conserved in RCK motifs, many of its features tend to be present in RCK motifs that bind nucleotides. Particularly, the GXGXXG consensus sequence is invariably present in RCK motifs that interact with ATP or ADP.

The hinge helix (αF) radiates away from the core and intercalates with the core of a sister RCK motif, thus forming the canonical RCK dimer (RCK1-RCK2) with significant conformational flexibility (Table 1.1). At least two RCK dimer states exist that differ in the magnitude of the αF1-αF2 angle and the width of the intradimer cleft (Figure 1.5). Ligand-induced conformational changes in RCK dimers rely on the ligand's ability to bias the RCK dimer equilibrium towards a particular state. In at least some cases, ligand binding can also couple or uncouple sister RCK units (Vieira-Pires et al., 2013).

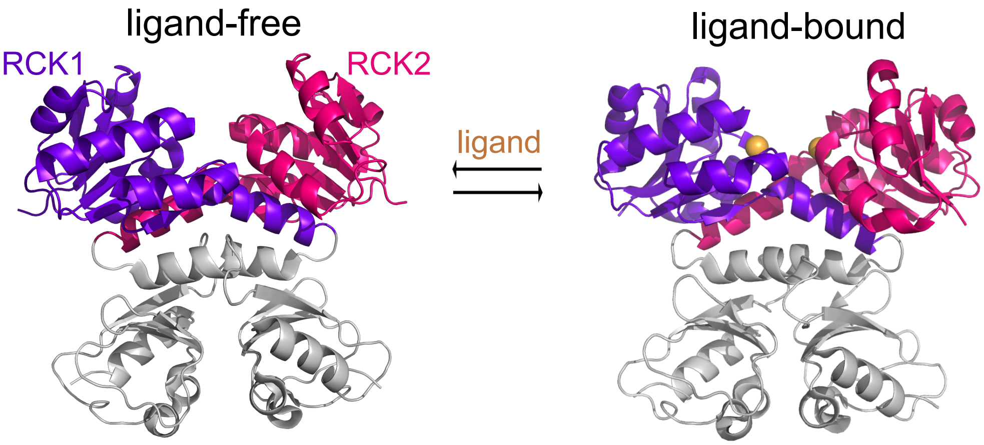

Figure 1. 5 – Ligand-induced conformational changes in the RCK dimer

Ca^{2+}-free (PDB: 2fy8) and Ca^{2+}-bound (PDB: 1lnq) structures of the MthK RCK dimer. The Ca^{2+} ions' van der Waals diameters are exaggerated for illustration purposes.

Table 1. 1 – Ligand-induced conformational changes in various structurally characterized RCK multimers

Angle values were obtained from structures with the following PDB codes: 2fy8, 1lnq, 4gvl, 4J9U, 4J9V, 1lss, 1lsu, 2hms, 2hmu, 2hmw, 4j7c, 4j90, 4j91, 3eyw, 3l9w, 3l9x.

K^+-selective System	Relevant Ligands	Hinge Angle Mobility Range[a]
MthK	Ca^{2+}, Ba^{2+}, H^+	129 – 138°
GsuK	ADP, NAD^+, Ca^{2+}	127°[b]
Trk	ATP, ADP, H^+	93 – 120°
Ktr	ATP, ADP, NAD^+, NADH	90 – 127°
KefC[c]	GSH, GSX[d]	128°[b]

[a] Range is defined by the lowest and highest hinge angle values calculated from known regulatory domain crystal structures

[b] Structure only available for one hinge state

[c] With the exception of KefC, all listed systems are controlled by structurally characterized octameric RCK assemblies

[d] Glutathione and glutathione derivatives

In the functional regulatory module, inter-dimer connections are established by extensive interactions between the αD and αE helices of neighbor RCK cores. In the context of the octameric RCK assembly, each inherently flexible sister RCK pair is constrained by interactions with its neighbors. To accommodate the hinge angle changes in each sister RCK pair, each dimer plane must subtly rotate around the dimer's symmetry axis. The outcome of a particular dimer plane rotation is dictated by the neighbor interface type; two major types of neighbor interfaces exist – *fixed* and *mobile*. In a fixed interdimer interface, neighbor RCK cores are stably attached to each other and behave like a rigid body that rotates concurrently with each dimer plane rotation. Conversely, a mobile interface involves looser interdimer connections that allow neighbor RCK cores to slide past each other as the dimer planes rotate.

The RCK unit is a simple structural component with built-in versatility: minor evolutionary adjustments at the ligand binding site and the neighbor interfaces can generate a large variety of structurally similar regulatory modules with different chemomechanical properties. The functional diversity of RCK octamers is best exemplified by comparing two well-studied systems: the MthK and Trk regulatory modules (Figure 1.6).

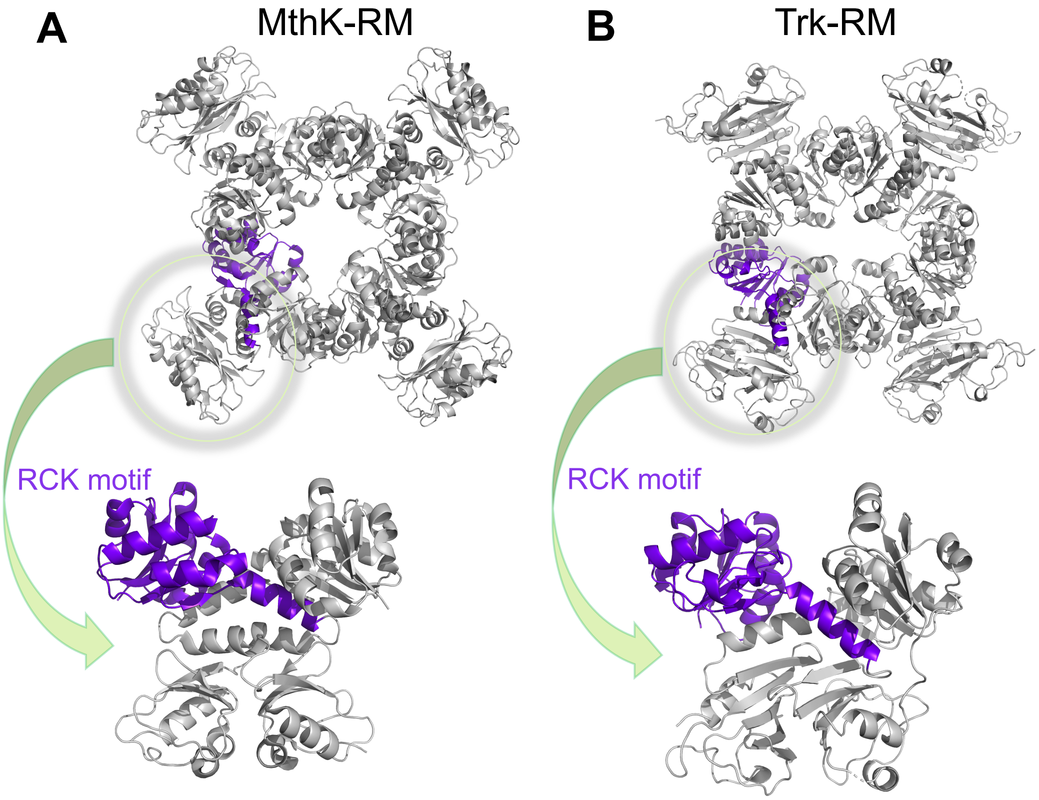

Figure 1. 6 – Structurally conserved building blocks in the MthK and Trk regulatory modules

(A) MthK regulatory module (PDB: 1lnq) and **(B)** Trk regulatory module (PDB: 4J9U) are functionally distinct gating rings, built from structurally conserved RCK motifs.

These nonhomologous regulatory modules differ greatly in terms of their structural plasticity and functional output and are only unified by their octameric RCK composition. In addition to responding to a different set of ligands (Table 1.1), each ring exhibits a unique combination of neighbor interface types: all four neighbor interfaces in the MthK ring are of the fixed type, whereas the Trk ring contains two fixed and two mobile neighbor interfaces in an alternating arrangement. Consequently, the two regulatory modules undergo remarkably different ligand-induced conformational changes. Crystallographic data suggests that Ca^{2+} induces a subtle four-fold symmetric flattening and widening in the MthK ring, while ATP induces dramatic two-fold symmetric wringing in the Trk ring (Cao et al., 2013; Ye et al., 2006). This difference in ring plasticity is consistent with the difference in function that each regulatory module performs: the MthK ring controls a single four-fold symmetric K^{+}-selective pore module, whereas the Trk ring regulates a double-pore module that is two-fold symmetric.

1.4 Thesis objective

We hypothesized that, despite their substantial differences in conformational flexibility and functional output, the Trk and MthK regulatory modules are energetically related through the RCK motif. Since each gating ring contains nearly-identical building blocks, assembled according to a set of common rules, we predicted that ligand-induced conformational changes in the two gating rings and their respective pore modules are governed by the same fundamental energetic principles. To test our prediction, we sought to answer the following three questions: (1) In each RCK octamer, what are the intrinsic energetics of an individual RCK component, in the absence or presence of ligand? (2) In each gating ring, how must an individual RCK motif energetically relate to the remaining seven, in order to generate the desired functional output, i.e. to regulate the open probability of a particular pore? (3) What are the energetic commonalities between the gating mechanisms for the Trk and MthK whole-channel systems, from an RCK-centered point of view?

A recently reported mechanistic study on the isolated MthK gating ring details the energetics of Ca^{2+}-induced conformational changes in an individual RCK motif target (Lewis and Lu, 2019b). A model is subsequently derived to relate the behavior of the observed RCK to that of the remaining RCKs in the regulatory module in a way that predicts the previously published whole-channel P_o dependence on Ca^{2+} concentration (Pau et al., 2010). Thus, questions (1) and (2) above have already been answered for the MthK system and remain unanswered for the Trk system, prompting us to perform the equivalent study on the Trk gating ring. The goals of this thesis project were to observe ATP- and ADP-induced conformational changes in an individual RCK motif in the Trk gating ring, use the findings to deduce a whole-channel gating model for Trk and compare the derived model to the already existing model for MthK.

1.5 Thesis overview

The research presented in this thesis has an experimental and a modeling component, detailed in Chapters 2 and 3, respectively. The experimental work on Trk implemented a single-molecule fluorescence-based technique for detecting angstrom-scale conformational changes in a protein target on a millisecond timescale (Lewis and Lu, 2019a). Chapter 2 presents the main experimental method and our efforts to adapt it for studies on the Trk system. Chapter 3 reports our results obtained from the complex between the Trk gating ring and pore module; based on the reported findings, a model is derived that predicts the whole-channel Trk behavior in the absence of ligand and at increasing ATP or ADP concentrations. Chapter 4 provides a mechanistic comparison between the Trk and MthK systems, focusing on their structural, functional and energetic similarities and differences, and ultimately highlighting the common energetic principles that govern the behavior of both regulatory modules and possibly that of all existing octameric RCK assemblies.

CHAPTER 2: DETECTING ANGSTRÖM-SCALE CONFORMATIONAL CHANGES IN THE TRK GATING RING BY ANALYZING FLUORESCENCE ANISOTROPY

Author Contributions

Structural analysis, experimental optimization and data collection were performed by Valentina Dimitrova. Valentina Dimitrova and John Lewis analyzed the single-particle data.

2.1 Introduction

2.1.1 Structure and function of Trk

Large intracellular accumulation of K^+ against an unfavorable electrochemical gradient is critical for cell survival. In bacteria, the endergonic process of K^+ influx is enabled by the nearly ubiquitous superfamily of K^+ transporters (SKT) (Corratge-Faillie et al., 2010). The SKT is comprised of secondary active transporters that harness the energy stored in established H^+ or Na^+ electrochemical gradients and use this energy to pump K^+ into the cell. The SKT includes the Trk family of H^+/K^+ symporters and the evolutionarily related Ktr family of Na^+/K^+ symporters.

The Trk transporter is a multicomponent complex expressed constitutively in a majority of bacterial species and fueled by the proton-motive force (Rhoads and Epstein, 1977; Rhoads and Epstein, 1978). Trk has a non-zero basal open probability that can be upregulated or downregulated in response to cytosolic ATP or ADP, respectively (Cao et al., 2013; Stewart et al., 1985). The Trk complex (Figure 2.1) is built from the transmembrane pore module TrkH, the cytosolic regulatory module TrkA and the auxiliary cytosolic component TrkE (Cao et al., 2011; Cao et al., 2013; Dosch et al., 1991; Epstein, 2003).

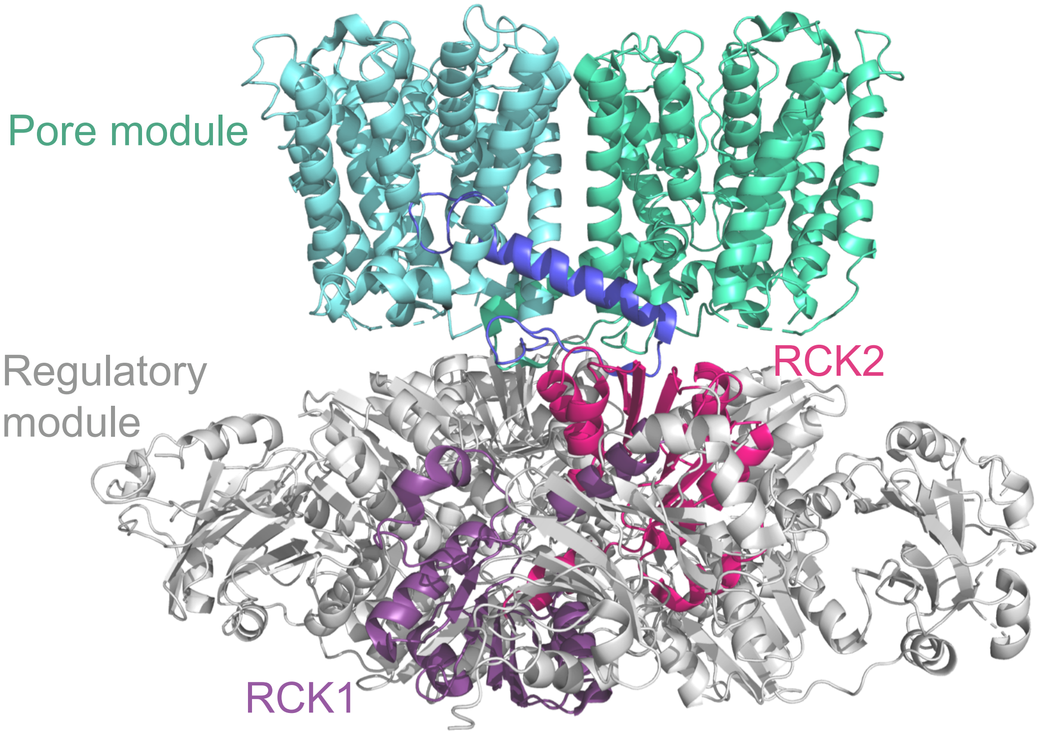

Figure 2. 1 – Crystal structure of the TrkAH channel complex

PDB code: 4J9U. The pore module (TrkH) is a homodimer of K^+-selective pore units (cyan and aquamarine). The cytosolic regulatory module (TrkA) is a homotetramer of RCK1-RCK2 sister pairs, one of which is highlighted here.

TrkH is a homodimer, where each monomer forms a K^+-selective pore with relatively high specificity and ~1 mM affinity for K^+. The TrkA and TrkE proteins are regulators of TrkH that bind cytosolic ATP and control pore opening (Harms et al., 2001; Nakamura et al., 1998). The exact regulatory role of TrkE is poorly understood, but ATP-dependent activity can be retained in its absence. Recent studies on the *V. parahaemolyticus* TrkAH complex, heterologously expressed in *E. coli*, demonstrate that the complex behaves like an ion channel facilitating passive K^+ diffusion and exhibiting open probability of 0.17 in absence of ligand. ATP increases the open probability of TrkH from 0.17 to 0.87, whereas ADP decreases the open probability to 0.015; this effect is mediated by TrkA and does not require ATP hydrolysis, suggesting that ATP acts as a ligand rather than an energy-supplying substrate for Trk.

The Trk regulatory module, TrkA, is built from four identical 50 kDa subunits, each containing a tandem pair of homologous RCK units (RCK1 and RCK2) that form the canonical RCK dimer, as described in Chapter 1 of this thesis (Cao et al., 2013; Figure 2.2A).

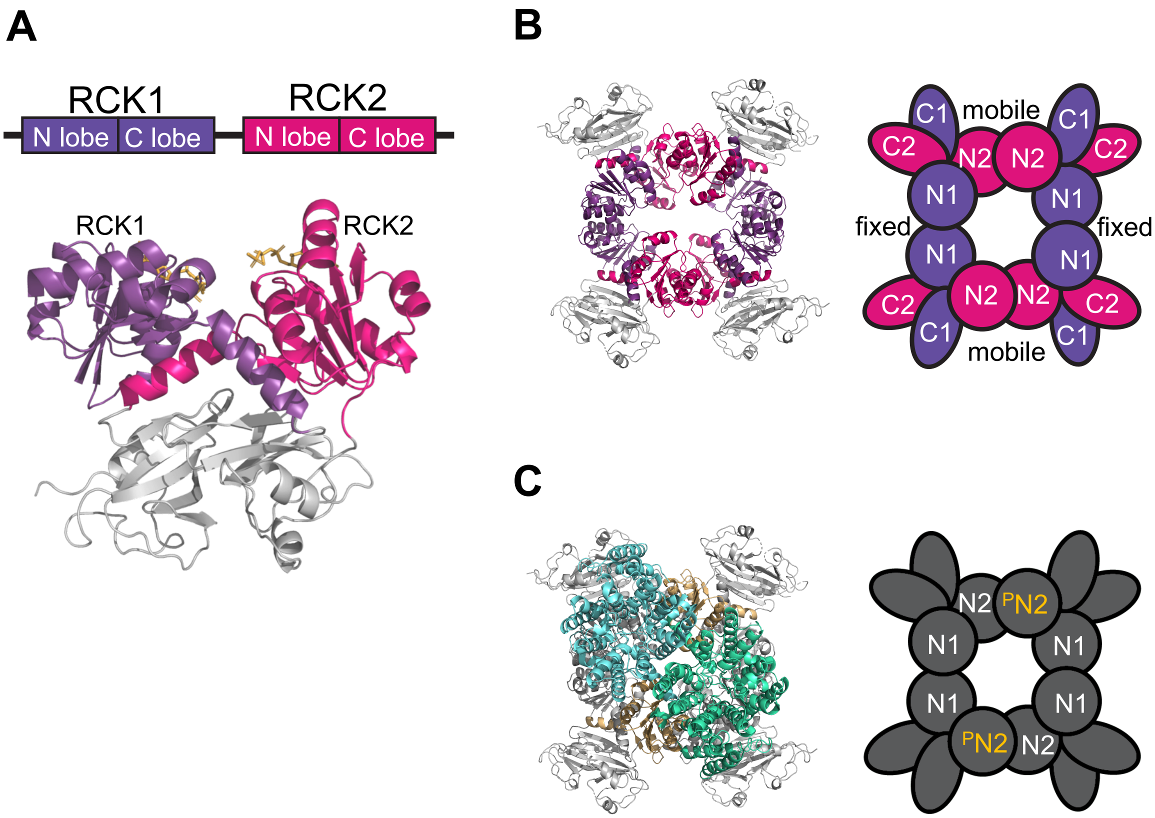

Figure 2. 2 – Assembly scheme of the TrkA gating ring

(A) Structure of the TrkA RCK dimer with one ATP-γS molecule bound to each RCK motif (PDB: 4J9V). **(B)** Top-down view of the TrkA gating ring (PDB: 4J9U) and a schematic representation of inter-dimer assembly interfaces in the isolated gating ring. **(C)** Top-down view of the TrkAH complex (PDB: 4J9U) and a schematic representation of inter-dimer assembly interfaces in the gating ring bound to the TrkH pore module.

The four RCK dimers build a two-fold symmetric ring, where RCK1-RCK1 neighbor interfaces alternate with RCK2-RCK2 neighbor interfaces around the ring perimeter (Figure 2.2B). At the time when the bulk of this thesis was prepared, the only whole-channel structure for TrkAH reflected that the pore module docks at two diametrically opposed RCK2 unit cores (^{P}N2) and that the remaining six RCK units do not interact with the pore directly (Figure 2.2C). However, a recently published structure of the ADP-bound TrkAH complex reflects that the pore module can simultaneously interact with all four RCKs from the top half of the gating ring (Zhang et al., 2020). Structural alignments predict that the RCK1-RCK1 interfaces are fixed, whereas the interfaces between RCK2 neighbors, as well as RCK1-RCK2 sisters, are mobile. Each RCK unit core hosts a ligand binding site that features the characteristic fingerprint region for nucleotide binding (see Section 1.3).

Crystallographic studies have captured two distinct conformations of TrkA, henceforth referred to as $\mathrm{TrkA_{flat}}$ and $\mathrm{TrkA_{twist}}$, resolved to 3.8 Å and 3.05 Å, respectively (Figure 2.3). The $\mathrm{TrkA_{flat}}$ structure was solved as part of the TrkAH complex and contains four NADH molecules, one in each RCK2 ligand binding site; NADH was used as additive to improve crystal quality and is likely irrelevant functionally. The $\mathrm{TrkA_{twist}}$ structure represents the gating ring in absence of pore module and contains eight ATP-γS molecules, one in each RCK binding pocket. Alignment of the two tetrameric structures predicts that the transition from $\mathrm{TrkA_{flat}}$ to $\mathrm{TrkA_{twist}}$ involves rigid-body rotation of the RCK2 core and peripheral subdomain from each RCK dimer around the αF1 hinge helix of the sister RCK1 unit; this global transition is accompanied with large rotational and translational motions at the RCK2-RCK2 interface, whereas the RCK1-RCK1 interface remains nearly static. Aligning an isolated RCK dimer from $\mathrm{TrkA_{flat}}$ against a dimer from

TrkA$_{\mathrm{twist}}$ reveals a notable intradimer cleft widening and a hinge angle reduction from 120° to 90°. Importantly, regardless of the extent of its positional change within the bounds of the gating ring, each individual RCK unit undergoes a conformational change; hence, TrkA$_{\mathrm{flat}}$ and TrkA$_{\mathrm{twist}}$ inform us of two distinct conformations for the RCK1 unit and two distinct conformations for the RCK2 unit.

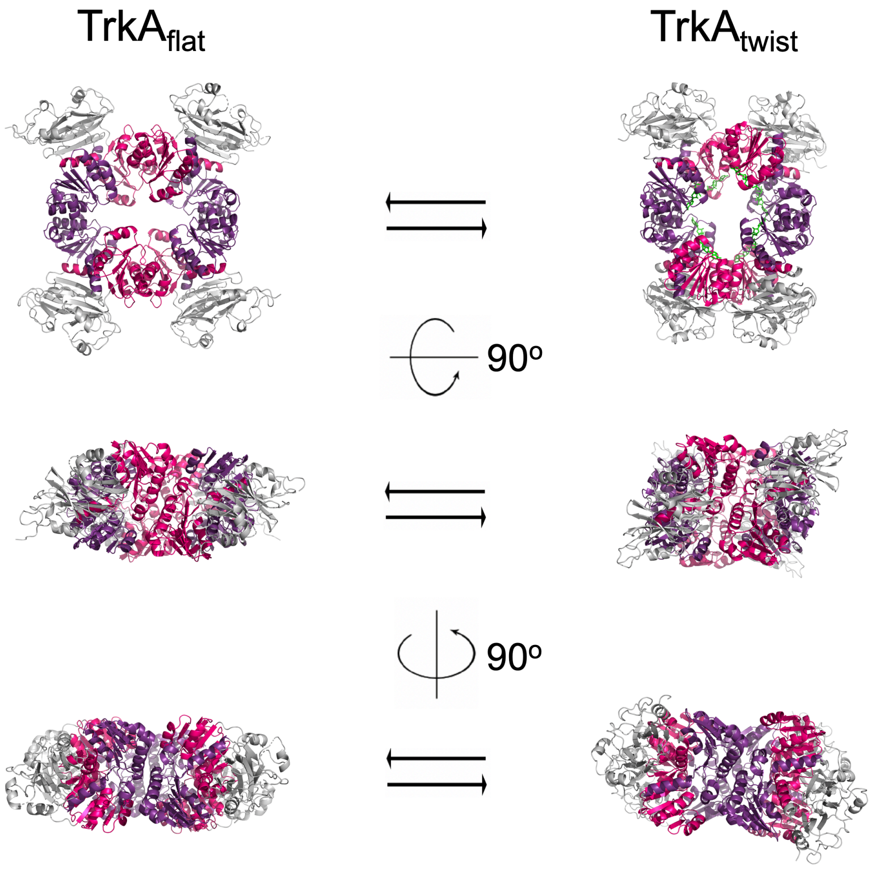

Figure 2. 3 – Two distinct conformations of the TrkA gating ring

Crystal structures of pore-bound TrkA$_{\mathrm{flat}}$ (PDB: 4J9U) and pore-free TrkA$_{\mathrm{twist}}$ (PDB: 4J9V) gating rings, reveal TrkA's impressive conformational flexibility and inform of two distinct conformations for the RCK1 and RCK2 motifs.

2.1.2 Using fluorescence anisotropy to detect single-molecule conformational changes

To study the mechanism through which TrkA regulates its associated pore module, we wished to track the conformational changes of an individual RCK unit within the gating ring in real time. This task necessitates resolving distances on the order of less than 10 Å on a millisecond timescale – a bold experimental undertaking that, until recently, was considered extremely technically challenging. A recent study, focusing on the structurally related MthK regulatory module, successfully resolved RCK unit states that differ by 3.4-8.1 Å on the linear scale, in real time (Lewis and Lu, 2019a). A key insight presented in this work is that conformational changes in most protein targets are accompanied by domain rotations, whereby secondary structure elements, such as α-helices, may adopt unique state-specific spatial orientations. The paradigm shift brought by this realization reframes the seemingly impossible quest of resolving angstrom-scale linear transitions in real time into the task of resolving small angular changes in the orientation of a properly chosen helix in the protein of interest. The latter can be achieved by attaching a fluorophore to the reporter helix and monitoring the fluorophore's orientation using a polarization microscope.

Several past investigations have utilized the fluorescence polarization method to study two-dimensional single-molecule motion (Adachi et al., 2000; Ha et al., 1998; Sase et al., 1997; Sosa et al., 2001; Warshaw et al., 1998). The extension of this method to the third dimension was practically achieved in a study tracking the three-dimensional motion of the myosin V lever arm domain, labeled with a bifunctional rhodamine probe (Forkey, 2003). The technique used in the myosin V studies has a ~25^{o} resolution and is well-suited for resolving the large angular changes (~80^{o}) involved in the swinging motion of the lever arm domain. However, a greater resolution of at least 10° is required in order to resolve the more subtle rotations of mobile helices in the RCK motifs of TrkA and MthK. A conceptually simple emission-based method to accomplish such resolution on a millisecond timescale was theorized at the beginning of this century (Fourkas, 2001), but was not practically feasible until a very recent technological development (Lewis and Lu, 2019a).

Effective resolution of 5° was successfully achieved in the single-molecule studies of RCK conformational changes in the MthK regulatory module. The experimental strategy involves the use of purified and fluorescently labeled MthK gating ring immobilized on a streptavidin-coated glass surface via four biotin-streptavidin anchors (Figure 2.4):

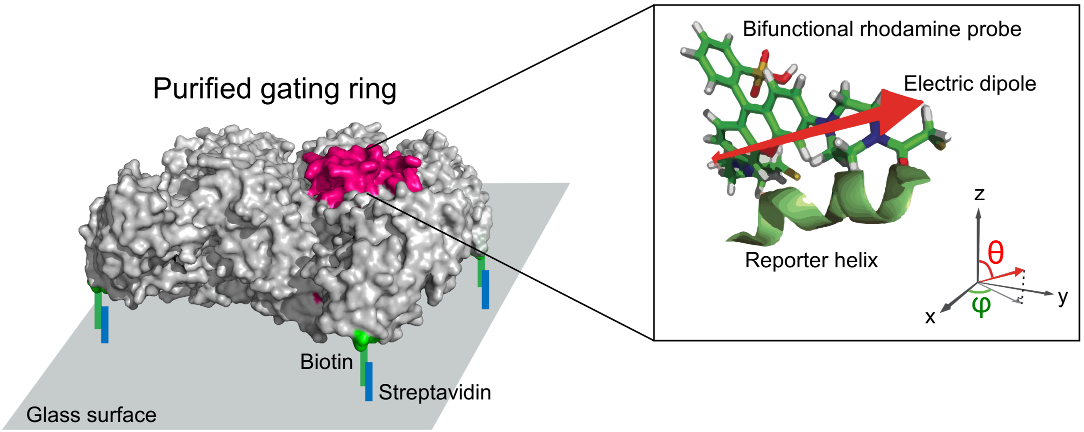

Figure 2. 4 – General experimental setup for single-molecule data collection

The attachment mode to the coverslip is such that the microscope's optical axis is aligned with the regulatory module's central axis. The αB helix in one of the eight RCK units per gating ring is labeled with a bifunctional rhodamine probe, cross-linked to two appropriately spaced cysteine residues engineered into the target helix. The two-point fluorophore attachment aligns the probe's emission dipole with the long axis of the helix, thus ensuring that the change in spatial orientation of αB is reliably reported by the polarization changes of the probe's emission signal. To ease the theoretical discussion of this technique, it is convenient to define a coordinate system whose z-axis aligns with the optical axis, and xy-plane coincides with the coverslip surface (Figure 2.4). Within this coordinate system the orientation of the emission dipole is defined by the inclination angle θ measured against the z-axis and rotation angle φ in the xy-plane measured against the x-axis. The next section outlines the strategy used to deduce the values of angles θ and φ from bifunctional rhodamine emission signal measurements.

2.1.3 Direct calculation of fluorophore orientation from polarized-emission intensities

In the method outlined above, the spatial orientation of a reporter helix serves as proxy for the protein's conformational state. If for each of the protein states the helix adopts a unique orientation, given by a three-dimensional vector $\mathbf{R} = R_x\hat{\imath} + R_y\hat{\jmath} + R_z\hat{k}$ (Figure 2.5A), then two states S_1 and S_2 can be resolved by resolving the two corresponding helix orientation vectors $\mathbf{R_1} = R_{x1}\hat{\imath} + R_{y1}\hat{\jmath} + R_{z1}\hat{k}$ and $\mathbf{R_2} = R_{x2}\hat{\imath} + R_{y2}\hat{\jmath} + R_{z2}\hat{k}$, equivalent to resolving vector positions separated by the linear distances $(R_{x2} - R_{x1})$, $(R_{y2} - R_{y1})$, and $(R_{z2} - R_{z1})$. Since the average radius of proteins is 20 Å (Brocchieri and Karlin, 2005; Erickson, 2009), one can expect that the notorious diffraction limit (Hecht, 2002) would make direct resolution of the position vectors in question untenable for any microscopy technique relying on visible light. Fortunately, the orientations of $\mathbf{R_1}$ and $\mathbf{R_2}$ can be completely divorced from the distance scale by thinking in terms of the vectors' spherical coordinates $(|\mathbf{R}|, \theta_1, \varphi_1)$ and $(|\mathbf{R}|, \theta_2, \varphi_2)$, respectively (Figure 2.5B). In a spherical coordinate system, $\mathbf{R}$'s orientation is fully defined by the polar angle θ and azimuthal angle φ, so resolving the two states S_1 and S_2 reduces to resolving angles, separated by the angular differences $\Delta\theta = (\theta_2 - \theta_1)$ and $\Delta\varphi = (\varphi_2 - \varphi_1)$.

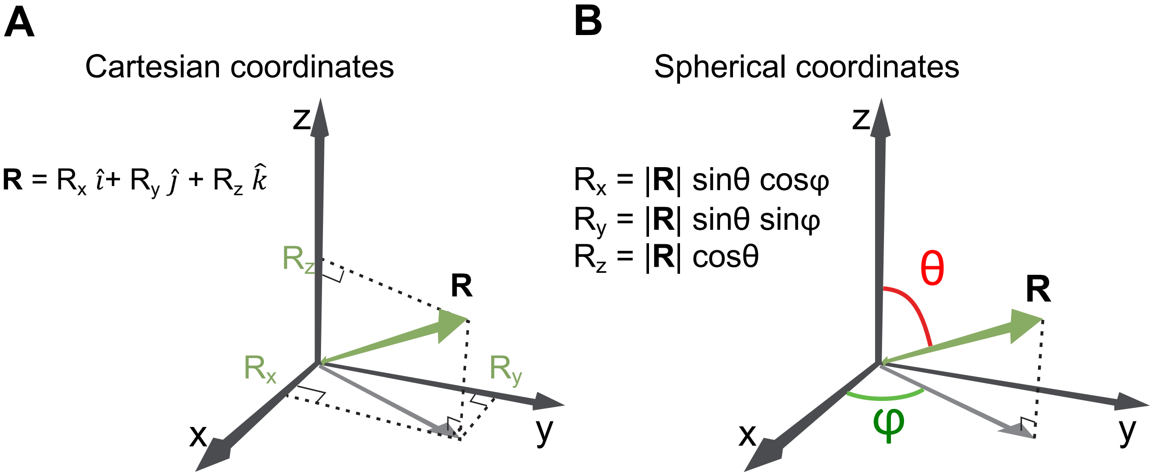

Figure 2. 5 – Three-dimensional description of an α-helix

Assuming that a bifunctional rhodamine probe has reacted with both appropriately spaced cysteine residues on the target helix, the fluorophore's emission dipole vector, **E** $= E_x\hat{\imath} + E_y\hat{\jmath} + E_z\hat{k}$, is parallel to **R**, such that the θ and φ coordinates of **E** reliably report on the protein conformational state. The Cartesian and spherical coordinates of **E** are related as follows:

$$E_x = |\boldsymbol{E}| sin\theta cos\varphi$$

$$E_y = |\boldsymbol{E}| sin\theta sin\varphi$$

$$E_z = |\boldsymbol{E}| cos\theta$$

2. 1 – Relationship between Cartesian and spherical coordinates of E vector

According to the fluorophore dipole model (Lakowicz, 2006), the dipole vector **E** represents the polarized portion, I_p, of the total emitted light, while a natural portion I_n also exists, such that:

$$I_p = I_n = |\boldsymbol{E}|^2$$

$$I_{tot} = I_p + I_n = 2|\boldsymbol{E}|^2$$

2. 2

where an additional proportionality constant is omitted but implied. The intensity components of I_p are given below:

$$I_x = E_x^2$$

$$I_y = E_y^2$$

$$I_z = E_z^2$$

$$I_p = I_x + I_y + I_z$$

2. 3

From Equations 2.1.1-3, it is clear that the values of θ and φ can be calculated from the intensities I_x, I_y and I_z.

As the microscope's objective collects the emission signal, the three vector components $\mathbf{E_x}$, $\mathbf{E_y}$, and $\mathbf{E_z}$ are mapped onto a two-dimensional space in a manner that preserves the information about the fluorophore's three-dimensional orientation (Figure 2.6). Since, the objective's surface is aligned with the xy-plane, passage through the objective preserves the polarization state of components $\mathbf{E_x}$ and $\mathbf{E_y}$. Conversely, $\mathbf{E_z}$, normal to the surface of the objective, becomes isotropic upon collimation (Figure 2.6B).

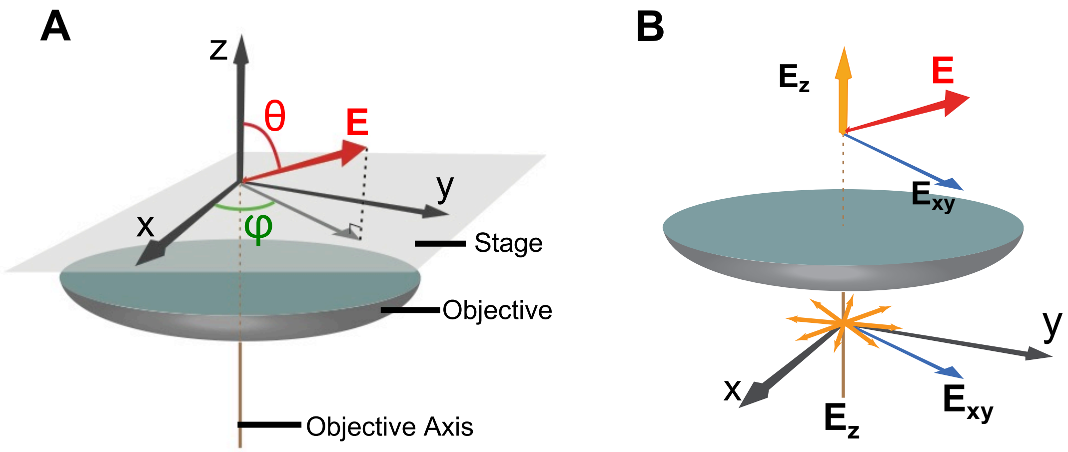

Figure 2. 6 – Polarization state of the collimated light signal

If a 0°-90° beam splitter were positioned downstream of the objective, the I_x signal component would be sorted entirely in the 0° channel and the I_y component entirely in the 90° channel; the isotropic I_z component and the I_{np} light portion would be evenly split between the two channels:

$$I_0 = I_x + \frac{1}{2}I_z + \frac{1}{2}I_{tot}$$

$$I_{90} = I_y + \frac{1}{2}I_z + \frac{1}{2}I_{tot}$$

2. 4

where I_0 and I_{90} are the intensities recorded from the 0° and 90° channels, respectively (Figure 2.7A). The two equations above have three unknowns and are thus insufficient for deducing the θ and φ values; more such linearly independent equations can be generated by splitting the emission signal into more than two channels. It can be shown that in general, the intensity collected by one of h number of channels with a polarization angle of ψ° relative to the x-axis is given by:

$$I_{\psi}(I_{tot},\theta,\varphi)=\frac{1}{h}I_{tot}\left[\frac{1}{2}sin^{2}\theta cos2(\varphi-\psi)+1\right]$$

2. 5 – Expression for one polarized intensity component as a function of θ, φ and I$_{tot}$

In theory, the I_{ψ} measurements from three channels would suffice to determine θ and φ (Fourkas, 2001), but practically, the beam can only be split into an even number of components (Figure 2.7B). Four-fold splitting of the emission signal can be achieved by first evenly dividing the beam with a non-polarizing beam splitter and then directing one half to a 0°-90° polarizing beam splitter, and the other half to a 45°-135° polarizing beam splitter. The resulting four polarized components I_0, I_{45}, I_{90}, and I_{135} are sufficient to calculate θ and φ as shown below:

$$\varphi=\frac{1}{2}tan^{-1}\frac{I_{45}-I_{135}}{I_0-I_{90}}$$

$$\theta=sin^{-1}\left(2\sqrt{\frac{\sqrt{(I_0-I_{90})^2+(I_{45}-I_{135})^2}}{(I_0+I_{45}+I_{90}+I_{135})}}\right)$$

$$I_{tot}=I_0+I_{45}+I_{90}+I_{135}$$

2. 6 – φ, θ and I$_{tot}$, expressed in terms of I$_0$, I$_{45}$, I$_{90}$ and I$_{135}$, without correction terms

Since in practice I_0, I_{45}, I_{90}, and I_{135} differ in terms of depolarization, including all four recorded values in the angle calculations improves the precision of θ and φ determination.

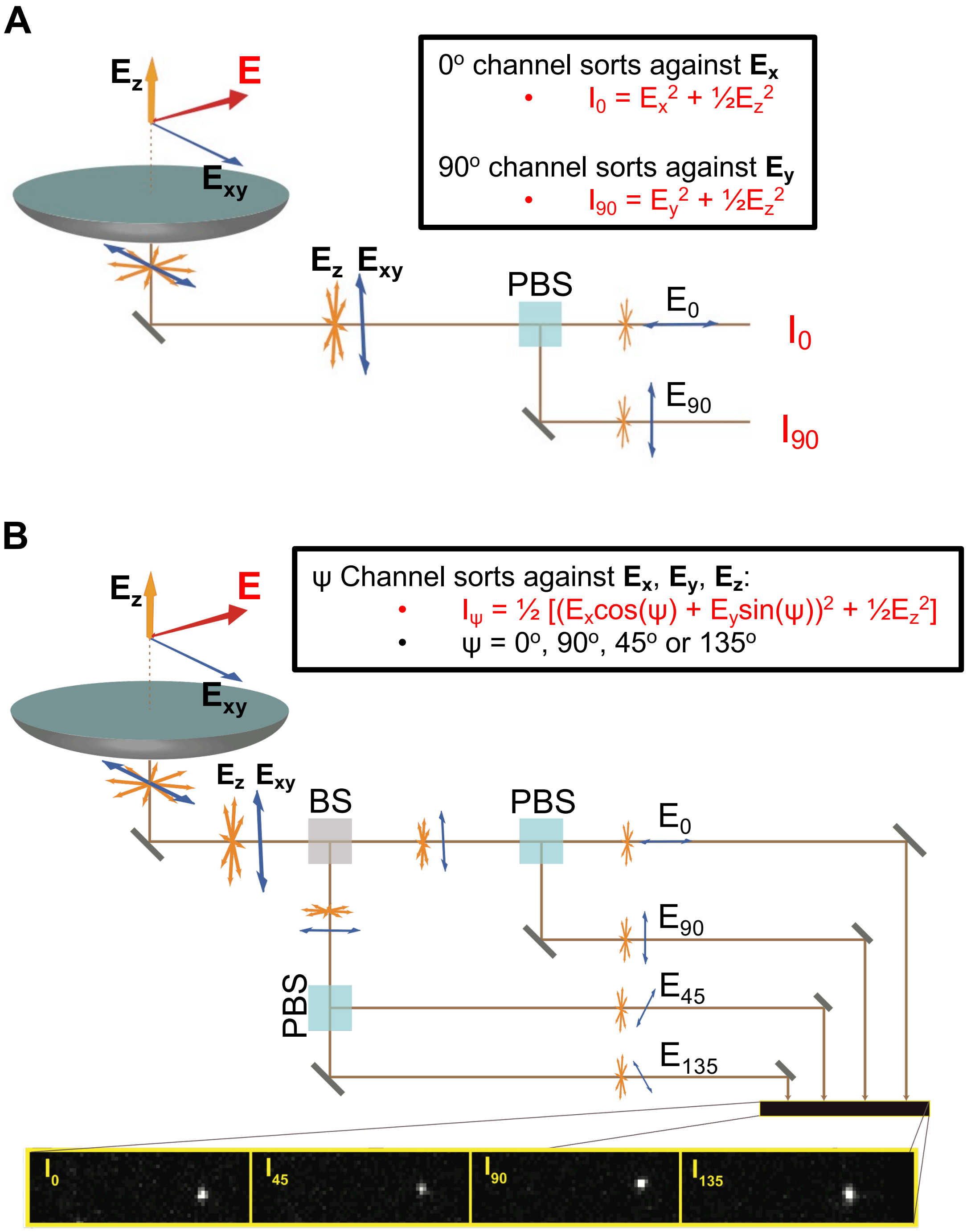

Figure 2. 7 – Sorting of the collimated emission signal

(A) Sorting into two polarized emission channels by passage through a polarizing beam splitter (PBS). **(B)** Sorting into four polarized emission channels. The beam is initially split evenly with a non-polarizing beam splitter, after which each beam half is sorted into two polarized components. The four signal components can be simultaneously recorded in real time with an EMCCD camera.

The precision of angle measurements can be further improved by implementing corrections that account for deviations from the idealized case discussed above. One set of corrections arises from the inability of the objective to collect all photons emitted by the probe (Axelrod, 1979). An objective collects light from a limited volume defined by a cone of half-angle $\alpha = \sin^{-1}(NA/n_g)$, where NA is the numerical aperture of the objective and n_g is the refractive index of the mineral oil. All photons are not collected unless $\alpha = 180^o$, but for real objectives $\alpha < 90^o$, an imperfection that can be accounted for by well-established corrections. Additional correction terms must be included to address any sources of meaningful emission signal depolarization throughout the data recording setup. Such depolarization can take place at the level of the probe itself as it experiences diffusive motion on timescales shorter than a single emission event. The light depolarization effects of this type of motion have been previously studied in the context of a tethered diffusion model (Forkey, 2000; Forkey, 2005), assuming a single attachment point between the probe and the protein, such that the fluorophore can span a cone with half-angle δ (dubbed the *wobble angle*). The value of the wobble angle for a particular probe, protein and attachment site can be determined experimentally (see Section 2.2.6.3) and used as a correction factor in the final calculations of θ and φ. Significant signal depolarization also occurs at the level of the polarizing beam splitters. This type of depolarization effect can be quantified by calculating the polarization ratio values, f_0, f_{45}, f_{90}, and f_{135}, reporting the amount of light that retains its original polarization in each of the four channels. Using a Wollaston beam splitter (Ohmachi et al., 2012) for the 0^o-90^o split yields $f_0 = 0.99$ and $f_{90} = 0.99$, indicating that this optical element barely changes the incident beam's polarization properties. The best practically achievable values for the other two polarization ratio vales are $f_{45} = 0.85$ and $f_{135} = 0.79$, using a wire-grid polarizer for the 45^o-135^o split (Lewis et al., 2019a; Lippert et al., 2017). Additionally, the actual polarization angle values ψ_0, ψ_{45}, ψ_{90} and ψ_{135} of the four polarized components may differ from the intended ones (0°, 45°, 90° and 135°), and light may not pass equally well through the four recording channels. The beam splitter imperfections listed above can be addressed by an appropriate set of correction terms, whose values can be deduced by following a calibration protocol (see Section 2.2.6.3).

Angle value calculations from continuous intensity recordings yield traces of θ and φ as functions of time that can be further analyzed, in order to identify states. State assignment is aided by tracking an additional angle value, Ω, which represents the overall rotation angle of the emission dipole between two states. Ω is related to the changes in θ and φ, and can be calculated from the dot product of the corresponding emission dipole vectors.

2.1.4 Prerequisites for successful single-molecule studies on the Trk regulatory module

The rest of this chapter details our efforts in adapting the technique discussed above to study ligand-induced conformational changes in the TrkA gating ring. Before single-molecule recordings can be performed on this protein, we must identify a viable reporter helix that not only adopts a unique spatial orientation in each of the known TrkA structures, but also undergoes large enough rotations to be detected by our method with resolution limit of 5°. We must then optimize the protein labeling protocol, involving a chemical reaction that covalently attaches a bifunctional rhodamine probe, containing two thiol-reactive iodoacetamide groups to two appropriately spaced cysteine residues engineered into the target helix. While determining the best labeling reaction conditions, we wish to maximize probe attachment to the intended site on the reporter helix and minimize off-target labeling. We must next demonstrate that the signal recorded from optimally labeled TrkA particles is of sufficient quality to enable detection of event transitions and subsequent state identification. Importantly, we must verify the method's viability for studying ligand-induced conformational changes in TrkA by demonstrating state probability dependence on ligand concentration.

2.2 Methods

2.2.1 TrkA structural analysis

The structure of ATP-γS-bound TrkA (TrkA$_{twist}$) was built from the half-ring atomic resolution model provided on RCSB Protein Data Bank (4J9V) by generating the appropriate symmetry-related object in the PyMOL molecular graphics system (referenced in Bibliography). A second and distinct structure for the isolated TrkA gating ring (TrkA$_{flat}$) was obtained by removing the pore module from the TrkAH complex model deposited online (4J9U). The two TrkA structures were aligned using PyMOL in combination with the molecular graphics application Coot (Emsley et al., 2010). Each structure was first moved to position its center of mass at the origin. Next, the TrkA$_{flat}$ structure was rotated relative to the xy-plane to make the z-axis perpendicular to the gating ring's transverse plane. Lastly, the TrkA$_{twist}$ structure was rotated relative to the TrkA$_{flat}$ structure until the 2-fold symmetry axes of the two molecules were closely aligned.

The aligned TrkA structures were then inspected to identify suitable reporter α-helices that rotate substantially between the two protein conformations, are long enough to accommodate the bifunctional rhodamine probe, are not essential for RCK octamer assembly or ligand binding, and have two properly spaced residues with solvent-exposed β-carbons. Such residue pairs would eventually be mutated to a cysteine pair that can react with the fluorescent probe.

Promising helices were studied further to predict the emission dipole orientation for a bifunctional rhodamine probe attached to a properly positioned cysteine pair. For each target helix a vector was assigned that connects the α-carbons of the two probe-reactive residues ($C_{\alpha 1}$ and $C_{\alpha 2}$):

$$\vec{A} = x_A\hat{\imath} + y_A\hat{\jmath} + z_A\hat{k}$$

2. 7

where the coordinates of $\vec{A}$ can be calculated from the PyMOL coordinates of $C_{\alpha 1}$ and $C_{\alpha 2}$ by simple vector algebra, as follows:

$$x_A = x_{C_{\alpha 2}} - x_{C_{\alpha 1}}$$

$$y_A = y_{C_{\alpha 2}} - y_{C_{\alpha 1}}$$

$$z_A = z_{C_{\alpha 2}} - z_{C_{\alpha 1}}$$

2. 8

The following trigonometric relationships were used to calculate the θ and φ coordinates for $\vec{A}$:

$$\theta = \cos^{-1}\frac{z_A}{\sqrt{x_A^2 + y_A^2 + z_A^2}}$$

2. 9 – Trigonometric relationship to calculate θ from known protein structure

$$\varphi = \cos^{-1}\frac{x_A}{\sqrt{x_A^2 + y_A^2}}$$

2. 10 – Trigonometric relationship to calculate φ from known protein structure

The overall rotation angle Ω between vector $\vec{A}$ and its corresponding vector $\vec{B}$ in the alternative protein conformation was calculated as follows:

$$\Omega = \cos^{-1}\frac{x_A x_B + y_A y_B + z_A z_B}{\sqrt{(x_A^2 + y_A^2 + z_A^2)\,(x_B^2 + y_B^2 + z_B^2)}}$$

2. 11 – Trigonometric relationship to calculate helix rotation angle between two structures

2.2.2 Cloning and purification of TrkA

A gene encoding the *Vibrio parahaemolyticus* TrkA protein was cloned into a modified pET31b expression vector (Novagen) in frame with a C-terminal recognition sequence for Tobacco Etch Virus (TEV) protease. A sequence encoding a double strep-tag with high intrinsic affinity toward streptavidin (Schmidt and Skerra, 2007) was fused downstream of the TEV site via the Seamless Ligation Cloning Extract (SLiCE) method (Zhang et al., 2012). The resulting recombinant DNA sequence encoded full-length TrkA with a C-terminal twin-strep-tag (SA<u>WSHPQFEK</u>GGGSGGGSGGSA<u>WSHPQFEK</u>), cleavable by TEV. Desired mutations in the TrkA sequence were introduced via site-directed mutagenesis.

BL21(DE3) bacterial cells were transformed with the pET31b plasmid carrying desired TrkA sequences; successful transformation and plasmid retention was ensured via kanamycin antibiotic selection. Large suspension cultures were grown in Luria broth supplemented with 25 mg/L kanamycin at 37 °C and induced at $OD_{600nm} = 0.8$ with 0.2 mM isopropyl β-D-1-thiogalactopyranoside (IPTG, Sigma) for 16-18 h at 20 °C. Following induction, cells were harvested via centrifugation and cell pellets were snap-frozen in liquid N_2 and stored at -80 °C for up to 1 year.

For TrkA protein purification, cell pellets were thawed and resuspended in ice-cold base buffer (50 mM Tris-HCl, pH 8.0, 150 mM KCl, 5 mM 2-mercaptoethanol), containing 1 mM phenylmethanesulfonyl fluoride (PMSF, Sigma). Cell suspension was sonicated with Branson 450 Sonifier (VWR Scientific) at 60% duty cycle, output control setting #9 for 3 rounds of 45 pulses each and 5-min breaks on ice between sonication rounds. Further cell lysis was carried by 20-min room-temperature rocking incubation in the presence of 0.2% Triton X-100 detergent. Cell lysate was cleared via high-speed centrifugation and poured over a column packed with Strep-Tactin® Superflow affinity resin (IBA Life Sciences) equilibrated with base buffer. Following a column wash with 10 column volumes (CV) of base buffer, TrkA was eluted with ~5 CV of 10 mM d-Desthiobiotin (Sigma) in base buffer and concentrated to 180-300 μM using Amicon® Ultra centrifugal filter units with 10-50 kDa molecular weight cutoff range (Millipore Sigma). Concentrated affinity-purified TrkA was aliquoted, and either used immediately or snap-frozen in liquid N_2 and stored at -80 °C for up to 1 year.

The oligomeric state and solubility of purified wild-type or mutant TrkA proteins were assessed by size exclusion chromatography using a Superdex 200 10/300 GL column (GE Healthcare), pre-equilibrated in gel filtration buffer (20 mM Tris-HCl, pH 8.0, 100 mM KCl). The oligomeric state of wild-type TrkA was determined via a quantitative approach, whereby a commercial mixture of proteins with known molecular weights (Bio-Rad) is first run through the gel filtration column. The common logarithm of each standard protein's molecular weight is then plotted against its experimentally observed elution volume, and a line equation is generated that allows the direct calculation of TrkA's molecular weight from its own elution volume. The oligomeric states of all mutant TrkA proteins were deduced by comparison to the elution profile of wild-type TrkA.

2.2.3 Preparation and quantitative assessment of fluorescently labeled TrkA samples

Aliquots of affinity-purified TrkA were subjected to size exclusion chromatography using either a Superdex 200 or a Superose 6 10/300 GL column in gel filtration buffer. Peak fractions were pooled and concentrated to 100-200 μM. Next, the concentrated protein was reduced for 1 h at room temperature with tris(2-carboxyethyl)phosphine (TCEP, Hampton Research) at a concentration ensuring 1 TCEP molecule was present for every Trk regulatory module. Reduced TrkA regulatory modules were then mixed with a cysteine-reactive fluorescent probe at room temperature. For labeling efficiency experiments, the dye used was tetramethylrhodamine-5-iodoacetamide (5-TMRIA, Invitrogen) at a ratio dye:subunit = 1.8:1 and the incubation time was 90 min. For single-molecule data collection, TrkA was instead labeled with the dye bis-((N-iodoacetyl)piperazinyl)-sulfonerhodamine (BRI_2, Invitrogen), providing one dye molecule per gating ring and incubating for 12-16 h. Upon reaction completion, free dye was removed by applying the sample to a Zeba™ spin desalting column (Thermo Fisher). Cleared labeled sample was subjected to size exclusion chromatography; absorbance at 280 nm and 550 nm was simultaneously monitored during gel filtration runs of labeled protein samples. The A_{280nm} and A_{550nm} values were used to calculate the concentration of protein and dye, respectively, using the Beer-Lambert law:

$$A = \varepsilon l c$$

2. 12 – Beer-Lambert law

where the protein or dye concentration c can be calculated from the measured sample absorbance A, the molar extinction coefficient ε (ε_{TrkA} = 29,000 $M^{-1}cm^{-1}$, $\varepsilon_{rhodamine}$ = 87,000 $M^{-1}cm^{-1}$), and the optical path length l (l = 1 cm for the quartz cuvette used in the described experiments). Labeling efficiency was calculated as the ratio of the concentration of dye to the concentration of TrkA subunits in each labeled sample.

2.2.4 Assembly of data collection chamber

Prior to chamber assembly, all glass components were thoroughly cleaned. Glass coverslips (24x30-1.5, Fisher) and glass micro slides (25x75x1 mm, VWR) were arranged vertically in a Coplin jar, filled with 30% 7X® cleaning solution (MP). The jar was placed in a Branson 3510 ultrasonic cleaner apparatus and a 20 min sonication round was performed at 32 °C. Next, the cleaning solution was gently decanted and the open Coplin jar with its contents still inside was placed under running tap water for 10 min, then under running deionized water for 3 min. The water-filled Coplin jar was returned to the bath sonicator for another 20 min cleaning round at 32 °C. The water in the Coplin jar was then carefully removed and replaced with 200 proof ethanol, after which a final 20 min sonication round was performed. Lastly, the ethanol was gently poured out and the partially open jar was left in a clean room to air-dry the contents overnight.

Clean glass coverslips were coated with 0.01% poly-L-lysine hydrobromide (Sigma), as follows: 85 μl drops of the coating solution were deposited onto a clean glass surface and coverslips were placed gently face-down onto the drops, one coverslip per drop. After 1 h incubation at room temperature, the coverslips were rinsed three times with 3.5 mL filtered deionized water and left to air-dry overnight.

Each sample chamber was built by attaching the lysine-coated surface of a coverslip onto the face of a glass micro slide via double-sided adhesive tape. Leaving two opposite edges of the coverslip untaped resulted in a basic perfusion chamber with a volume of ~15 μl. Perfusions were performed manually by pipetting a desired solution at one end of the chamber, while holding a piece of absorbent paper at the other end. After mounting a slide onto the microscope objective using Type B Cargille immersion oil, each chamber was washed with 20 volumes of deionized water, then 20 volumes of wash buffer (10 mM HEPES, pH 7.5, 200 mM KCl). Streptavidin (Promega) at 5 mg/mL in wash buffer was then introduced and allowed to attach to the lysine-coated surface for 15 min. Unbound streptavidin was washed away with 20 chamber volumes of wash buffer. Next, 3 chamber volumes of 0.5 nM fluorescently labeled TrkA were flowed in and protein immobilization was allowed to occur for 5 min. Lastly, the chamber was perfused with 4 volumes of activation buffer (20 mM Tris-HCl, pH 7.0, 233 mM K^+, 50 mM $MgCl_2$, 100 mM DTT, 0-50 mM ligand). The ligands used were Adenosine 5'-(β,γ-imido)triphosphate lithium salt hydrate (AMP-PNP, Sigma), Adenosine 5'-diphosphate potassium salt (ADP, Sigma), or Adenosine 5'-monophosphate disodium salt (AMP, Sigma). In experiments with inorganic phosphate (PO_4^{3-}), $MgCl_2$ was excluded from the activation buffer recipe to avoid phosphate precipitation.

2.2.5 Single-molecule measurements

Data collection followed a modified version of a recently described protocol (Lewis and Lu, 2019a). Single-molecule measurements were performed on a fluorescence polarized microscope built from a Nikon microscope (model Ti-E). To generate the excitation signal, a linearly polarized laser beam (532 nm) from a 100 mW laser (Crystalaser CL532-100-S) was attenuated through a continuous neutral density filter and then transformed into a circularly polarized beam by passing through a ¼ λ-plate, positioned at 45° relative to the polarization of the incident light. The beam was then passed through a 100X objective (Nikon Achromatic, NA = 1.49), and directed at a 76° angle incident to the coverslip, to meet the condition for total internal reflection (Axelrod et al., 1984) and give rise to an evanescent field that excites the fluorophores on the coverslip surface. The polarized emission signal from individual fluorophores was collected by the objective and subsequently passed through a 540/593 nm bandpass filter (Semrock FF01-593/40-25) to prevent excitation light propagation. Next, the emission signal was split in two identical beams by a 50:50 non-polarizing beam splitter (Thorlabs CM1-BS013). One resulting beam was further split along 0° and 90° by a Wollaston polarizing beam splitter (Edmund Optics 68820), and the other beam was split along 45° and 135° by a wire-grid polarizing beam splitter (Thorlabs WP25M-Vis). Each of the four resulting beams, I_0, I_{45}, I_{90} and I_{135}, was directed onto a designated sector in the CCD grid of an EMCCD camera (Andor iXon Ultra 897), allowing the four polarized components for each fluorophore to be recorded simultaneously and in real time.

To minimize signal interference between neighboring emitting particles, data were collected from coverslips containing a well-spaced, sparse population of 15-30 fluorescently labeled TrkA molecules per field. For each tested ligand concentration, multiple 15-second movies were recorded, each from a different field on the coverslip, at 33 frames per second, at room temperature. To ensure that the protein, fluorophore and buffer qualities remain optimal throughout the entire span of data collection, all labeled protein samples and buffers were kept on ice until needed and only small aliquots were taken out and warmed up to room temperature 10 min prior to chamber preparation; a new chamber was prepared and used every 1.5 h.

2.2.6 Data analysis

2.2.6.1 Detection and integration of intensities

Upon exiting the beam splitters, the four polarized emission component beams are not perfectly parallel, causing translational and rotational offsets between the images captured in the four designated EMCCD camera sectors. To extract intensity traces from the recorded movies, an automated program was used that first finds the particles, then relates the particles from the reference 0° channel to those from the remaining three channels and lastly integrates the four intensities for each identified particle (Lewis and Lu, 2019a).

For each recorded movie, the first 75 movie frames were averaged to obtain clear particle images. The entire image-capturing field was then explored to select pixels whose intensities were greater than an empirically determined threshold value. Each isolated cluster of selected pixels represented a particle defined by a matrix with information on the particle’s position and boundaries. The center of each examined particle was defined as the intersection between the row and column with highest intensity.

Signals captured in the reference channel were next related to those in the remaining three channels by accounting for the rotational and translational offsets between the channels. Briefly, in a preliminary calibration step, three particles were chosen manually in the reference channel to define a plane with maximal area, corresponding to this channel’s xy-plane. The same particle triplets were chosen in the rest of the imaging channels defining their own xy-planes. The reference channel's xy-plane was then translated and rotated to match the xy-planes in the other three channels. The latter operation provided the translational offset values Δx_n and Δy_n relating the reference and the nth channel, as well as the corresponding rotational offset angles γ_n and α_n around the reference channel's x- and z-axis, respectively.

Particle signal intensities were computed by applying a 'zoning' approach commonly used to integrate intensities in crystallography. Briefly, for each particle, a data-capturing zone was defined that contains 90% of the total intensity. From the particle's center a circle was drawn with radius twice as large as that of the data capturing zone. Within such a circle, two additional zones were defined: the buffer zone, containing the remaining 10% of the particle intensity and a background zone composed entirely of dark pixels. For each particle, the mean pixel intensity was computed in the data-capturing zone and the corresponding background value was subtracted. Performing this operation for all movie frames in all four channels generated four polarized emission intensity traces that were subsequently used in angle calculations.

2.2.6.2 Detection of event transitions

Event transitions in the four measured polarized intensities were detected by the change point algorithm, which has been previously applied to analyzing photon arrival time in multichannel recordings and was recently adapted for analyzing intensity data collected over a fixed time interval (Beausang et al., 2011; Chen and Gupta, 2001; Lewis and Lu, 2019a). The analytical method we used detects concurrent changes in photon emission rate in all four polarized intensity traces by finding values for τ that maximize the cumulative log-likelihood-ratio function below:

$$LL_R = \sum_{r=1}^{h} m_r \ln\left(\frac{m_r}{\tau}\right) + (N_r - m_r)\ln\left(\frac{N_r - m_r}{T - \tau}\right) - N_r \ln\left(\frac{N_r}{T}\right)$$

2. 13 – Log-likelihood-ratio function for event transition detection

where $h = 4$ is the number of intensity traces included in the function, m_r is the number of photons collected in the rth channel by arrival time τ, N_r is the total number of photons collected in the rth channel for the duration T of the time interval observed. A detailed derivation of Equation 2.13 has been recently provided elsewhere (Lewis and Lu, 2019a). Briefly, for each of the four intensity traces, a log-likelihood function LL_0 is derived that reflects the probability that the fluorophore emits photons at a constant rate during a time interval T. A second log-likelihood function LL_1 is also produced for the alternative scenario that the rate of photon emission changes at time point τ within the time interval T. The ratio of the two log-likelihood functions LL_1 and LL_0 tests the two hypotheses that within the time interval T an intensity change does or does not occur. LL_1/LL_0 ratio functions from all four channels are then combined to produce the LL_R function above.

By utilizing the log-likelihood-ratio method we performed an automated search of event transitions as follows: the program first searched for a single transition over the entire trace. If a change point X was discovered, the program sought additional transitions between the start of the trace and X, and between X and the end of the trace. This process was iterated for progressively shorter time intervals until the LL_R value fell below a significance threshold that limits the false positive events to 5%, resulting in 1% false negative events.

2.2.6.3 Angle calculations from single-molecule recordings

The values of φ and θ were calculated from Equations 2.14-16 below:

$$\varphi = \frac{1}{2} tan^{-1}(\frac{(I_{45} - I_{135})(f_0 cos2\psi_0 - f_{90} cos2\psi_{90}) - (I_0 - I_{90})(f_{45} cos2\psi_{45} - f_{135} cos2\psi_{135})}{(I_0 - I_{90})(f_{45} sin2\psi_{45} - f_{135} sin2\psi_{135}) - (I_{45} - I_{135})(f_0 sin2\psi_0 - f_{90} sin2\psi_{90})})$$

2. 14 – φ, expressed as a function of I_0, I_{45}, I_{90}, I_{135} and correction terms

$$I_{tot} = \frac{1}{2}(\frac{[X_2 + X_1 f_0 cos2(\varphi - \psi_0)]I_{90} - [X_2 + X_1 f_{90} cos2(\varphi - \psi_{90})]I_0}{X_1(X_3 - \frac{2}{3}X_2X_4)(f_0 cos2(\varphi - \psi_0) - f_{90} cos2(\varphi - \psi_{90}))} + \frac{[X_2 + X_1 f_{45} cos2(\varphi - \psi_{45})]I_{135} - [X_2 + X_1 f_{135} cos2(\varphi - \psi_{135})]I_{45}}{X_1(X_3 - \frac{2}{3}X_2X_4)(f_{45} cos2(\varphi - \psi_{45}) - f_{135} cos2(\varphi - \psi_{135}))})$$

2. 15 – I_{tot}, expressed as a function of I_0, I_{45}, I_{90}, I_{135}, φ and correction terms

$$\theta = sin^{-1}(\sqrt{\frac{1}{2X_1X_4I_{tot}}\left(\frac{I_0 - I_{90}}{f_0 cos2(\varphi - \psi_0) - f_{90} cos2(\varphi - \psi_{90})} + \frac{I_{45} - I_{135}}{f_{45} cos2(\varphi - \psi_{45}) - f_{135} cos2(\varphi - \psi_{135})}\right)})$$

2. 16 – θ, expressed as a function of I_0, I_{45}, I_{90}, I_{135}, I_{tot}, φ and correction terms

where X_1, X_2 and X_3 are constants describing the collection of light through the objective, X_4 is a correction factor for the diffusive motion of the probe, ψ_0, ψ_{45}, ψ_{90} and ψ_{135} are the calibrated polarization angle values of the polarized-beam splitters, and f_0, f_{45}, f_{90} and f_{135} are correction terms accounting for the effect of the splitters on the effective ψ and on light polarization. A theoretical discussion of the three equations above is provided in Section 2.1.3 of this thesis and a detailed derivation can be found in the Supplementary section of Lewis and Lu, 2019a.

To account for the incomplete collection of photons by the objective with collection cone half-angle α = 78.5°, we used the correction factors X_1, X_2 and X_3, all of which can be calculated from the value of α (Axelrod, 1979; Fourkas, 2001) as follows:

$$X_1(\alpha) = \frac{\pi}{12}(7 - 3cos\alpha - 3cos^2\alpha - cos^3\alpha)$$

$$X_2(\alpha) = \frac{\pi}{2}(cos\alpha - cos^3\alpha)$$

$$X_3(\alpha) = \frac{2\pi}{3}(1 - cos\alpha)$$

2. 17

The value of correction factor X_4 was determined from the equation below:

$$X_4(\delta) = \frac{r_{app}}{r_0}$$

2. 18

where the apparent anisotropy of r_{app} of the fluorophore experiencing some diffusive motion and the intrinsic anisotropy of the rhodamine probe r_0 = 0.395 (Corrie et al., 1998), are related through the so-called wobble angle δ as follows:

$$\langle r_{app} \rangle = r_0 \frac{1}{2} cos\delta(1 + cos\delta)$$

2. 19 – Relationship between anisotropy and wobble angle

The r_{app} value can be determined experimentally by measuring the anisotropy of labeled TrkA in solution with the caveat that all measured values r would be underestimates of the true r_{app} value due to protein tumbling; yet, r and r_{app} are still related:

$$\frac{1}{r} = \frac{1}{r_{app}}(1 + \frac{RT}{\eta V})$$

2. 20 – Relationship between anisotropy, measured in solution, and apparent anisotropy

where R, T, η and V are the gas constant, temperature, viscosity and protein volume, respectively. From the equation above it is apparent that $r \rightarrow r_{app}$ as $\eta \rightarrow \infty$. To determine r_{app} for the BRI$_2$ probe attached to TrkA's αB2 helix we measured the anisotropy of solutions containing 120nM labeled protein in AniTest buffer (20 mM Tris-HCl, pH 8.0, 100 mM KCl, 0-50% glycerol), using a polarization fluorometer (Photon Technology International (PTI) QuantaMaster fluorometer). Samples were excited with vertically or horizontally polarized light at λ_{ex} = 545 nm and emission was detected at λ_{em} = 575 nm and separated into vertical and horizontal components from which anisotropy was calculated.

In Equations 2.14-16 above, the ψ and f_ψ values account for beam splitter imperfections that affect the polarization of the emission signal's four components. An additional correction factor, $g_\psi = \frac{I_{tot,90}}{I_{tot,\psi}}$, is implicitly included in the above equations to account for differences in the amount of light passing through each of the four recording channels. The numerical values of g_ψ, ψ and f_ψ were determined by measuring the four channel intensities when the collected signal's φ component was pre-set and known. Briefly, a bright-field light beam was passed through a polarizer that allows incremental adjustment of the emerging beam's φ value prior to being collected with the microscope objective. By varying φ in 5° increments in the 0° to 180° range we generated a plot for each of the four measured intensities as a function of φ and globally fitted the four plots to the equation below:

$$I_\psi = \frac{1}{4} g_\psi I_{tot} [f_\psi sin^2\theta cos2(\varphi - \psi) + 1]$$

2. 21

where θ was set to 90°. The fitted values of g_ψ, ψ and f_ψ were then used as intended to calculate θ, φ and I_{tot} with Equations 2.14-16.

The Ω values were calculated according to the dot-product-based equation below:

$$\Omega_{i,j} = cos^{-1}(\frac{\boldsymbol{E}_i.\boldsymbol{E}_j}{|\boldsymbol{E}_i|.|\boldsymbol{E}_j|})$$

2. 22 – Expression for the overall rotation angle Ω between two states

where $\Omega_{I,j}$ is the overall probe rotation angle between states i and j, and ***E*** is defined by θ and φ as discussed in Section 2.1.3 above.

2.2.6.4 State identification

Angle calculations from the four polarized emission signals yielded traces for θ, φ and Ω as functions of time, and transition point analysis defined individual events within these traces. For each such event in the θ, φ or Ω traces, individual data points were averaged over the event lifetime, so that each event i had an associated set of three mean angle values (${}_\theta x_i$, ${}_\varphi x_i$, ${}_\Omega x_i$). Note that the ${}_\Omega x_i$ for a state S_i is calculated in reference to another identified state. Each event was then sorted into one of k states based on the event-specific (${}_\theta x_i$, ${}_\varphi x_i$) angle pairs, assuming that each state follows a Gaussian distribution. Sorting was achieved by a k-means clustering algorithm (Press, 2007), which operates on a 'nearest neighbor' principle, comparing each ($_\theta x_i$, $_\varphi x_i$) pair to each of the k state means ($_\theta\mu_k$, $_\varphi\mu_k$) and assigning the interrogated event to the state with the closest mean, equivalent to minimizing the distance, given by the equation below:

$$d_{i,k} = \sqrt{({}_{\theta}\mu_k - {}_{\theta}x_i)^2 + ({}_{\varphi}\mu_k - {}_{\varphi}x_i)^2}$$

2. 23 – K-means clustering distance equation

Events are first sorted against states with randomly chosen means to provide the initial $d_{i,k}$ values; subsequently, events are reassigned and $d_{i,k}$ distances are recalculated, following an iterative process that ends when no further reassignment takes place. K-means clustering alone can adequately sort the data against two states, but the algorithm's performance deteriorates for $k \geq 3$, as it becomes highly sensitive to initial guess values for the state parameters. To boost the performance of our core state identification algorithm, we paired it with two optimization routines: Nelder-Mead downhill simplex and simulated annealing (Press, 2007). The resulting state identification program iteratively reassigns events and seeks state parameter values, aiming to minimize the log likelihood ratio function below:

$$LL_R = \frac{LL_k}{LL_1} = \frac{\sum_k \sum_i [\,({}_{\theta}\mu_k - {}_{\theta}x_i)^2 + \left({}_{\varphi}\mu_k - {}_{\varphi}x_i\right)^2]}{\sum_i [\left({}_{\theta}\mu_1 - {}_{\theta}x_i\right)^2 + \left({}_{\varphi}\mu_1 - {}_{\varphi}x_i\right)^2]}$$

2. 24 – Log-likelihood-ratio for state identification

where LL_k and LL_1 correspond to the cases of k states and one state, respectively.

The most probable number of states was determined for each analyzed particle by performing the above algorithm at various k = 1, 2, …, n until a k value is reached for which adding one more state (k+1) would be no longer statistically justified based on an *F* test evaluating the statistical difference between Chi-squared values χ_k^2 and χ_{k+1}^2 (Horn, 1987; Lewis and Lu, 2019a).

The data analysis discussed above yielded a summary for each individual TrkA particle that includes the I_{tot}, I_0, I_{45}, I_{90} and I_{135} intensity traces with identified transitions, the three angle traces, the number of identified states, the means (${}_{\theta}\mu_k$, ${}_{\varphi}\mu_k$) and standard deviations (${}_{\theta}\sigma_k$, ${}_{\varphi}\sigma_k$) for each respective state, and the assignment of each event to its most probable state distribution. State distributions were then sorted in order of increasing ${}_{\theta}\mu_k$ to generate state identities S_1, S_2, …, S_k, with θ means related by: $\theta_1 \leq \theta_2 \leq \ldots \leq \theta_k$. State identification ambiguities, arising from unresolved θ distributions, were addressed by choosing state identities such that $\Omega_{12} \leq \Omega_{23} \leq \ldots \leq \Omega_{(k-1)k}$. Individual TrkA particles were manually selected or rejected based on a thorough inspection of their respective data analysis summaries. All selected particles had low-noise intensity traces, showing clear signs of adequate signal polarization and a single photobleaching event at the end of the I_{tot} trace. To improve the resolution, we extended our list of selection criteria to only include particles with 5 or more events per trace and effective σ values $\leq 7^{o}$. Lastly, ensemble analysis was performed on a large number of selected TrkA particles, reporting the ensemble means for θ and Ω.

2.3 Results

2.3.1 Structure-guided search for suitable reporter helices in the RCK motifs of TrkA

The two aligned TrkA structures, $\text{TrkA}_{\text{flat}}$ and $\text{TrkA}_{\text{twist}}$ were first qualitatively inspected to identify mobile α-helices within the RCK1 and RCK2 motifs (Table 2.1). With the exception of helix αF1, all RCK1 helices are relatively immobile, consistent with the previously reported involvement of this motif's core region in the assembly of fixed neighbor interfaces in TrkA (Cao et al., 2013; Figure 2.2). Conversely, all of the helices in the RCK2 motif undergo substantial rigid body rotation between the two protein conformations, as would be expected from the role of RCK2 in building TrkA's mobile neighbor interfaces. Among the mobile helices in RCK2, three were deemed inadequate for probe attachment: the αC2 helix is too short to accommodate the bifunctional rhodamine probe, whereas the αD2 and αE2 helices are important for the overall structural integrity of the TrkA gating ring, as they participate in important inter-subunit contacts between neighboring RCK2 core regions. The N-terminus of αA2 both lines the RCK2 ligand binding pocket and critically contacts the sister αF1; nevertheless, the αA2 helix was still considered promising since its length enables us to attach a probe far away from its N-terminus. The initial qualitative inspection of the two TrkA structures thus revealed four promising α-helices: αF1, αA2, αB2 and αF2, each of which contained at least one solvent-exposed residue pair with proper spatial orientation for probe attachment chemistry.

Table 2. 1 – Summary of findings from qualitative inspection of TrkA α-helices

Helix ID		Visual assessment outcome				
Location within TrkA's amino acid sequence	RCK nomenclature	Detectable rotation? (Y/N)	# helical turns	Important interface proximity? (Y/N)	Binding pocket proximity? (Y/N)	Probe-receptive residue pair? (Y/N)[e]
Q10-G21	αA1	N	3	Y	Y	N
A33-Y43	αB1	N	3	N	N	Y
P55-D65	αC1	N	3[d]	N	N	N
D76-N91	αD1	N	4	Y	N	N
P102-K113	αE1	N	3[d]	Y	N	N
A124-Q138	**αF1**[a]	Y	4	N	N	Y
N242-T254	**αA2**	Y	4	Y	Y	Y
Y264-Q273	**αB2**[b]	Y	3	N	N	Y
Q287-N294	αC2	Y	2	N	N	N
D308-M321	αD2	Y	4	Y	N	N
R332-Q340	αE2	Y	3[d]	Y	N	N
P350-R363	**αF2**[c]	Y	4	N	N	Y

[a] hinge helix 1
[b] interacts with the pore gate
[c] hinge helix 2
[d] broken helix
[e] questions the availability of a residue pair, both solvent-exposed and properly oriented for probe attachment chemistry
Note: promising reporter helices are highlighted in green.

The four identified reporter helix candidates were quantitatively examined to determine their θ and φ coordinates and the overall rotation angle Ω from one conformation to the other (Table 2.2). Since TrkA is a tetramer, each helix is observed four times in the TrkA structure, necessitating the calculation of four θ, φ and Ω values per helix per state; the table below summarized the average values for each helix in each of the two states. The calculated angle values confirm the initial observation that the αF1, αA2, αB2 and αF2 helices undergo substantial rigid body rotation as TrkA changes its conformation. Although the calculations suggest that the αF2 helix rotates only slightly in the θ and φ directions, the overall three-dimensional rotation of this helix is 13.2°, within the method's resolution limit.

Table 2. 2 – Calculated θ, φ and Ω values from the $\mathrm{TrkA_{flat}}$ and $\mathrm{TrkA_{twist}}$ structures

Helix ID	θ_{ave} values $\mathrm{TrkA_{flat}}$	 $\mathrm{TrkA_{twist}}$	 change	φ_{ave} values $\mathrm{TrkA_{flat}}$	 $\mathrm{TrkA_{twist}}$	 change	Ω_{ave} values
αF1	50.5°	71.1°	20.6°	74.6°	87.0°	12.4°	23.0°
αA2	21.6°	54.0°	32.4°	51.6°	41.5°	10.1°	33.0°
αB2	41.8°	71.8°	30.0°	21.1°	33.2°	12.1°	31.8°
αF2	66.7°	57.6°	9.1°	4.1°	7.2°	3.1°	13.2°

2.3.2 Purification of TrkA cysteine substitution mutants

All recombinant TrkA versions used in this study contained a C-terminal twin-strep-tag whose high affinity for streptavidin served a double purpose: (1) the tag first enabled us to obtain highly pure TrkA protein by an affinity purification step, which utilizes streptavidin-coated resin; (2) in subsequent polTIRF experiments the strep-tag anchored the fluorescently labeled TrkA to a streptavidin-coated glass surface. Successful purification of recombinant wild-type TrkA yielded 6.3 mg of protein for every 1 L of BL21(DE3) suspension culture grown (Figure 2.8A). High protein purity and lack of degradation are evident in the polyacrylamide gel image provided. When subjected to size exclusion chromatography, purified wild-type TrkA eluted at a volume corresponding to the size of ~245 kDa (Figure 2.8B), about four times the molecular weight of the individual TrkA subunit (54.4 kDa). We thus conclude that wild-type TrkA was purified in its tetrameric form.

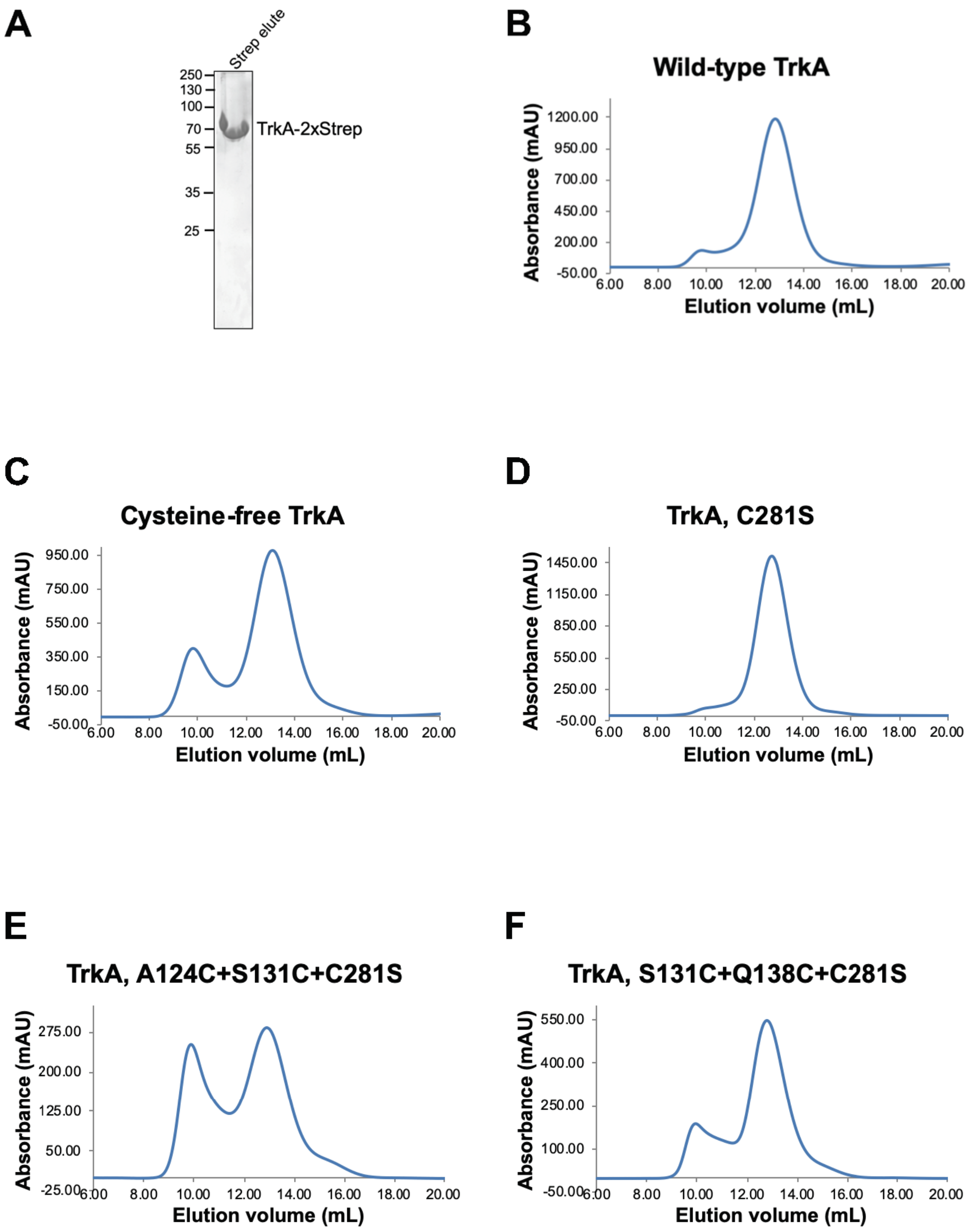
A
Strep elute
250
130
100
70
55
35
25
TrkA-2xStrep
B
Wild-type TrkA
Absorbance (mAU)
1200.00
950.00
700.00
450.00
200.00
-50.00
6.00
8.00
10.00
12.00
14.00
16.00
18.00
20.00
Elution volume (mL)
C
Cysteine-free TrkA
Absorbance (mAU)
950.00
750.00
550.00
350.00
150.00
-50.00
6.00
8.00
10.00
12.00
14.00
16.00
18.00
20.00
Elution volume (mL)
D
TrkA, C281S
Absorbance (mAU)
1450.00
1150.00
850.00
550.00
250.00
-50.00
6.00
8.00
10.00
12.00
14.00
16.00
18.00
20.00
Elution volume (mL)
E
TrkA, A124C+S131C+C281S
Absorbance (mAU)
275.00
200.00
125.00
50.00
-25.00
6.00
8.00
10.00
12.00
14.00
16.00
18.00
20.00
Elution volume (mL)
F
TrkA, S131C+Q138C+C281S
Absorbance (mAU)
550.00
400.00
250.00
100.00
-50.00
6.00
8.00
10.00
12.00
14.00
16.00
18.00
20.00
Elution volume (mL)

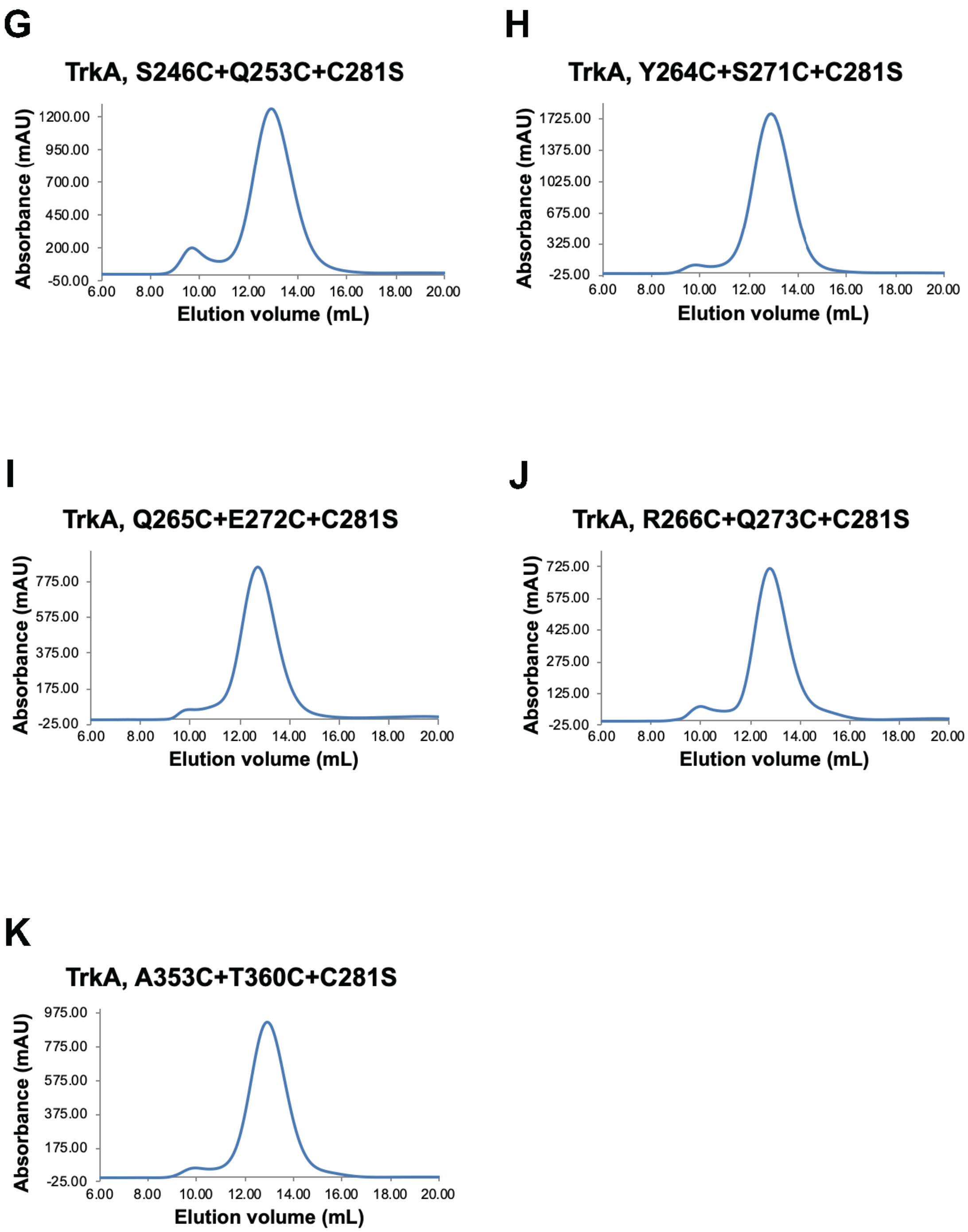

Figure 2. 8 – Purification of wild-type TrkA and various cysteine substitution mutants

(A) SDS-PAGE of affinity-purified wild-type TrkA protein from *V. parahaemolyticus*. **(B-K)** Superdex 200 size exclusion profiles of various test TrkA constructs.

To avoid covalent attachment of the fluorescent probe to the endogenous cysteine residues C83 and C281, we attempted to purify the cysteine-free TrkA protein C83S+C281S (Figure 2.8C). Although the expression and purification of this protein was successful, the purified cysteine-free mutant progressively aggregated, as evidenced by both the cloudiness of the affinity-purified sample (data not shown) and the sizable aggregation peak observed in the gel filtration profile. This finding suggests that one or both of the endogenous cysteine residues are important for TrkA's structural integrity. Given that C83 is a buried residue, whereas C281 is solvent-exposed, we surmised that the C83S mutation is the one causing protein aggregation and that the C281S mutation alone would be innocuous. Indeed, the purified C281S mutant was a tetramer (Figure 2.8D) and retained its oligomeric state for up to 3 days at 4 ^{o}C (data not shown). Moreover, this recombinant TrkA version and some of its derivatives remained tetrameric even after being frozen in liquid nitrogen, kept at -80 ^{o}C for up to 1 year and subsequently thawed (Figure 2.10A).

Using the C281S construct as background, several TrkA mutants were generated, for which certain pairs of amino acid residues within the αF1, αA2, αB2 or αF2 helix were replaced with cysteine pairs. All chosen residue pairs were spaced 7 amino acids apart in the primary sequence, such that the side chains of each pair point roughly in the same direction, achieving the necessary geometry for bifunctional rhodamine probe attachment. Seven such cysteine-pair mutants were purified successfully, and their oligomeric states were evaluated by size exclusion chromatography (Figure 2.8E-K). Both attempts at introducing a cysteine pair in the αF1 helix yielded protein that aggregated rapidly (Figure 2.8E, F). TrkA's sensitivity to mutations within the αF1 helix may be due to the importance of this helix for RCK dimer assembly and stability. All other purified cysteine-pair mutants were stable tetramers (Figure 2.8J-K), and could be frozen and thawed without impacting the oligomeric state (data not shown).

2.3.3 Mock labeling experiments with TrkA and the 5-TMRIA probe

Following protein purification, wild-type TrkA or its various mutant versions were allowed to react with excess amount of the monofunctional rhodamine dye tetramethylrhodamine-5-iodoacetamide (5-TMRIA) in order to determine their labeling efficiency (Table 2.3). In all tested samples, a significant portion of the protein aggregated with the fluorescent probe (Figure 2.9A-H), possibly due to the low solubility of this probe in aqueous buffers and its tendency to noncovalently attach to protein hydrophobic patches, such as ones that may become exposed in partially unfolded TrkA. Nevertheless, tetrameric TrkA peaks with co-migrating dye peaks were observed for wild-type and all but two of the TrkA mutants tested.

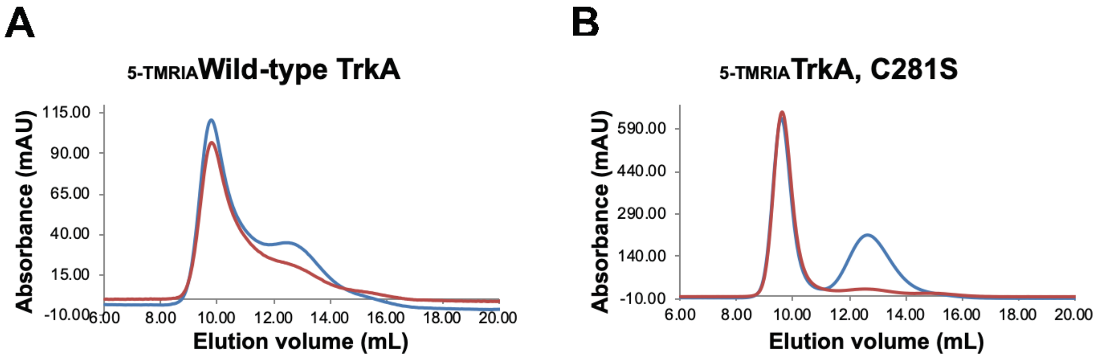

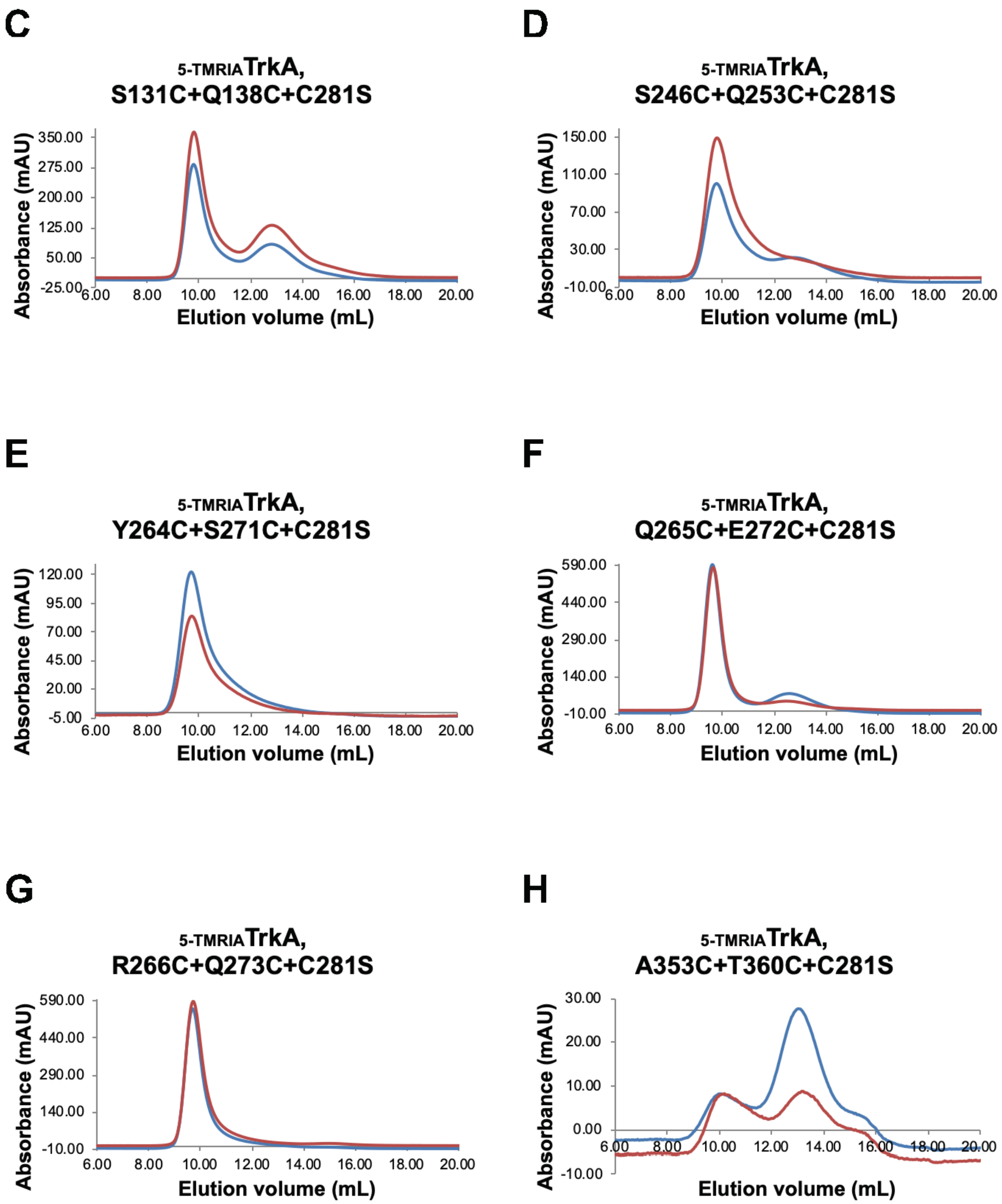

Figure 2. 9 – Mock labeling of TrkA with the monofunctional rhodamine probe 5-TMRIA

All chromatograms were produced by running fluorescently labeled TrkA samples through a Superdex 200 10/300 GL size exclusion column. Blue traces (A280nm) follow the protein and red traces (A550nm) track the fluorescent dye.

As expected, wild-type TrkA reacted with the fluorescent probe (Figure 2.9A), and endogenous labeling was greatly reduced by replacing the exposed C281 residue with serine, resulting in a 5-fold labeling efficiency decrease from 19.1% to 4.0% (Figure 2.9B; Table 2.3). Although the highest labeling efficiency (48.3%) was achieved with the C131+C138 pair in the αF1 helix, the labeled protein aggregated rapidly (Figure 2.9C). Given our earlier observation that the S131C+Q138C+C281S mutant tends to aggregate even in the absence of dye (Figure 2.8F), it is likely that the impressive labeling efficiency for this mutant results from its instability: local protein unfolding at the level of the αF1 helix may increase the probe's access to the intended probe-reactive sites, while potentially occurring global unfolding may expose the otherwise buried C83 residue and make it available for probe attachment as well. Introducing the C246+C253 pair in the αA2 helix also resulted in high labeling efficiency (27.2%), but the labeled protein was also prone to aggregation (Figure 2.9D), suggesting that reaction with the fluorescent probe destabilizes the S246C+Q253C+C281S mutant. This notion is consistent with an earlier remark that the αA2 helix plays an important structural role in stabilizing the RCK dimer by interacting with the sister αF1 helix. The S131C+Q138C+C281S and S246C+Q253C+C281S mutants were thus dropped from further consideration, due to their post-labeling instability. Out of three tested cysteine pair combinations within the αB2 helix, only the Q265C+E272C+C281S mutant yielded a tetrameric protein peak that comigrates with a dye peak (Figure 2.9E-G). Similarly, labeling the C353+C360 pair within the αF2 helix was successful and yielded stable tetrameric TrkA (Figure 2.9H). The labeling efficiencies for the two mutants were 15.5% and 15.9%, respectively, nearly four-fold above background (Table 2.3). Since the TrkA structures predict that the αB2 helix rotates by a much greater degree than the αF2 helix (Table 2.2), we chose to rely on the Q265C+E272C+C281S mutant for our polTIRF data collection.

Table 2. 3 – Summary of experimental search for appropriate probe attachment sites in TrkA

TrkA construct	Oligomeric state		% Labeled subunits
	Pre-label	Post-label	
wild-type	ST[a]	ST	19.1
C83S, C281S	Ag[b]	n/a	n/a
C281S	ST	ST	4.0
A124C, S131C, C281S	Ag	n/a	n/a
S131C, Q138C, C281S	UT[c]	UT	48.3
S246C, Q253C, C281S	ST	UT	27.2
Y264C, S271C, C281S	ST	Ag	n/a
Q265C, E272C, C281S	ST	ST	15.5
R266C, Q273C, C281S	ST	Ag	n/a
A353C, T360C, C281S	ST	ST	15.9

[a] ST = Stable Tetramer
[b] Ag = Aggregate
[c] UT = Unstable Tetramer

2.3.4 Reducing signal contribution from undesired probe attachment sites on TrkA

For the purpose of single-molecule data collection, it was necessary to ensure that the recorded fluorescent signal comes from the desired helix and only one such reporter helix is observed per regulatory module. To increase the likelihood that only one out of the four αB2 helices in TrkA becomes labeled, we purified the protein from BL21(DE3) cells that had been co-transformed with 3 units of DNA encoding the C281S mutant and 1 unit of DNA encoding the Q265C+E272C+C281S mutant (Figure 2.10A). We predict that this expression strategy yields a heterologous population of TrkA heterotetramers, with all 4 subunits containing the C281S mutation, while 0 to 4 subunits additionally contain the Q265C+E272C mutation pair. For clarity, we can symbolically represent these mutant heterotetramers as $(C281S)_4(Q265C+E272C)_n$, where n = 0, 1, 2, 3 or 4. If we assume that BL21(DE3) competent cells easily engulf four or more plasmid DNA copies, we can expect that the predominant protein species in a purified sample would be of the (C281S)$_4$(Q265C+E272C)$_1$ form. However, previous experience with *E. coli* co-transformations suggests to us that a competent cell is ~10 times less likely to absorb two distinct plasmids than it is to absorb a single plasmid; there is no published or anecdotal evidence revealing how much less likely it is for competent cells to engulf three or more plasmids. In the absence of formal studies on the subject matter, we cannot predict what proportion of our TrkA sample is in the (C281S)$_4$(Q265C+E272C)$_1$ form, but we have high confidence that this particular mutant species is well-represented in the mixed TrkA population. Notably, during the initial phases of single-molecule data analysis, we discard any particles that exhibit more than one photobleaching steps, ensuring that we predominantly retain data recorded from the (C281S)$_4$(Q265C+E272C)$_1$ species (see Section 2.2.6.4).

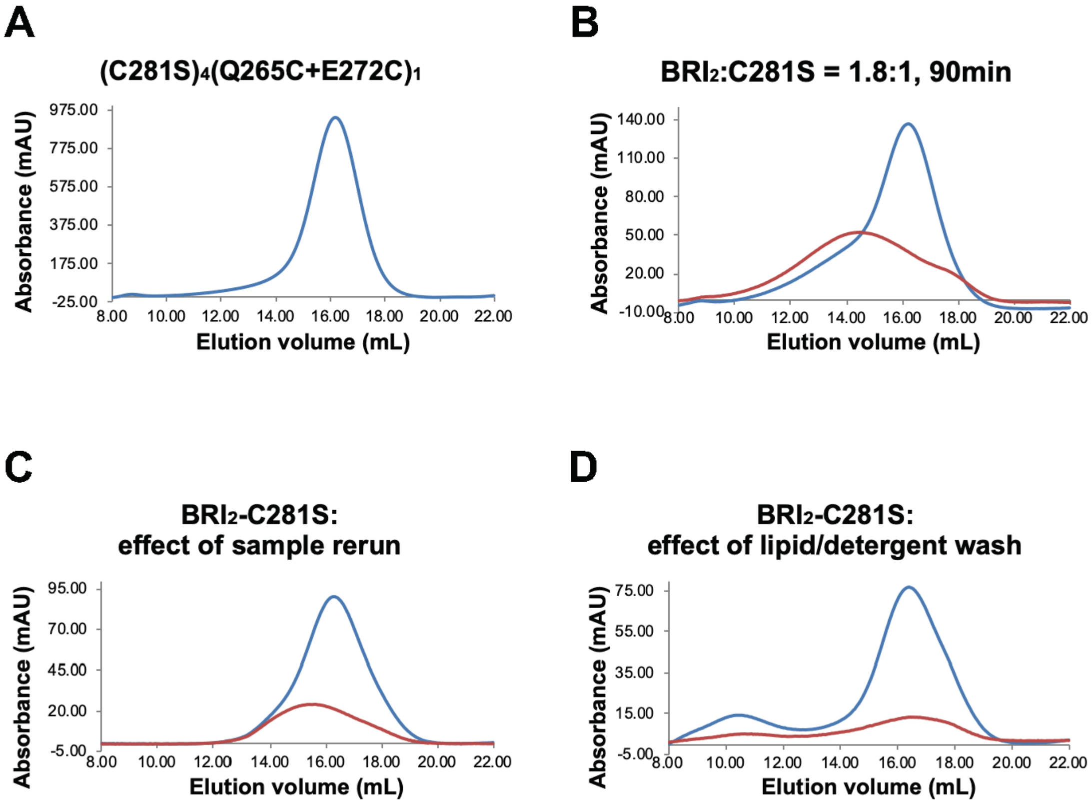

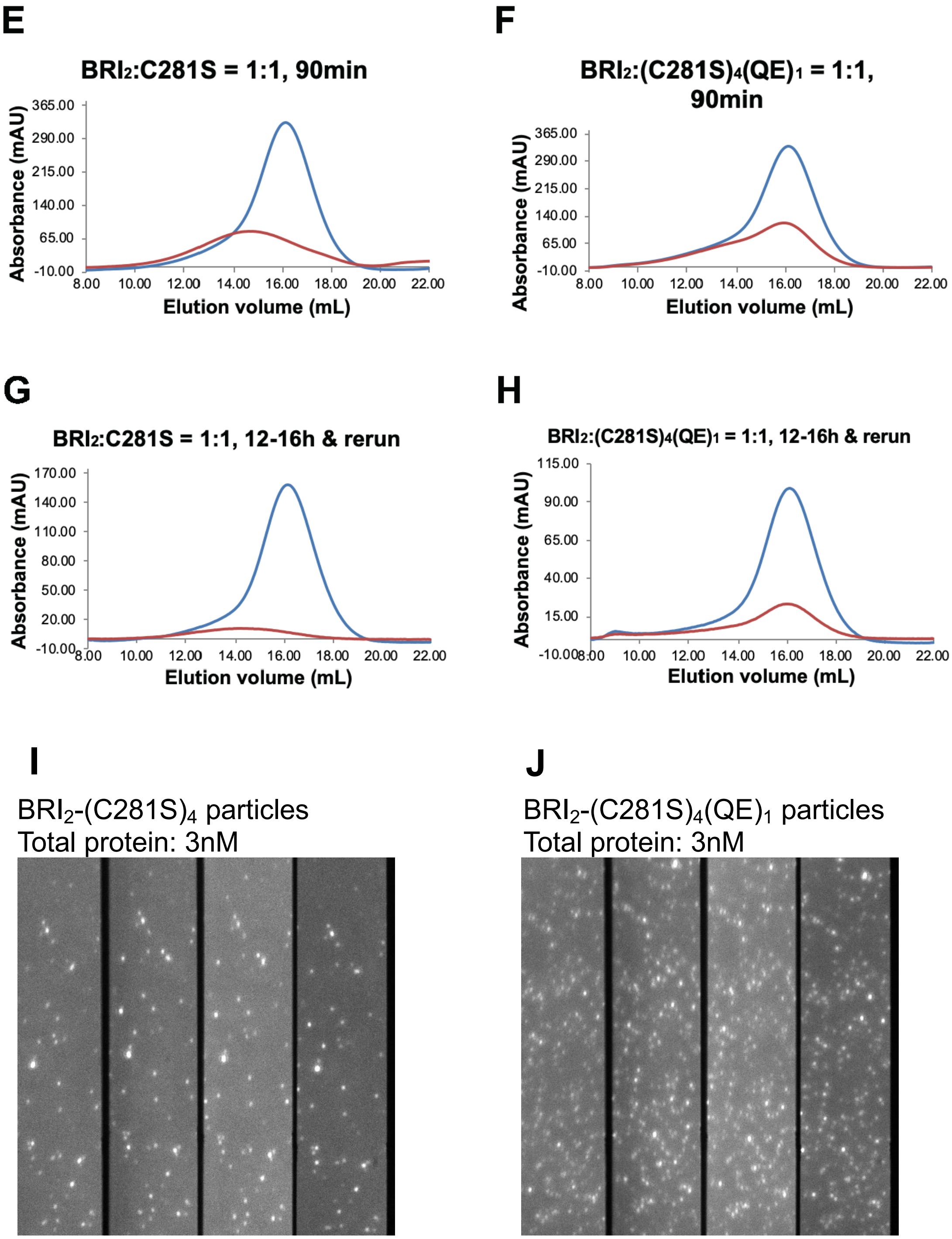

Figure 2. 10 – Reducing off-target fluorescent labeling in TrkA

(A) Purification of the TrkA construct, used in single-molecule recordings. **(B-H)** Optimization of procedure for labeling TrkA with bifunctional rhodamine probe BRI_2. **(I,J)** 5-fold bright particle count increase in the presence of the Q265C+E272C mutation pair. The four panels in each image correspond to the four split emission intensity components.

Unlike our pilot labeling experiments where the 5-TMRIA monofunctional rhodamine probe was used (Section 2.3.3), single-molecule experiments necessitated that we use a probe with bifunctional attachment mode, such as bis-((N-iodoacetyl)piperazinyl)-sulfonerhodamine (BRI_2), ensuring that the fluorescent signal's emission dipole is reliably aligned with the long axis of the reporter helix. Since initial labeling studies had indicated that 4.0% of C281S mutant subunits retain the 5-TMRIA dye (Table 2.3), we wished to determine the degree of unintentional labeling with BRI_2 as well. In a reaction setup identical to the one used for our mock labeling experiments, 9.0% of C281S mutant subunits retained the BRI_2 dye (Figure 2.10B), raising the undesired prospect that during single-molecule data collection, the signal recorded from the intended site on the αB2 helix would be substantially contaminated with signal from an unknown probe attachment site. To ameliorate this problem, we sought to better understand the nature of off-target labeling in the C281S mutant and optimize the labeling protocol accordingly.

The peak gel filtration fractions from the labeled TrkA sample (Figure 2.10B) were pooled, concentrated and reran through the Superose 6 column (Figure 2.10C). The observed 10% decrease in endogenous labeling suggests that at least some of the dye carried by TrkA is non-covalently attached. In fact, BRI_2's partially hydrophobic nature makes it likely that the dye would lodge in small hydrophobic crevices on target proteins. To test whether hydrophobic interactions are responsible for some of the unintentional probe attachment, labeled C281S mutant was treated with a non-denaturing lipid/detergent mix (Figure 2.10D). Following 1-hour incubation in the presence of 2 mg/mL PC:PE:PG (3:1:1) lipid mix and 20 mM DDM detergent, the amount of labeled protein decreased nearly 2-fold (from 9.0% to 5.2%). Since the lipid/detergent wash strategy proved more effective in fluorescent dye removal than the aqueous wash, it appears likely that endogenous TrkA labeling mainly arises from hydrophobic interactions between the probe and protein. Importantly, demonstrating that 10-40% of dye can be removed from the C281S mutant supports that probe attachment to unintended sites on TrkA is a readily reversible process. Consistent with this notion, reducing the BRI_2 amount in the labeling reaction from 1.8 to 1 dye molecule per regulatory module decreased endogenous labeling by 30% (from 9.0% to 6.1%; Figure 2.10E).

We next compared the labeling efficiencies of the C281S and $(C281S)_4(Q265C+E272C)_1$ mutants with the BRI_2 dye (Figure 2.10E, F), and observed that the presence of a probe-reactive αB2 helix only increases the percentage of labeled subunits 2-fold. Rerunning each sample through the Superose 6 column decreased C281S labeling to 4.9% and $(C281S)_4(Q265C+E272C)_1$ labeling to 10.5%, maintaining the 2-fold labeling efficiency difference between the two mutants (data not shown). Unlike the unintentional probe attachment discussed above, BRI_2 attachment to the αB2 helix is covalent and hence not reversible, making it likely that given enough incubation time, the probe will leave the off-target sites on TrkA and react with the target helix irreversibly, thus increasing the instances of desired labeling events. Indeed, increasing the reaction duration from 90 min to 12-16 h combined with running the labeled samples through the Superose 6 column twice, resulted in ~6 times more labeled subunits for the $(C281S)_4(Q265C+E272C)_1$ mutant than the C281S mutant (Figure 2.10G, H). The latter labeling procedure was followed for all BRI_2-TrkA preparations used in subsequent single-molecule polTIRF studies. We confirmed the superior labeling of the $(C281S)_4(Q265C+E272C)_1$ mutant by observing 3nM samples of each protein type under polTIRF and noting the presence of 5-10 times more particles when a probe-reactive αB2 helix is present (Figure 2.10I, J). Subsequent analysis of the recorded images revealed that fluorescent signals detected from the C281S mutant are on average 2 times dimmer than those measured from the $(C281S)_4(Q265C+E272C)_1$ mutant. Thus, even though unintentional probe attachment sites might still contribute 10-20% of the recorded signal, undesired signals can be filtered out by imposing a proper intensity cutoff.

2.3.5 Determining the apparent anisotropy of fluorescently labeled TrkA in solution

To experimentally determine the attached fluorophore's apparent anisotropy, r_{app}, we measured the anisotropy, r, of BRI_2-TrkA in solutions of increasing viscosity (see Section 2.2.6.3). Our measurements did not change significantly over a broad range of glycerol concentrations (0-50%), suggesting that TrkA tumbles too slowly to affect the observed anisotropy values. In this case, our experiment directly reports r_{app}, which we estimate as the average from all measurements in the 0-50% glycerol range: $r_{app} = 0.262 \pm 4.56E\text{-}3$. Previously, the equivalent experiment with the MthK regulatory module, labeled at a single target cysteine residue, yielded $r_{app} \approx 0.34$, significantly greater than the value we have obtained with the BRI_2-TrkA sample. This comparison suggests that the majority of the BRI_2 probe on TrkA has reacted with only one of the two cysteine residues at the target site. From this bulk experiment, we cannot determine whether any fluorophore molecules have attached in a bifunctional manner; however, this information should become readily available upon ensemble analysis of the single-molecule data. Since the r_{app} values for a mono- versus bifunctionally attached probe would differ significantly, and the calculated θ is dependent on r_{app}, a mixture of two differentially labeled protein species would be reflected by the θ ensemble distributions (see Section 2.3.7). Indeed, each of the three state distributions in Figure 2.12B is asymmetric and contains a dominant peak, followed by a much smaller secondary peak with a slightly greater θ mean. We have determined that these double peaks result from mixing two particle populations, which we can separate reasonably well by imposing a ~55° cutoff on θ. Based on their comparable state probabilities and Ω values, these populations are likely related and can be safely merged. In the interest of calculating θ as accurately as possible, we must apply different wobble corrections to these two populations (see X_4 in Equation 2.18) prior to merging them. We are currently in the process of creating an algorithm that performs this operation on a large number of particles. In the meantime, since the wobble phenomenon has no bearing on state assignment or the state probabilities, we have chosen to proceed with model derivation, while temporarily accepting the slightly compromised θ accuracy.

2.3.6 Single-molecule recordings from individual RCK units in the isolated TrkA gating ring

TrkA tetramers of the $(C281S)_4(Q265C+E272C)_1$ mutant type were labeled with the BRI_2 fluorescent probe and attached to a streptavidin-coated glass surface through the C-terminal strep-tags of individual TrkA subunits. The conformational changes in one of the eight RCK units in each regulatory module were captured in real-time by simultaneously recording the four emission intensity components I_0, I_{45}, I_{90} and I_{135}, as described above (Section 2.2.5). Figure 2.11A displays the time dependence of the four intensity components measured from one example TrkA particle, as well as the time dependence of the total emitted intensity and probe orientation angles θ, φ and Ω, calculated with Equations 2.14-16 and 2.22 above. The obvious difference in intensity values in the I_0-I_{90}, as well as the I_{45}-I_{135} panel, suggests robust signal polarization. Each polarized intensity component varies as a function of time, resulting in a time-dependent variation of the calculated θ and φ values with clearly detectable event transitions. Intraevent averaged data points were next subjected to our state identification algorithm (Section 2.2.6.4), which determined the most probable number of states and ultimately sorted the detected events into three well-resolved states: S_1, S_2 and S_3 (Figure 2.11B). This analysis was performed separately for each individual TrkA particle prior to calculating ensemble means.

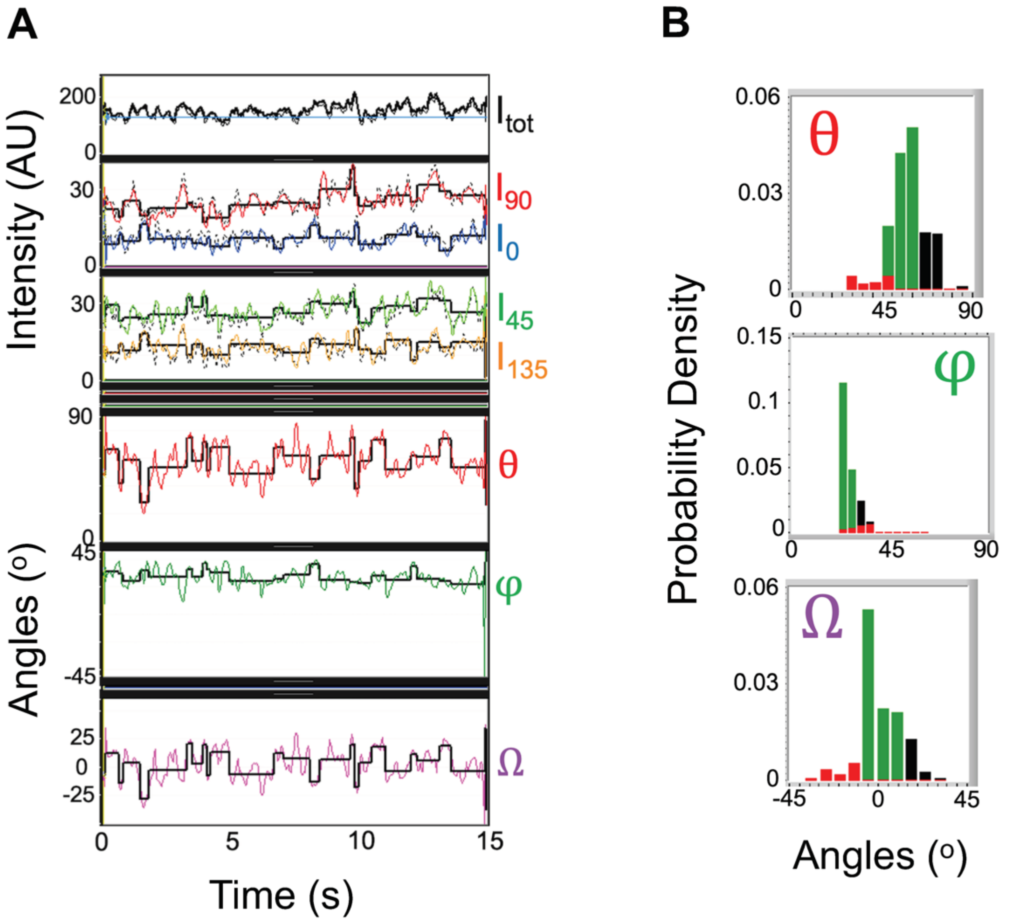

Figure 2. 11 – Primary data output from a single BRI_2-TrkA particle

(A) Time dependence of the total emission intensity (I_{tot}) and its four measured polarized components (I_0, I_{90}, I_{45} and I_{135}), along with the calculated angle values θ, φ and Ω at every timepoint. Black traces represent time-averaged data points for each particular event. **(B)** Three well-resolved states (S_1 in red, S_2 in green and S_3 in black) and their θ, φ and Ω probability distributions in a single particle.

2.3.7 Relating identified states to known TrkA crystal structures

Prior to relating the experimentally identified conformational states to the known TrkA crystal structures, we determined the ensemble means for θ and Ω from a large number of individually analyzed molecules (Figure 2.12). Unlike the well-resolved single-molecule θ distributions, the ensemble averaged $\theta_{1\text{-}3}$ distributions are very broad and overlap substantially. Since ensemble averaging does not affect the Ω resolution nearly as much, we suspect the primary cause for θ distribution broadening is the variation in absolute orientation of individual TrkA molecules on the glass surface. As described in Section 2.3.5 above, the broad θ distributions may also be a consequence of observing a mixed population of bifunctionally and monofunctionally labeled protein targets. Regardless of the effect of ensemble averaging on the resolvability of θ and Ω, we are confident in the precision of our angle calculation and state identification, which are performed on a molecule-by-molecule basis rather than at the ensemble level. The sole purpose of ensemble averaging is thus to improve the accuracy of angle calculations. Future efforts will be made to further improve the θ accuracy by implementing appropriate wobble corrections (see Section 2.3.5).

The calculated ensemble means for the S_1 and S_3 states were consistent with the ones predicted from the $\text{TrkA}_{\text{flat}}$ and $\text{TrkA}_{\text{twist}}$ structures, respectively (Figure 2.12). The predominant state S_2, on the other hand, is a novel state that has not been previously observed or structurally characterized.

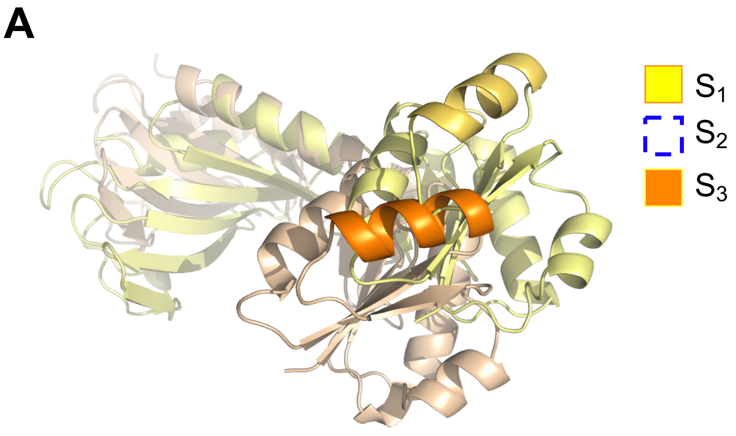

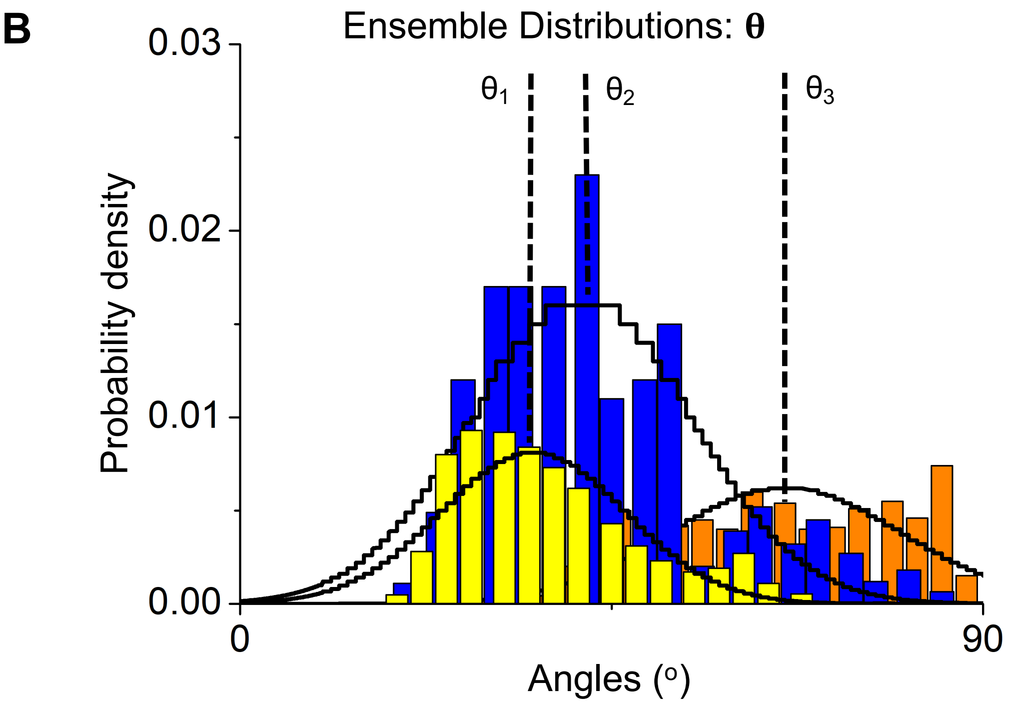

	θ1	θ2	θ3
Crystallography	42°	n/a	72°
Polarization	38°±11°	44°±13°	72°±14°

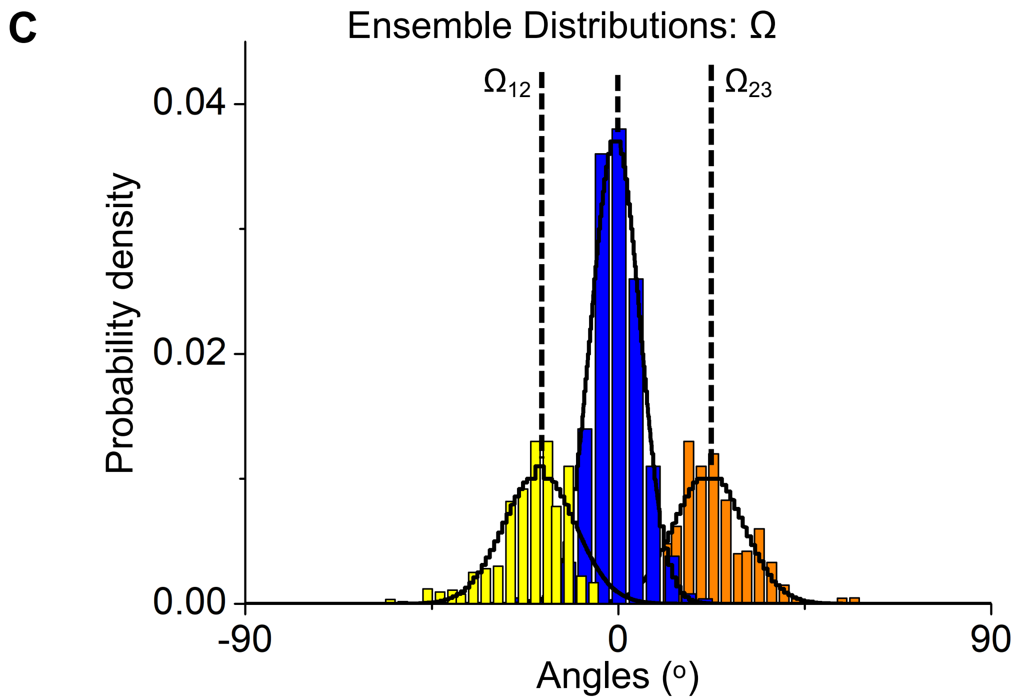

	Ω_{12}	Ω_{13}	Ω_{23}
Crystallography	n/a	39°	n/a
Polarization	21°±11°	43°±17°	22°±10°

Figure 2. 12 – Structural alignment between two RCK2 conformations and ensemble distributions of θ and Ω

(A) Alignment of RCK2 units from the $\text{TrkA}_{\text{flat}}$ (PDB: 4J9U) and $\text{TrkA}_{\text{twist}}$ (PDB: 4J9V) structures with the αB2 reporter helix highlighted in yellow and orange, respectively. **(B, C)** Ensemble distributions of three θ **(B)** or Ω **(C)** angles, constructed with data obtained from 335 rhodamine-labeled TrkA particles in the absence of ligand. Black Gaussian curves were calculated from the respective angle mean and σ values. Below each distribution is a comparison of the angle values, calculated from the structure, against experimentally determined angle values (mean ± σ, calculated from the data). The number of events, comprising each state distribution is as follows: S_1 – 1,250 events, S_2 – 1,775 events, and S_3 – 1,194 events.

2.3.8 Ligand-induced conformational changes in the isolated TrkA gating ring

In a final set of experiments, we demonstrated that the observed RCK unit state probabilities depend on [AMP-PNP] and [ADP] (Figure 2.13A-E; Table 2.4). Due to expected instability of the ATP ligand, which is known to slowly hydrolyze to ADP and phosphate in aqueous solutions, we chose to activate TrkA with the non-hydrolysable ATP analog AMP-PNP in all single-molecule experiments. In the absence of ligand, the state probabilities for S_1, S_2 and S_3, are ${}_{apo}P_1 = 0.228$, ${}_{apo}P_2 = 0.551$, and ${}_{apo}P_3 = 0.222$, respectively (Table 2.4).

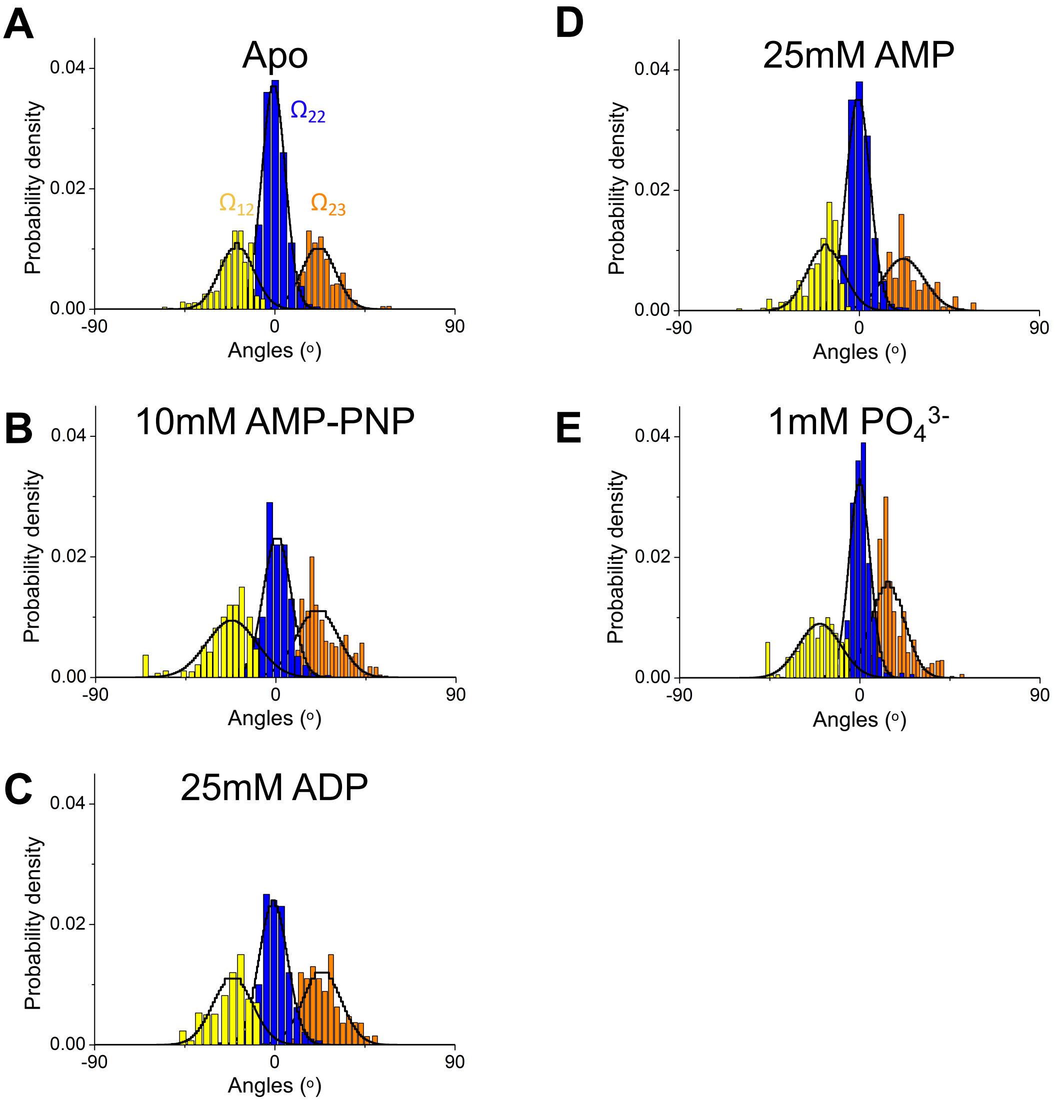

Figure 2. 13 – Ligand dependence of RCK state probabilities in the isolated TrkA gating ring

(A-E) Ω distributions in the absence of ligand **(A)** or at saturating concentrations of AMP-PNP **(B)**, ADP **(C)**, AMP **(D)** or inorganic phosphate **(E)**. Black Gaussian curves were calculated from the respective angle mean and σ values.

Table 2. 4 – Summary of RCK state probability ligand dependence in the isolated TrkA

	S1		S2		S3		Total # particles
	Probability[a]	# events	Probability[a]	# events	Probability[a]	# events	
0 mM Ligand	0.228 ± 1.18E-2	375	0.551 ± 1.40E-2	540	0.222 ± 1.17E-2	331	102
10 mM AMP-PNP	0.298 ± 1.25E-2	365	0.408 ± 1.34E-2	559	0.295 ± 1.25E-2	410	103
25 mM ADP	0.278 ± 1.50E-2	277	0.427 ± 1.65E-2	362	0.296 ± 1.52E-2	256	65
25 mM AMP	0.245 ± 1.29E-2	326	0.530 ± 1.50E-2	480	0.225 ± 1.26E-2	298	94
1 mM PO_4^{3-}	0.237 ± 1.44E-2	239	0.429 ± 1.68E-2	333	0.334 ± 1.60E-2	299	74

[a] Probabilities calculated from the number of observed events per state, relative to the total number of events. Standard errors calculated based on variance in measurements from a multinomial distribution.

AMP-PNP increased the $P_{1,3}$ probabilities and decreased the P_2 probability to the new values $_MP_1$ = 0.298, $_MP_2$ = 0.408, and $_MP_3$ = 0.295. Surprisingly, the effect of ADP on all three state probabilities was nearly identical to that of AMP-PNP, consistent with the inability of TrkA to discriminate between these two ligands (Figure 2.13A-C). In agreement with the electrophysiology studies on TrkAH, AMP had no effect on the state probabilities of individual RCK units in TrkA (Cao et al., 2013; Figure 2.13D). This latter observation suggests that the nearly identical effects of AMP-PNP and ADP are exerted on TrkA through the β-phosphate rather than the α-phosphate or adenosine group. Consistent with the idea that the isolated gating ring recognizes and responds to a single properly positioned phosphate, the effect of PO_4^{3-} on the state probabilities was nearly identical to that of AMP-PNP and ADP (Figure 2.13E).

2.4 Discussion

In the experiments reported above, we sought to satisfy all necessary prerequisites for successful single-molecule studies on TrkA. Our structural analysis and subsequent purification and labeling optimization revealed that the most viable probe attachment site on TrkA is the αB2 helix in the RCK2 motif. Collecting data from TrkA, labeled at the αB2 helix, has the added advantage of observing the gating ring component that is closest to the pore gate. According to the whole-channel structure (TrkA$_{\text{flat}}$, PDB: 4J9U), this helix is the docking site for the pore module and a direct point of contact with the pore gate. Furthermore, single-molecule experiments with the MthK gating ring tracked the equivalent helix αB, precisely because this helix is located closest to the pore gate. By observing equivalent structural elements in each gating ring, we are in the best position to directly compare the experimental findings from the Trk and MthK systems.

We demonstrate that the signal recorded from fluorescently labeled TrkA is long-lasting and polarized, with clearly detectable transitions and enough events per particle to ensure reliable state identification on a particle-by-particle basis. Statistical analysis reveals that the tracked RCK unit visits three states (S_1, S_2 and S_3) and ensemble averaging yields accurately calculated θ and Ω angles that allow us to link S_1 and S_3 to the TrkA$_{\text{flat}}$ and TrkA$_{\text{twist}}$ structures, respectively. Importantly, the observed state probabilities exhibit clear AMP-PNP and ADP dependence, as each ligand increases the populations of S_1 and S_3 and decreases the population of S_2.

The unexpectedly identical TrkA response to AMP-PNP and ADP prompted us to examine closely the ligand binding pockets in the two known structures. We found that in the TrkA$_{\text{flat}}$ structure, where each RCK2 core binds one NADH molecule, the phosphate binding consensus sequence backbone closely contacts the ligand's diphosphate region, as expected (Bellamacina et al., 1996; Figure 2.14A). In the ATP-γS-bound TrkA$_{twist}$ structure, on the other hand, neither the RCK1 nor the RCK2 phosphate binding consensus sequence is in close contact with the phosphate groups of the ligand (Figure 2.14B, C). Instead, the ATP-γS β-phosphates in RCK1 and RCK2 are stabilized by interactions with the R100 and N306 residues, respectively, and no stabilizing contacts are provided for the γ-phosphates. From these observations, it appears that a gating ring in the TrkA$_{twist}$ configuration would not be able to discriminate between ATP and ADP.

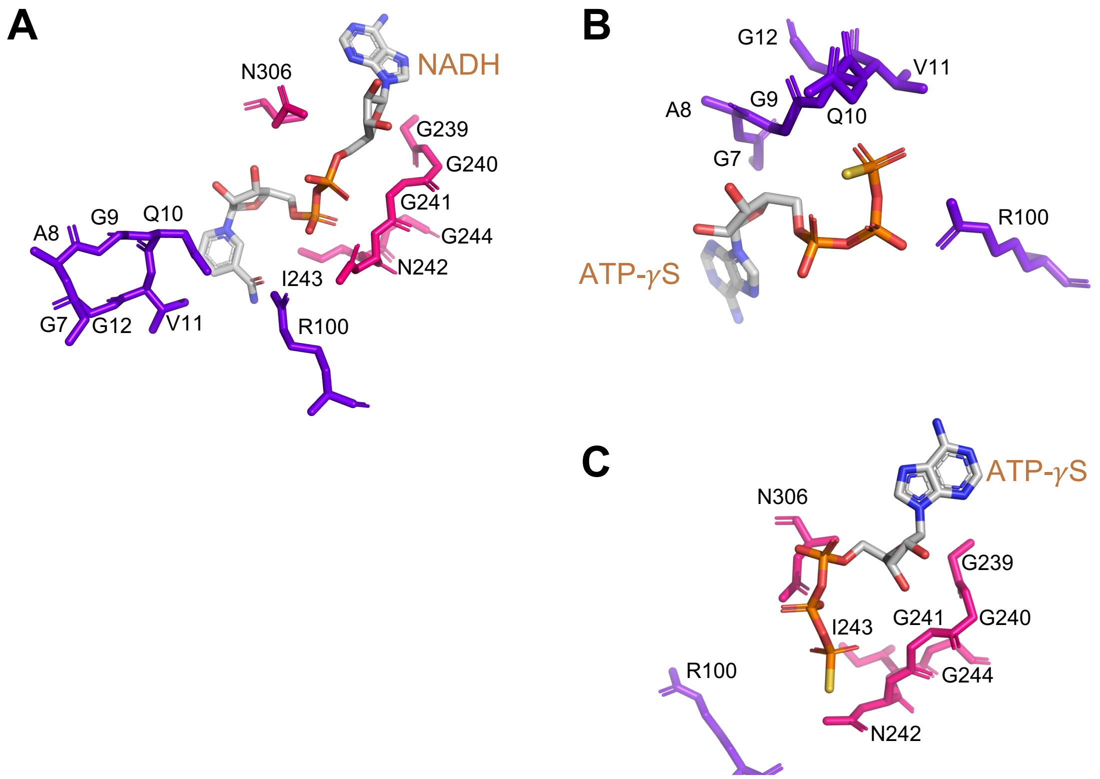

Figure 2. 14 – Structural analysis of the TrkA ligand binding pockets

(A) RCK2 binding pocket, occupied by NADH (PDB: 4J9U). The GGGNIG consensus sequence closely lines the ligand's diphosphate region. R100 from RCK1 points into the RCK2 binding pocket. **(B)** RCK1 binding pocket, occupied by ATP-γS (PDB: 4J9V). The GAGQVG consensus sequence does not contact the ligand's phosphate groups. R100 coordinates the β-phosphate in its own binding pocket. **(C)** RCK2 binding pocket, occupied by ATP-γS (PDB: 4J9V). The GGGNIG consensus sequence does not contact the ligand's phosphate groups. N306 interacts with the β-phosphate.

A very recent publication presents the whole-channel TrkAH structure bound to ADP, ATP or ATP-γS and reveals that, in the presence of the pore module, TrkA binds 8 ATP-γS, but only 4 ADP molecules (Zhang et al., 2020). According to this structural report, the RCK2 binding site provides identical stabilizing contacts for ATP-γS as for ADP with residues N306 and N242 coordinating the α- and β-phosphates, respectively; no stabilizing contacts are provided for the γ-phosphate of ATP-γS in RCK2. The RCK1 binding site, on the other hand, can only be occupied by ATP-γS, and residues R98 and R100 form salt bridges with the γ- and β-phosphate, respectively. In light of this recent structural report and the above analysis on the isolated TrkA structure, we conclude that the gating ring must be associated with the pore module in order to respond differently to ATP and ADP. Since, unlike MthK, the TrkAH whole-channel behavior cannot be directly deduced from observations on the isolated gating ring, we were prompted to carry all subsequent experiments in the presence of TrkH.

CHAPTER 3: DERIVING AN ENERGETIC MODEL FOR TRK ION CHANNEL GATING

Author Contributions

Purification of TrkA and TrkH, nanodisc assembly and data collection were performed by Valentina Dimitrova. Scaffold protein purification and lipid reconstitution were carried by Yufeng Zhou. Valentina Dimitrova and John Lewis analyzed the single-particle data. Model derivation and validation were performed by Valentina Dimitrova, John Lewis and Zhe Lu.

3.1 Introduction

3.1.1 Single-channel properties of TrkAH

The regulatory module TrkA controls the opening of the pore module TrkH in a ligand-dependent manner. TrkH is a transmembrane homodimer and each of its two 54kDa subunits contains an ion permeation pathway, selective for K^+ and Rb^+ over smaller ions such as Na^+ and Li^+ (Cao et al., 2011). Each TrkH subunit contains 18 α-helices that can be grouped into five tandem domains D0–D5 (Figure 3.1A). All helices, except for the two within D0, assemble into a core structure that resembles the canonical TM1-P-TM2 core of simple K^+ channels (Zhou et al., 2001) with some prominent distinctions. Unlike the KcsA pore with genuine fourfold symmetry, the TrkH pore is only pseudo-fourfold symmetric due to the low homology between domains D1 to D4. In addition, the signature sequence TVGYG, which forms the selectivity filter of KcsA, is only weakly conserved in the TrkH P-loops. Compared to the KcsA selectivity filter, that of TrkH has a significantly shorter constricted region for K^+ coordination with one crystallographically confirmed and two putative K^+ binding sites along the ion conduction pathway. Importantly, a TrkH feature completely absent in KcsA is a highly conserved intramembrane loop that breaks the pore-lining M2 helix in domain D3 and inserts into the ion permeation pathway, preventing K^+ in the selectivity filter to move inwardly. Thus, the TrkH gating mechanism must be notably different from that of KcsA and likely involves conformational changes that pull the D3M2a-D3M2b loop out of the ion permeation pathway. In fact, just C-terminal to the D3M2b helix lies a cytosolic loop region that directly interacts with the TrkA gating ring and likely couples intramembrane loop displacement to conformational changes in the regulatory module (Cao et al., 2013; Figure 3.1B).

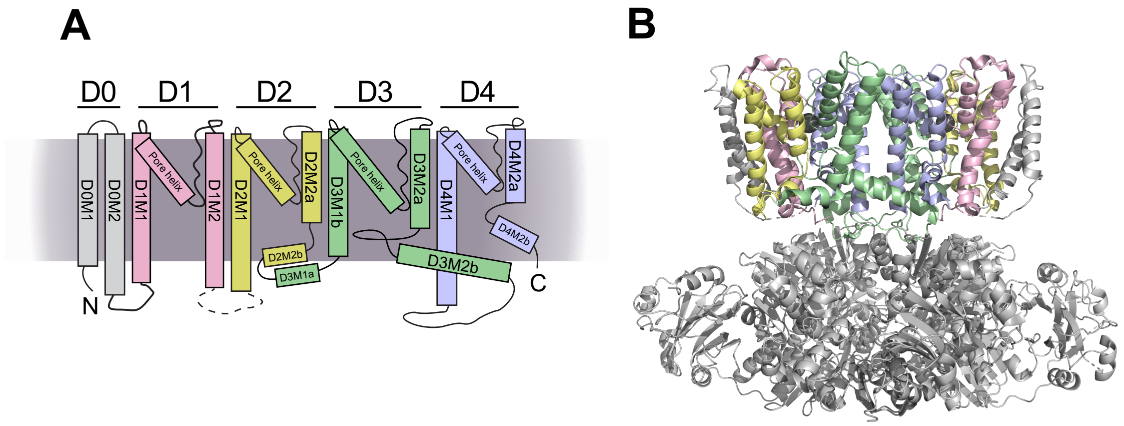

Figure 3. 1 – Structure of the pore module TrkH

(A) Transmembrane topology of TrkH, shown with the cytosolic side on the bottom. **(B)** Crystal structure of the TrkAH ion channel (PDB: 4J9U). The five tandem domains are colored according to the scheme in panel (A). Figure adapted from Cao et al., 2011.

Single-channel recordings from the TrkAH complex in the absence of ligand demonstrate prolonged closures interrupted with occasional channel activity bursts, during which the current alternates between two levels, differing in amplitude by a factor of 2 (Cao et al., 2013). Importantly, the higher of the two conductance levels is the entry and exit point for nearly all activity bursts and the open channel is about equally as likely to be in a single- as in a double-conducting state. Together, these observations suggest that both TrkH pores can exist in a conducting state and that they are coupled at the initiation and termination of each channel activity burst, as well as partially coupled during bursts. The properties of activity bursts are altered in the presence of ATP and ADP, with ATP increasing burst frequency and duration and ADP having the opposite effect. A detailed inspection of single-channel traces from liganded TrkAH shows that ATP preserves the ~50-50 split between the single- and double-conducting states, whereas ADP only favors occasional, nearly instantaneous visits to the double-conducting state, followed by channel closing.

3.1.2 Theoretical predictions for TrkA-mediated ligand effects on the TrkH open probability

ATP and ADP regulate the open probability of TrkAH in a dose-responsive manner (Figure 3.2). The P_o dependence on the concentration of each ligand, [L], can be fitted with a version of the Hill approximation (Hill, 1910), derived by assuming a simple model for ligand-dependent channel opening (Figure 3.2A):

$$P_o = \frac{{}_{apo}P_o + {}_{L}P_o\left(\frac{[L]}{EC_{50}}\right)^n}{1 + \left(\frac{[L]}{EC_{50}}\right)^n}$$

3. 1 – Generic Hill fit expression

where ${}_{apo}P_o$ and ${}_{L}P_o$ are the open probabilities for the unliganded and fully-liganded channel species, respectively, and *n* is the Hill coefficient, related to the number of ligand binding sites and reflecting ligand binding cooperativity. The minimum and maximum P_o, EC_{50} and slope are the four defining features for the P_o vs [ATP] and P_o vs [ADP] dose-response curves. ATP increases the P_o from 0.17 to 0.87 with an EC_{50} = 0.7 mM and

n_{ATP}=3.4, whereas ADP reduces the P_o from 0.17 to 0.015 with an EC_{50} = 0.9 mM and n_{ADP}=1.7. The comparable EC_{50} values indicate that TrkA has similar affinities for the two ligands; the two-fold difference between n_{ATP} and n_{ADP} is consistent with the recently reported finding that the Trk gating ring likely binds twice as many ATP as ADP molecules (Zhang et al., 2020).

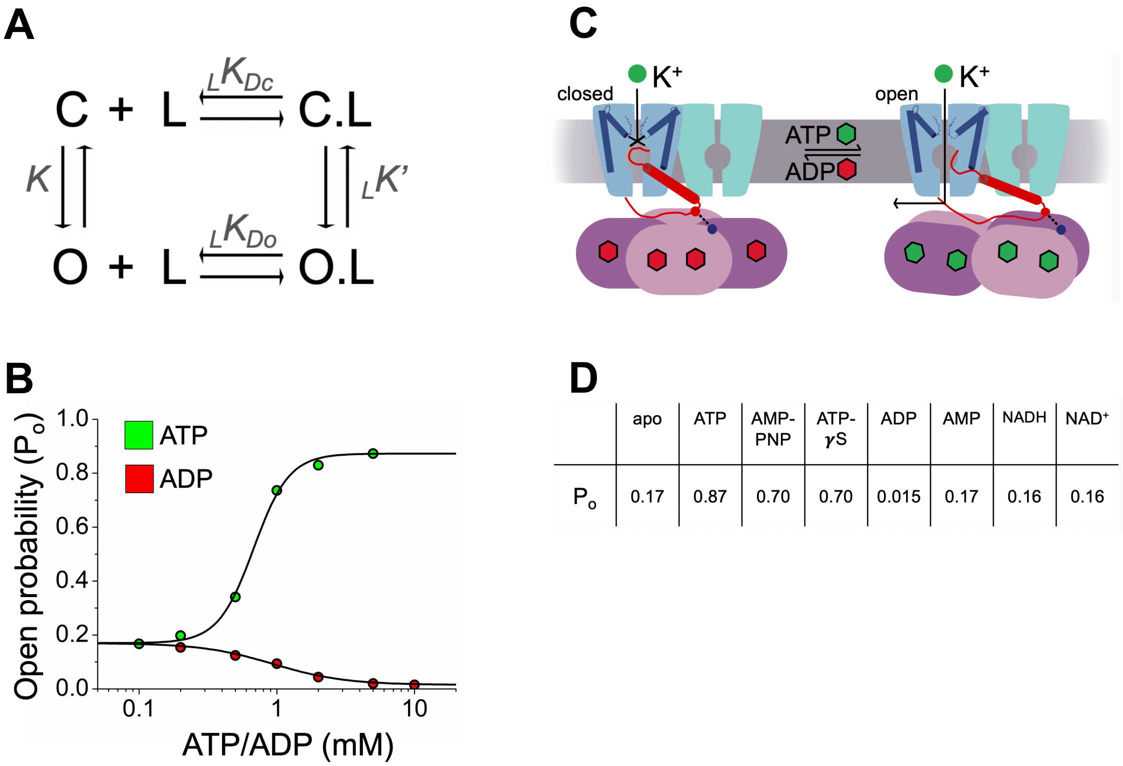

	apo	ATP	AMP-PNP	ATP-γS	ADP	AMP	NADH	NAD⁺
P_o	0.17	0.87	0.70	0.70	0.015	0.17	0.16	0.16

Figure 3. 2 – Effects of ATP, ADP and other ligands on the TrkAH open probability

(A) Simple model for ligand-dependent channel opening, assuming an equilibrium between four species: ligand-free closed or open (C and O) and ligand-bound closed or open (C.L and O.L). **(B)** Single-channel electrophysiology data, reflecting the open probability dependence on [ATP] or [ADP]. Values were obtained by using a ruler to measure heights from a previously published dose-response plot (Cao et al., 2013). **(C)** Schematic diagram, representing the proposed gating mechanism for TrkAH. For clarity, only one of the two D3M2b plunger helices is illustrated (red cylinder). Adapted from Cao et al., 2013. **(D)** Summary of the effect of various ligands on the channel open probability. Values were obtained by using a ruler to measure heights from a previously published bar graph (Cao et al., 2013).

The nonhydrolyzable ATP analogs AMP-PNP and ATP-γS increase the open probability of TrkAH to similar levels as genuine ATP does (Figure 3.2D), consistent with the notion that the energy of ATP binding rather than ATP hydrolysis powers pore opening. A very recent structural update on the TrkAH channel has demonstrated that in contrast to genuine ATP, which favors an open pore, the ATP-γS analog favors a pore conformation that is only partially open (Zhang et al., 2020), suggesting the importance of ATP's terminal phosphate for stabilizing the open relative to the closed ligand-bound channel state; similar logic may apply to the AMP-PNP analog, used in place of ATP in our fluorescence-based experiments. ATP-γS and AMP-PNP both increase the P_o to a maximum of 0.70, about 80% of what is achievable with genuine ATP (Figure 3.2D). Assuming that, under saturating conditions, the number of ligand-free channel species is negligible, the maximum open probability is given by:

$$
{}_{L}P_{o,max} = \frac{[O.L]}{[O.L] + [C.L]}
$$

$$
{}_{L}P_{o,max} = \frac{1}{1 + {}_{L}K'}
$$

3. 2 – Relation between $P_{o,max}$ and the K' equilibrium constant for a particular ligand L

where ${}_{L}K'$ describes the equilibrium between ligand-bound open and closed channel species for a particular ligand *L* (Figure 3.2A). From Equation 3.2 and the known maximum P_o values, we can calculate the ${}_{L}K'$ equilibrium constants for ATP and AMP-PNP to be ${}_{T}K'$ = 0.149 mM and ${}_{M}K'$ = 0.428 mM, respectively. The different efficacy of the two ligands is reflected by the ratio of the two equilibrium constants ${}_{T}K' / {}_{M}K'$ = 0.348. In Section 3.3.2.4 below, we use this ratio to relate our model P_o vs [AMP-PNP] curve to the P_o vs [ATP] dose-response plot observed by electrophysiology (Figure 3.2B). On a per-subunit basis, this ratio translates to:

$$c_L = \sqrt[3.4]{{}_{T}K' / {}_{M}K'}$$

$$c_L = 0.733$$

3. 3 – Experimentally determined numerical value for the scaling factor c_L

The association energy between the TrkA and TrkH modules likely contributes to stabilizing the closed relative to the open pore state, as indicated by the greater TrkH open probability in the absence of the gating ring ($P_o = 0.65$) than in its presence ($P_o = 0.17$). Based on structural findings, a gating mechanism has been proposed for TrkAH, whereby conformational changes in the regulatory module control channel opening by repositioning a plunger-like TrkH component, which consists of the pore-occluding intramembrane loop and the D3M2b helix (Figure 3.2C). In the framework of this model, ADP is thought to stabilize the plunger-in TrkH state, whereas ATP promotes the plunger-out TrkH state, a prediction that has been supported by recent structural findings (Zhang et al., 2020). This qualitative model provides an adequate starting point for understanding the effects of the two ligands on the open probability, but does not quantitatively address the four main features of the ATP- and ADP-dependent P_o dose response curves or the inter-pore coupling phenomena observed in single-channel traces.

A much more detailed mechanistic understanding of the TrkAH channel is afforded by our ability to observe the conformational changes in individual RCK units in TrkA at adequate spatial and temporal resolution (Chapter 2). By knowing the behavior of the observed RCK unit and invoking a quantitative model that properly accounts for the inter-RCK relationships within the regulatory module, one can predict the opening patterns of the associated pore module (Lewis and Lu, 2019b). It is important to keep in mind that, with the exception of one special case, the observed RCK unit does not directly report on the behavior of the remaining RCK units in the gating ring. In the absence of sufficiently high energetic input to stabilize a highly ordered and concerted subunit arrangement, it is much more likely for multi-subunit complexes to adopt configurations, in which certain components of the complex move somewhat independently from the rest.

When deriving a model that explains the ligand dependence of the entire TrkA tetramer through the behavior of individual RCK units, one must carefully weigh two alternative consequences of ligand binding. On the one hand, the effect of ligand binding may be localized to individual RCK units, rendering any ligand-bound unit more likely to adopt a state that promotes a desired channel state. On the other hand, ligand binding may affect the degree of inter-RCK coupling, thus regulating the number and type of possible RCK unit state combinations within the gating ring. Both types of effects were invoked to explain the impact of Ca^{2+} on the open probability of the MthK ion channel (Lewis and Lu, 2019b; Figure 3.3):

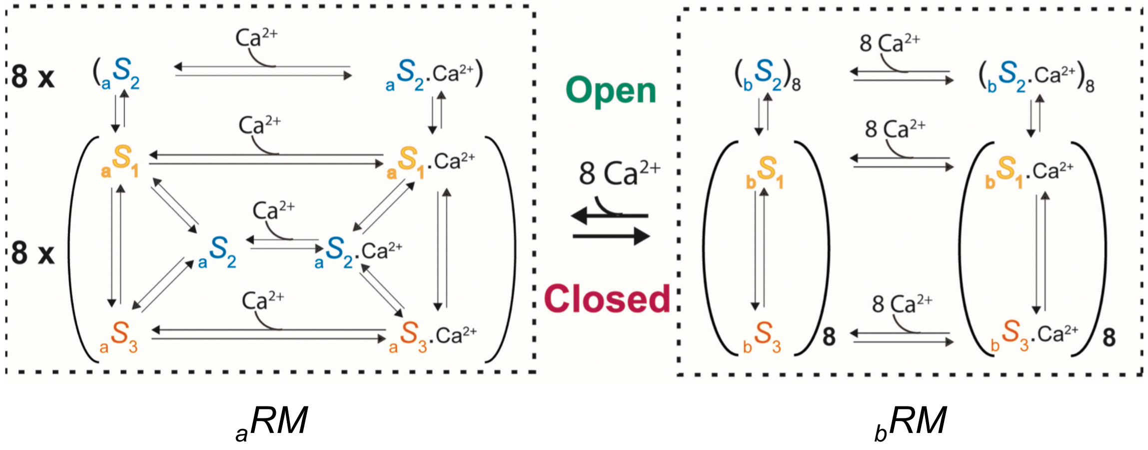

Figure 3. 3 – Model of the MthK regulatory module in two configurations

In this state diagram, regulatory module configurations $_a$RM and $_b$RM are at equilibrium that is under Ca^{2+} control, and the RCK units in each configuration can bind additional Ca^{2+}. In the closed states of $_a$RM, eight RCK units can independently adopt any of the three conformations; in the open states of $_a$RM, all RCKs are in S_2, regardless of whether they are bound to Ca^{2+}. In configuration $_b$RM, S_2 is excluded from the closed channel state.

According to the MthK model, each of the eight RCK units in the gating ring can adopt one of three states, S_1, S_2 and S_3, and channel opening is promoted only by the $(S_2)_8$ subunit combination. In addition, an equilibrium is envisioned between two regulatory module configurations $_a$RM and $_b$RM. In $_a$RM, the RCK units visit each state independently from one another, such that at any given time the gating ring can be in any of the forms $(S_1)_j(S_2)_k(S_3)_{8-j-k}$. Ca^{2+} binding to $_a$RM increases the frequency and duration of instances when each subunit adopts S_2, thus increasing the chance of encountering the $(S_2)_8$ subunit combination that would open the pore. Importantly, Ca^{2+} binding to $_a$RM also provides the necessary energy to transition the entire regulatory module into the more ordered configuration $_b$RM, in which only the $(S_2)_8$ and $(S_1)_j(S_3)_{8-j}$ subunit combinations are energetically accessible. Compared to $_a$RM, $_b$RM has greater odds of adopting the $(S_2)_8$ state, due to the significantly lower number of allowed subunit combinations. A theoretical prediction from the MthK model is that the $_b$RM configuration only becomes energetically available to the MthK gating ring in the whole-channel system and that the isolated regulatory domain can only display the $_a$RM configuration.

A model that takes into account the effect of Ca^{2+} on MthK's individual RCK state probabilities, as well as on inter-subunit coupling, predicts all main features of the previously reported whole-channel P_o vs $[Ca^{2+}]$ dose response curve. Given that TrkA is also composed of RCK units, similar energetic principles of channel gating may apply. ATP or ADP binding to individual TrkA RCK units may alter their inherent state equilibrium and/or affect their coupling to sister or neighbor RCKs.

As discussed in Section 2.4, the state redistribution pattern in the isolated TrkA is nearly identical for the AMP-PNP and ADP ligands, likely because in the absence of the pore module a putative binding site for the ATP γ-phosphate is unavailable. Therefore, single-molecule studies on isolated TrkA may not be as directly informative as those on the isolated MthK gating ring. We deemed it critical to study ligand-induced conformational changes in the Trk regulatory module TrkA docked onto the TrkH pore in order to generate an adequate model for the ATP and ADP effects on the whole channel.

3.2 Methods

3.2.1 Protein purification

3.2.1.1 Affinity purification of TrkH

A modified pET31b expression vector (Novagen), containing the *Vibrio parahaemolyticus trkH* gene, was generously provided by the laboratory of Dr. Ming Zhou, Department of Biochemistry and Molecular Biology, Baylor College of Medicine. The construct, encoding full-length TrkH with a C-terminal decahistidine (His_{10}) tag, cleavable by TEV protease, was transformed into BL21(DE3) bacterial cells; successful transformation and plasmid retention was ensured via kanamycin antibiotic selection. Large suspension cultures were grown in Luria broth supplemented with 25 mg/L kanamycin at 37 ^{o}C and induced at OD_{600nm} = 0.8 with 0.2 mM IPTG for 16-18 h at 20 ^{o}C. Following induction, cells were harvested via centrifugation and cell pellets were snap-frozen in liquid N_2 and stored at -80 ^{o}C for up to 2 years.

For TrkH protein purification, cell pellets were thawed and resuspended in ice-cold base buffer (50 mM Tris-HCl, pH 8.0, 150 mM KCl), supplemented with 1 mM PMSF. The cell suspension was subjected to three rounds of sonication (see Section 2.2.2), followed by a 3-hour room temperature incubation with 40 mM n-decyl-β-D-maltopyranoside (DM) detergent (Anatrace). The cell lysate was cleared via high-speed centrifugation and poured over a column packed with TALON® cobalt affinity resin (Clontech), pre-equilibrated with 5 mM DM in base buffer. The resin with bound TrkH-His_{10} protein was washed with 15 CV of 5 mM DM + 8 mM imidazole (Sigma) in base buffer, and further washed with 20 CV of 1 mM n-dodecyl-β-D-maltopyranoside (DDM) detergent (Anatrace) + 8 mM imidazole in base buffer. Pure TrkH protein was eluted with 4 CV of 1 mM DDM +

200 mM imidazole in base buffer. The elute was concentrated to 100-150 μM using Amicon® Ultra centrifugal filter units with 100 kDa molecular weight cutoff (Millipore Sigma).

3.2.1.2 Affinity purification of TEV protease

BL21(DE3)pLysS cells were transformed with pET plasmid, encoding C-terminally His-tagged TEV protease, fused at the N-terminus with maltose-binding protein (MBP) via a linker containing the TEV recognition sequence ENLYFQGS. Successful transformation and plasmid retention was ensured via ampicillin antibiotic selection. Large suspension cultures were grown in Luria broth supplemented with 100 mg/L ampicillin at 37 °C and induced at OD_{600nm} = 0.6 with 1 mM IPTG for 3 h at 37 °C. Following induction, cells were harvested via centrifugation and cell pellets were snap-frozen in liquid N_2 and stored at -80 °C for 4 months.

Cell pellets with expressed MBP-TEV-His were thawed and resuspended in TEV lysis buffer (20 mM Tris-HCl, pH 8.0, 50 mM NaCl), supplemented with 1 mM PMSF and 6.25 U/mL Pierce® universal nuclease (Thermo Fisher). The cell suspension was subjected to four rounds of sonication (see Section 2.2.2), followed by a 30-min room temperature incubation in the presence of 0.1 mg/mL lysozyme (Sigma) and 0.5% Triton X-100 detergent. The lysate was then centrifuged at high speed and the supernatant was poured over a cobalt affinity column. Resin-bound protein was sequentially washed with TEV wash buffers 1, 2 and 3 (50 mM Tris-HCl, pH 8.0, 500 mM NaCl), containing 0 mM, 4 mM and 8 mM imidazole, respectively. Pure TEV was eluted with TEV elution buffer (50 mM Tris-HCl, pH 8.0, 500 mM NaCl, 200 mM imidazole). The eluted sample was concentrated with 3 kDa cutoff Amicon® ultra centrifugal filter (Millipore Sigma) and dialyzed against TEV recovery wash buffer (20 mM Tris-HCl, pH 8.0, 100 mM NaCl) at 4

°C, overnight, to remove excess imidazole and allow self-cleavage. Next, dialyzed protein was centrifuged at high speed to clear visible precipitates and the supernatant was diluted 5-fold with TEV recovery wash buffer and re-loaded onto the cobalt affinity column to remove free MBP. The resin was washed with 5 CV TEV recovery wash buffer and TEV-His was eluted with 8 CV TEV recovery elution buffer (20 mM Tris-HCl, pH 8.0, 100 mM NaCl, 200 mM imidazole). The cobalt elute was concentrated and dialyzed overnight at 4 °C against TEV storage buffer (25 mM Na^+-phosphate, pH 8.0, 100 mM NaCl, 10% glycerol, 2 mM EDTA, 5 mM DTT). Recovered and buffer-exchanged TEV protease was aliquoted into small 120 μM samples and stored at -20 °C for up to 3 months.

3.2.1.3 Affinity purification of MSP2N2 scaffold protein

His-tagged MSP2N2 protein was expressed recombinantly in BL21(DE3) cells and purified following a previously published protocol (Ritchie et al., 2009). The protein elute, containing 50 mM HEPES, pH 7.8, 100 mM NaCl, 200 mM imidazole, was frozen and stored at -20 °C for 3 months.

3.2.2 TrkA and TrkH in vitro interaction test

TrkA with C-terminal twin-strep-tag, was affinity-purified, as described in Section 2.2.2. TrkH-His_{10} protein was purified separately, as detailed above. Each purified protein was exchanged into TrkAH assembly buffer (20 mM HEPES, pH 7.5, 100 mM KCl, 3.5 mM DM) by means of gel filtration through a Superdex 200 column. 2 μM of TrkH 2-pore module were mixed with 10 μM of TrkA regulatory module and allowed to equilibrate at 4 °C overnight. The TrkA/H mix was then incubated with Strep-Tactin® affinity resin for 1 h at 4 °C, after which the resin was washed extensively with TrkAH assembly buffer. Protein was eluted by incubating the resin with 10 mM d-Desthiobiotin in TrkAH assembly buffer for 15 min at 4 ^{o}C. The elute was allowed to bind to TALON® cobalt affinity resin for 1 h at 4 ^{o}C. The resin was washed extensively with TrkAH assembly buffer and protein was eluted with 1 mM DDM + 200 mM imidazole in base buffer. The protein elute was concentrated with a 10 kDa molecular weight cutoff centrifugal filter and subjected to size exclusion chromatography and SDS-PAGE to evaluate the TrkAH complex formation outcome.

3.2.3 Reconstitution of TrkH into nanodiscs

3.2.3.1 Lipid mix preparation

The following three lipids were mixed in the amounts specified: 100 mg 1-palmitoyl-2-oleoyl-glycero-3-phosphocholine (POPC, Avanti Polar Lipids) + 11 mg 1,2-dioleoyl-sn-glycero-3-phosphoethanolamine-N-(cap biotinyl) sodium salt (18:1 Biotinyl Cap PE, Avanti Polar Lipids) + 8 mg 1-palmitoyl-2-oleoyl-sn-glycero-3-phospho-(1’-rac-glycerol) sodium salt (POPG, Avanti Polar Lipids). After chloroform had been evaporated, the lipid mixture was resuspended in aqueous buffer as previously described (Ritchie et al., 2009); the buffer composition was 20 mM Tris-HCl, pH 8.0, 100 mM NaCl, 100 mM NaCholate. The resulting PC:^{bio}PE:PG lipid stock was aliquoted and stored at -20 ^{o}C until needed for nanodisc assembly.

3.2.3.2 MSP2N2 His-tag removal

Affinity-purified MSP2N2-His protein was thawed from -20 ^{o}C, concentrated and centrifuged at high speed to remove visible precipitates. The His-tag was then cleaved by an overnight incubation of 90 μM MSP2N2-His with 1.6 μM TEV protease, simultaneously dialyzing the protein mixture against 50 mM Tris-HCl, pH 8.0, 0.5 mM EDTA, 1 mM DTT at 4 ^{o}C to potentiate TEV and remove excess imidazole. To prevent cleavage of the TrkH

His-tag at later nanodisc formation steps (see Section 3.2.3.3 below), the TEV protease was irreversibly inhibited by addition of 20 mM iodoacetamide (Sigma), allowing the inhibition reaction to proceed protected from light for 30 min at room temperature. Iodoacetamide was then removed by exchanging the protein sample into base buffer, using a Sephadex™ G-25 M column (GE Healthcare). The recovered sample, containing the tag-less MSP2N2 and inactivated TEV protease, was concentrated to 180 μM and immediately used for TrkH-nanodisc assembly.

3.2.3.3 TrkH-nanodisc assembly, purification and storage

TrkH was purified as described in Section 3.2.1.1 above, and 28.3 μM of the 2-pore module was incubated at 4 °C, overnight with 21.1 mM PC:^{bio}PE:PG lipid mix in the presence of 56.3 mM sodium cholate. The TrkH/lipid mixture was diluted 2.7-fold with MSP2N2 scaffold protein, such that the resulting sample contained 10.4 μM pore module, 7.7 mM PC:^{bio}PE:PG and 114.0 μM MSP2N2. The mixture was rocked at 4 °C for 6.5 h, after which detergent was removed by an overnight incubation with Bio-Beads™ SM-2 adsorbent resin (Bio-Rad). The bio-bead supernatant was recovered and incubated with TALON® cobalt affinity resin for 30 min at room temperature. Next, the cobalt resin was washed extensively with base buffer and TrkH-nanodiscs were eluted with 200 mM imidazole in base buffer. A portion of the cobalt elute was subjected to size exclusion chromatography and SDS-PAGE to evaluate the outcome of TrkH-nanodisc formation. The remaining cobalt elute was snap-frozen in liquid N_2, stored for several weeks at -80 °C and subsequently thawed to test the freeze-thaw tolerance and long-term stability of TrkH-nanodiscs. After the quality of the thawed sample was assessed via gel filtration, the peak fractions were pooled and concentrated with 100 kDa centrifugal filter. Small aliquots of 4.7 μM TrkH-nanodiscs were snap-frozen and stored at -80 °C for several weeks until needed for single-molecule experiments.

3.2.4 Assembly of data collection chamber

Glass slides were assembled and mounted onto the microscope objective as detailed in Section 2.2.4. Each chamber was washed with 6.5 volumes of deionized water, then 6.5 volumes of wash buffer (10 mM HEPES, pH 7.5, 200 mM KCl). 5 mg/mL streptavidin in wash buffer was introduced and allowed to attach to the lysine-coated surface for 15 min. Unbound streptavidin was washed away with 6.5 volumes of wash buffer. Freshly thawed TrkH-nanodiscs diluted to 50 nM were then flowed in and surface attachment was allowed to proceed for 5min, after which unbound nanodiscs were washed away with 6.5 volumes of gel filtration buffer (20 mM Tris-HCl, pH 8.0, 100 mM KCl). To prevent direct attachment of strep-tagged TrkA to the streptavidin-coated surface, the chamber was then perfused with 6.5 volumes of 25 mM d-Desthiobiotin in gel filtration buffer. Next, 3 volumes of 0.5 nM fluorescently labeled TrkA were introduced in the continued presence of 25 mM d-Desthiobiotin for 10 min. Unbound TrkA was cleared by washing with 20 volumes of 25 mM d-Desthiobiotin and 6.5 volumes of gel filtration buffer. Lastly, the chamber was perfused with 4 volumes of activation buffer (20 mM Tris-HCl, pH 7.0, 233 mM K^+, 50 mM $MgCl_2$, 100 mM DTT, 0-50 mM ligand).

3.2.5 Single-molecule measurements and data analysis

Data were collected and analyzed as described in Sections 2.2.5-6.

3.3 Results

3.3.1 Preparation for single-molecule studies on the TrkAH complex

Recombinant wild-type TrkH was successfully purified at a 10 mg/L yield (Figure 3.4). In membrane protein purification strategies that utilize detergent, it is typical for the final product to contain 100-400 kDa of detergent. Indeed, the size exclusion elution profile of purified TrkH displays a predominant peak at 11.7 mL, corresponding to a 290 kDa species, consistent with a 2-pore module (2 x 55.1 kDa) coated with 180 kDa detergent.

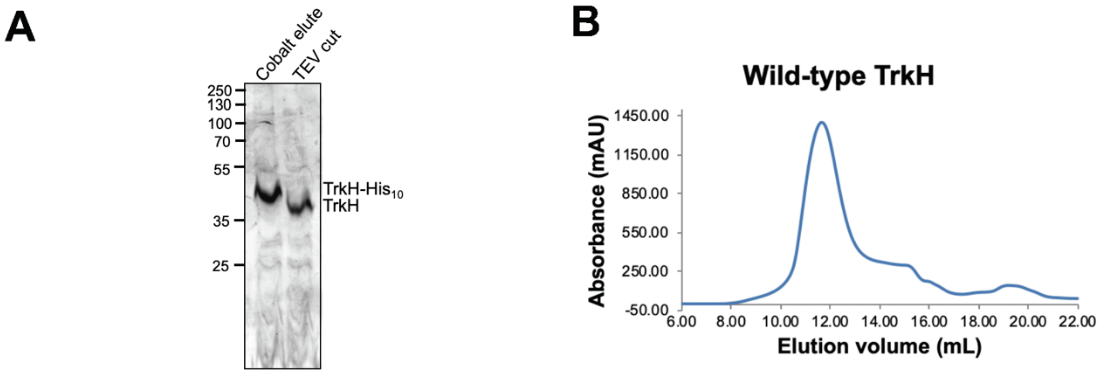

Figure 3. 4 – Purification of the pore module TrkH

(A) SDS-PAGE of affinity-purified wild-type TrkH protein from *V. parahaemolyticus*. **(B)** Superdex 200 size exclusion profile of the TrkH cobalt elute after TEV protease treatment.

For the purpose of studying the regulatory module complexed with the pore, we considered pre-forming the TrkAH complex from its purified components prior to single-molecule data collection (Figure 3.5). To demonstrate the ability of purified TrkA and TrkH to assemble into the TrkAH complex *in vitro*, we mixed the two proteins and employed a double-pull-down strategy to first recover strep-tagged TrkA and then His-tagged TrkH. The final elute contained both proteins (Figure 3.5A), supporting that complex assembly had been successful. The size exclusion profile of the recovered species displays two main peaks at 9.6 mL and 15.1 mL, respectively (Figure 3.5B).

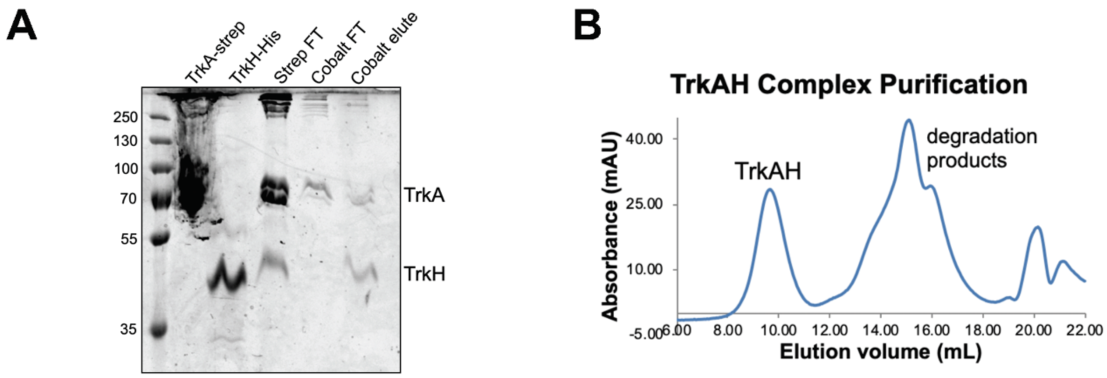

Figure 3. 5 – TrkA and TrkH *in vitro* interaction test

(A) TrkA and TrkH were purified separately and then incubated together to allow complex assembly. TrkAH was recovered from the protein mixture through a double-pull-down strategy, utilizing Strep-Tactin® and TALON® affinity resins. **(B)** Superdex 200 size exclusion profile of the recovered TrkAH complex, displaying two main peaks.

Considering the broadness and low apparent molecular weight of the latter peak (~70 kDa), we suspect that it contains an inhomogeneous mixture of protein degradation species, likely to have arisen from sample aging and the low stability of TrkA in buffers containing the DM detergent. The 9.6 mL elution peak, on the other hand, corresponds to a molecular weight of 670 kDa, which can be accounted for by a TrkA tetramer (4 x 54.4 kDa) assembled with either a single TrkH dimer and 350 kDa detergent or two TrkH dimers and 240 kDa detergent. Since TrkA provides two identical interfaces for pore docking, we cannot rule out the possibility that our *in vitro* TrkAH assembly strategy has resulted in two TrkH dimers attaching to a single gating ring. This version of TrkAH likely also forms when the complex is purified from cells co-expressing the two proteins, as suggested by the previously published crystal structure, in which one two-pore module is attached to either side of TrkA (Cao et al., 2013; PDB 4J9U).

To ensure that our single-molecule studies are performed on the TrkAH complex with physiologically relevant pore and gating ring stoichiometry, we chose to first securely attach the pore module to the glass surface and subsequently add the fluorescently labeled gating ring, thus only favoring the formation of the desired protein complex (Figure 3.6).

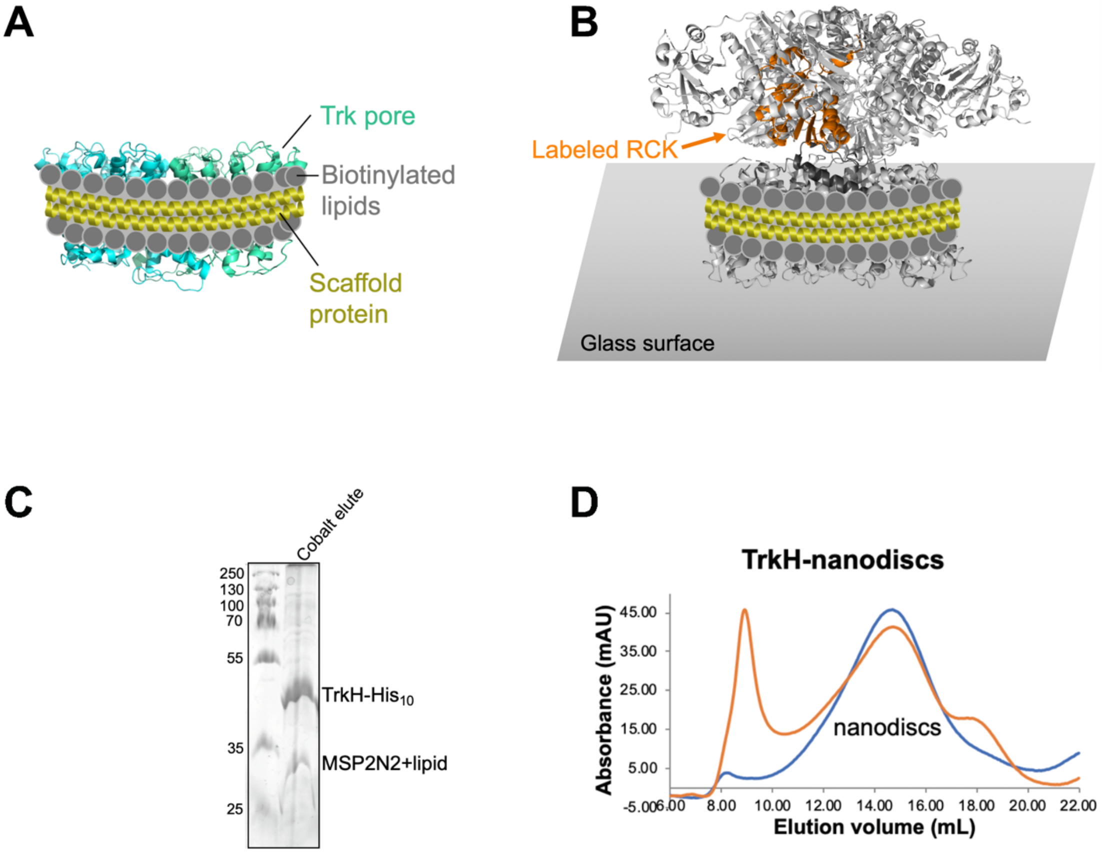

Figure 3. 6 – Assembly and purification of TrkH-nanodiscs

(A) Cartoon representation of TrkH, inserted in a lipid bilayer, held together by a belt of scaffold proteins. **(B)** Biotinylated lipids in the bilayer enable firm attachment on a streptavidin-coated glass coverslip. The fluorescently labeled TrkA gating ring is then added and allowed to dock onto the immobilized pore module. **(C)** SDS-PAGE of affinity-purified TrkH-nanodiscs with a visible band for the MSP2N2 scaffold protein. **(D)** Superose 6 size exclusion profile of affinity-purified TrkH-nanodiscs.

In preparation for this experimental setup, we reconstituted TrkH into nanodiscs, consisting of a lipid bilayer held together by a belt of a scaffold protein derivative of apolipoprotein A-1 (Ritchie et al., 2009; Figure 3.6A). The lipid composition of TrkH-nanodiscs featured the Biotinyl Cap PE lipid species, in which the head group of PE is covalently attached to biotin. Including at least 3 molecules of this phospholipid derivative per bilayer leaflet favors firm and nearly irreversible attachment of TrkH-nanodiscs to the streptavidin-coated glass coverslip. The long-term stability of TrkH-nanodiscs at -80 °C and their resilience against freeze-thawing, made it convenient to pre-form these macromolecular assemblies and store in frozen form until needed for single-molecule experiments.

Since TrkA-strep can attach directly to the streptavidin-coated coverslip instead of interacting with the immobilized pore, we tried excising the twin-strep-tag with TEV and discovered that in the absence of the tag, the TrkA quality rapidly deteriorated. In an alternative approach, we flooded the sample recording chamber with 25 mM d-Desthiobiotin after the pore immobilization step to saturate all unoccupied binding sites on streptavidin. We expected that adding fluorescently labeled TrkA in the continued presence of d-Desthiobiotin would result in few instances of direct TrkA attachment to the glass. In a series of control experiments, we confirmed that when labeled TrkA is added in the presence of 25 mM d-Desthiobiotin and absence of immobilized pore module, only a small handful of rapidly bleaching particles appear in the imaged field (Figure 3.7A). Conversely, when both d-Desthiobiotin and the pore are present, TrkA addition yields a significantly greater number of bright fluorescent particles with a long-lasting emission profile (Figure 3.7C). Note that TrkH itself is prone to some autofluorescence (Figure 3.7B), but we have found that the corresponding signal bleaches rapidly and is qualitatively distinct from the signal emitted by fluorescently labeled TrkA. Together, these control experiments support that TrkA attachment to the glass surface is mediated by TrkH.

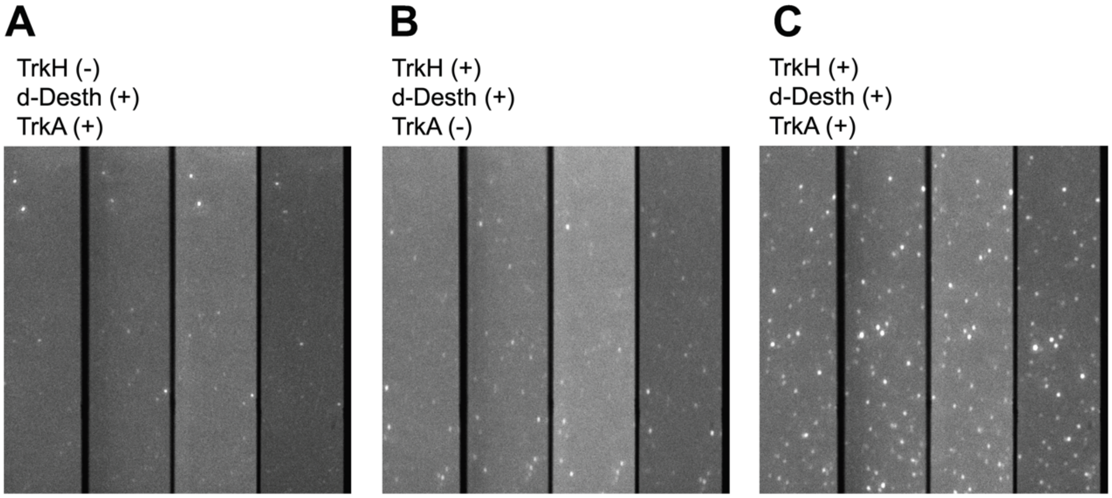

Figure 3. 7 – Control fluorescence-based experiments

(A) Sparse attachment of fluorescently labeled TrkA-strep onto a glass surface, pretreated with d-Desthiobiotin. **(B)** Minor signs of TrkH autofluorescence. **(C)** Robust attachment of BRI$_2$-TrkA-strep onto a TrkH-coated glass surface in the presence of d-Desthiobiotin. The four panels in each image correspond to the four split emission intensity components.

3.3.2 Deducing an energetic model for the TrkAH channel

3.3.2.1 AMP-PNP-dependent conformational changes in individual TrkA subunits

We recorded the polarized emission signals from multiple TrkAH particles at various concentrations of the non-hydrolysable ATP analog AMP-PNP and analyzed the measurements as discussed in Section 2.2.6. After manually filtering out particles with poor angle calculation statistics (high error, insufficient number of events, noisy intensity traces, etc.), we observed two main ligand-sensitive populations that could be adequately separated by imposing an $\Omega = 35^o$ cutoff. Particles in the range $\Omega \leq 35^o$ exhibited extremely shallow AMP-PNP dependence that likely reflects incomplete docking of the labeled gating ring onto the immobilized pore module. The second population of particles ($\Omega \geq 35^o$) had pronounced AMP-PNP dependence with a steep slope, similar to that of the previously published P_o versus [ATP] dose-response plot (Figure 3.2B, Figure 3.8B). All subsequent discussions refer to this latter population of particles.

For each ligand concentration tested, we performed ensemble analysis on the events from individual Ω traces to generate a set of three probability distributions, one for each of the three identified states (Figure 3.8). The plot of each state probability as a function of ligand concentration shows that the populations of S_1 and S_3 decrease with AMP-PNP, whereas the S_2 population increases (Figure 3.8B). The latter observation is consistent with the notion that, similar to MthK, S_2 promotes channel opening.

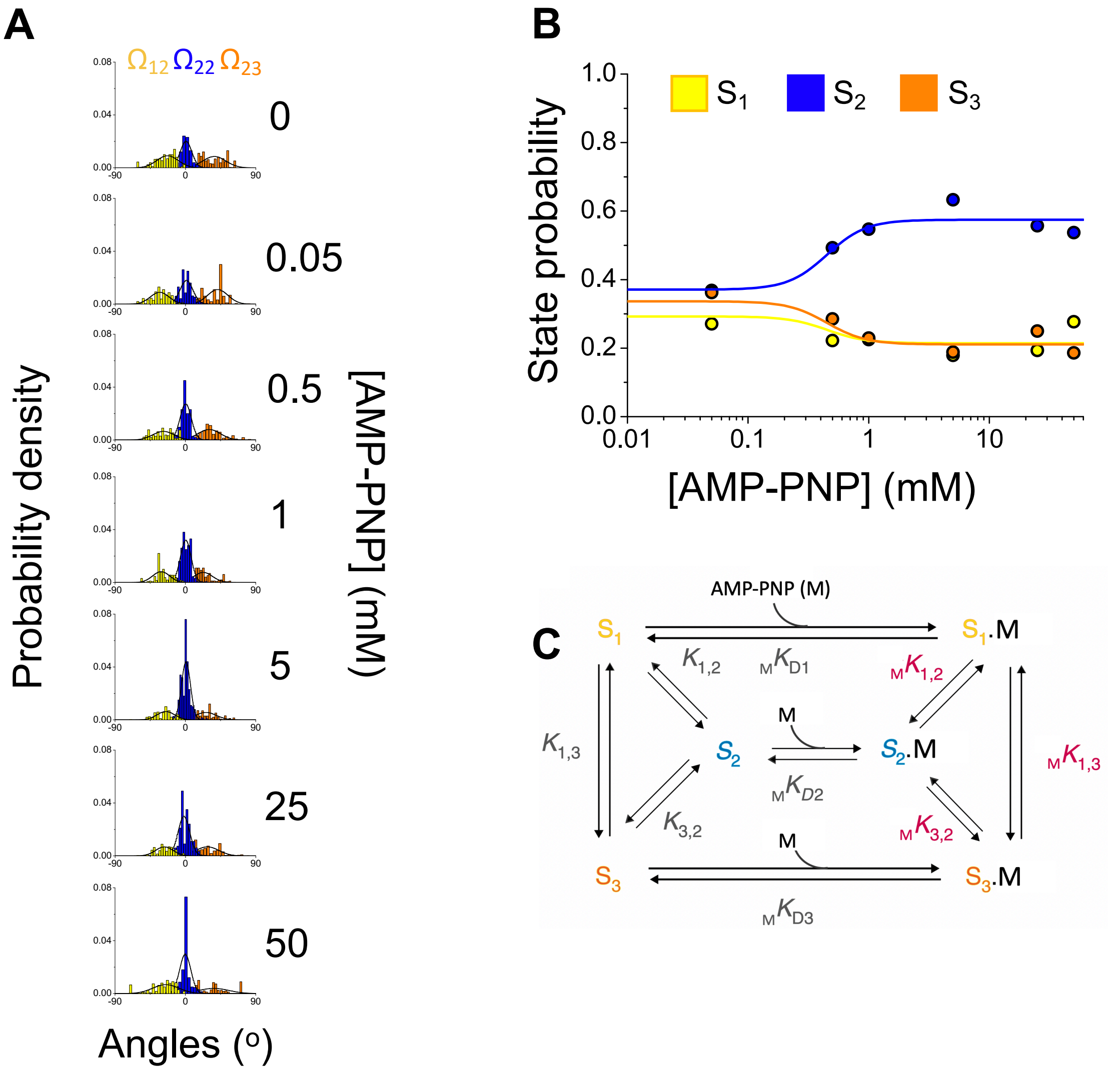

Figure 3. 8 – AMP-PNP dependence of state probabilities

(A) Ω distributions at increasing concentrations of the nonhydrolyzable ATP analog AMP-PNP. Distributions were obtained from a total of 270 particles. The black curves, superimposed on each histogram, are calculated from the data mean and standard deviation values. **(B)** AMP-PNP-dependent probabilities that an observed RCK unit adopts one of the three conformational states. Each circle represents a mean probability value and colored curves were calculated from a global fit of Equation 3.6 to these values. **(C)** A state diagram of an energetic model of RCK. According to this six-state model, the observed RCK unit exists in three conformations, with or without AMP-PNP bound.

Given that the populations of all observed states depend on the AMP-PNP concentration, it is reasonable to assume that, in the presence of the ligand, each observed state exists as a mixture of a ligand-free (S_1, S_2, S_3) and a ligand-bound form ($S_1.M_n$, $S_2.M_n$, $S_3.M_n$; Figure 3.8C), where *n* is the number of ligand molecules bound per subunit:

$$[{}^{obs}S_i] = [S_i] + [S_i.M_n]$$

$$i = 1, 2, 3$$

Choosing S_2 as a reference state, we can define the following equilibrium constants:

$$K_{i,2} = \frac{[S_i]}{[S_2]}$$

$${}_{M}K_{i,2} = \frac{[S_i.M_n]}{[S_2.M_n]}$$

$$({}_{M}K_{Di})^n = \frac{[S_i][M]^n}{[S_i.M_n]}$$

3. 4

The above expressions allow us to relate the concentration of each individual state to the concentration of the unbound S_2 species:

$$[S_i] = [S_2]K_{i,2}$$

$$[S_i.M_n] = [S_2.M_n]\ {}_{M}K_{i,2} = [S_2][M]^n \frac{{}_{M}K_{i,2}}{({}_{M}K_{D2})^n}$$

$$[{}^{obs}S_i] = [S_i] + [S_i . M_n]$$

$$[{}^{obs}S_i] = [S_2]\left(K_{i,2} + {}_{M}K_{i,2}\left(\frac{[M]}{{}_{M}K_{D2}}\right)^n\right)$$

3. 5

With these relationships we can express the probability of observing a particular state as a function of five equilibrium constants and the ligand concentration:

$$P_i = \frac{[S_i] + [S_i . M_n]}{[S_1] + [S_2] + [S_3] + [S_1 . M_n] + [S_2 . M_n] + [S_3 . M_n]}$$

$$P_i = \frac{K_{i,2} + \ {}_{M}K_{i,2}\left(\frac{[M]}{{}_{M}K_{D2}}\right)^n}{\left(K_{1,2} + 1 + K_{3,2}\right) + \left(\frac{[M]}{{}_{M}K_{D2}}\right)^n\left({}_{M}K_{1,2} + 1 + \ {}_{M}K_{3,2}\right)}$$

3. 6 – Model for RCK state probability dependence on ligand concentration

Note that Equation 3.6 above also describes the RCK state probability dependence on the concentration of genuine ATP, except that the numerical values of at least some of the equilibrium constants would be different if the channel were activated with ATP instead of AMP-PNP. We globally fit Equation 3.6 to the three RCK state probability plots in Figure 3.8B, and obtained values for all equilibrium constants summarized in Table 3.1 below:

Table 3. 1 – Fitted parameters of Equation 3.6 and subunit state probabilities at min and max AMP-PNP

Equilibrium Constants at Zero AMP-PNP		Observed Probabilities at Zero AMP-PNP	
$K_{1,2}$	0.777 +0.098/-0.061[b]	$_{apo}P_1$	0.313 ± 2.33E-2[a]
$K_{3,2}$	0.940 +0.135/-0.239[b]	$_{apo}P_2$	0.372 ± 2.43E-2[a]
$K_{1,3}$	0.826 +0.158/-0.220[b]	$_{apo}P_3$	0.315 ± 2.34E-2[a]
Equilibrium Constants at Saturating AMP-PNP		**Observed Probabilities at 25 mM AMP-PNP**	
$_{M}K_{1,2}$	0.363 +0.089/-0.043[b]	$_{M}P_1$	0.193 ± 2.35E-2[a]
$_{M}K_{3,2}$	0.368 +0.084/-0.055[b]	$_{M}P_2$	0.557 ± 2.96E-2[a]
$_{M}K_{1,3}$	0.986 +0.330/-0.188[b]	$_{M}P_3$	0.250 ± 2.58E-2[a]
$_{M}K_{D}$ (mM)			
$_{M}K_{D1}$	0.800 +0.281/-0.692[b]		
$_{M}K_{D2}$	0.374 +0.081/-0.319[b]		
$_{M}K_{D3}$	0.955 +0.330/-0.862[b]		
Exponent of [AMP-PNP]			
n	2.442 +14.970/-0.661[b]		

[a] Probabilities calculated from the number of observed events per state, relative to the total. Standard errors calculated based on variance in measurements from multinomial distribution.

[b] 95% confidence intervals from Chi Squared optimization

For the purposes of model derivation, we have made two key assumptions. First, since the S_2 population rises with increasing [AMP-PNP], we have assumed that, as in the MthK system, pore opening is promoted by the all-S_2 RCK unit combination in TrkA. Secondly, we have assumed that in presence of the pore module, RCK units are coupled in pairs, without specifying if the participants in a pair are sister or neighbor RCKs. Thus, in all model derivations, we will consider TrkA as a tetramer of RCK dimers rather than an octamer of RCK units, and will make no assumptions about the structural identity of the dimeric RCK species involved.

Most of the main features of the P_o vs [ATP] dose response curve in Figure 3.2B are mirrored by our P_2 vs [AMP-PNP] plot in Figure 3.8B. The two graphs have comparable EC50 values and Hill coefficients ($n = 3.4$ from electrophysiology versus $n = 2.4$ from fluorescence polarization studies). In addition, the observed P_2 at saturating ligand concentration (${}_{M}P_2 = 0.56$) approximates the maximum P_o achieved with AMP-PNP (${}_{M}P_{o,max} = 0.70$). The obvious discrepancy between the minimum probability value ${}_{apo}P_2 = 0.37$ and the spontaneous open probability ${}_{apo}P_o = 0.17$ implies that in the absence of ligand, the observed RCK dimer is not fully coupled to the remaining RCK dimers in the regulatory module, so observing one dimer in S_2 is not equivalent to observing the $(S_2)_4$ gating ring conformation. Instead, the ${}_{apo}P_o$ value is closely approximated by ${}_{apo}P_2^2 = 0.1369$, suggesting that two independent events must occur simultaneously at the gating ring level in order to open the pore. The latter observation is consistent with a gating ring composition featuring two independent ring halves, each containing two coupled RCK dimers. Our findings thus point to a model that assumes an equilibrium between two gating ring configurations, a semi-concerted ${}_{apo}RM$ and a fully concerted ${}_{T}RM$, with ATP promoting transition to the latter configuration. Note that the offset between ${}_{apo}P_2^2$ and ${}_{apo}P_o$ is identical to the offset between ${}_{M}P_2$ and ${}_{M}P_{o,max}$ (0.1369/0.17 = 0.8 and 0.557/0.70 = 0.8). As discussed later, this offset may be due to differences in experimental conditions between the fluorescence- and electrophysiology-based studies.

3.3.2.2 ADP-dependent conformational changes in individual TrkA subunits

In the presence of the pore module, saturating ADP did not alter the state equilibrium of individual subunits (Figure 3.9A; Table 3.2). Since in the isolated gating ring the populations of all three states responded to this ligand (see Section 2.3.8, Figure 2.13C), the purified TrkAH complex should remain sensitive to ADP.

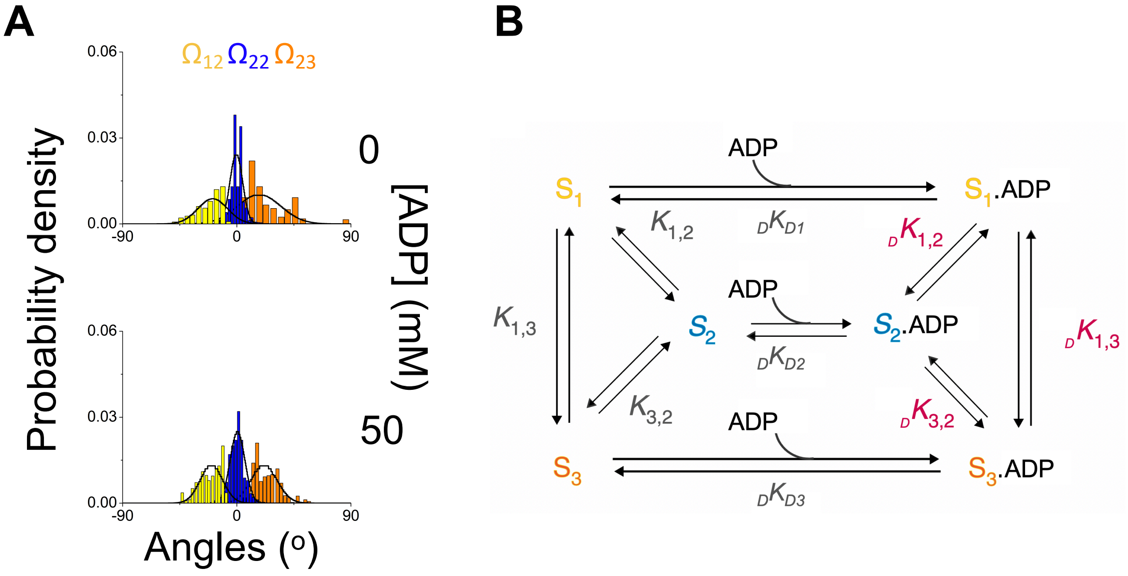

Figure 3. 9 – ADP dependence of RCK state probabilities

(A) Ω distributions at 0 and 50mM ADP. Distributions were obtained from a total of 140 particles. The black curves, superimposed on each histogram, are calculated from the data mean and standard deviation values. **(B)** A six-state energetic model for an individual RCK unit.

Assuming that TrkA retains its ability to bind ADP in the presence of TrkH (Figure 3.9B), the lack of ADP effect on the observed state probabilities must be interpreted as functionally meaningful.

Table 3. 2 – Calculated equilibrium constants and subunit state probabilities at min and max ADP

Equilibrium Constants at Zero ADP		Observed Probabilities at Zero ADP	
$K_{1,2}$	$0.841 \pm 7.10E\text{-}2^{b}$	$_{apo}P_{1}$	$0.313 \pm 2.33E\text{-}2^{a}$
$K_{3,2}$	$0.847 \pm 8.38E\text{-}2^{b}$	$_{apo}P_{2}$	$0.372 \pm 2.43E\text{-}2^{a}$
$K_{1,3}$	$0.994 \pm 1.04E\text{-}1^{b}$	$_{apo}P_{3}$	$0.315 \pm 2.34E\text{-}2^{a}$
Equilibrium Constants at Saturating ADP		**Observed Probabilities at 50 mM ADP**	
$_{D}K_{1,2}$	$0.818 \pm 5.02E\text{-}2^{b}$	$_{D}P_{1}$	$0.296 \pm 1.38E\text{-}2^{a}$
$_{D}K_{3,2}$	$0.945 \pm 5.49E\text{-}2^{b}$	$_{D}P_{2}$	$0.362 \pm 1.45E\text{-}2^{a}$
$_{D}K_{1,3}$	$0.865 \pm 5.44E\text{-}2^{b}$	$_{D}P_{3}$	$0.342 \pm 1.44E\text{-}2^{a}$

[a] Probabilities calculated from the number of observed events per state, relative to the total. Standard errors calculated based on variance in measurements from multinomial distribution.

[b] Equilibrium constants calculated from the relationships: $K_{i,j} = P_i / P_j$ and $_{D}K_{i,j} = {}_{D}P_i / {}_{D}P_j$. Standard errors calculated by error propagation from the probability errors.

In order to reduce the probability of the $(S_2)_4$ conformation without reducing the P_2 value, ADP must increase the number of possible combinatorial species by loosening the inter-dimer coupling that exists in the apo state. Indeed, the value of $_{D}P_2^{4} = 0.017$ closely approximates the measured $_{D}P_{o,min} = 0.015$, consistent with the need for four independent events to occur simultaneously at the gating ring level in order to open the pore module. Hence, we can expand our model and envision a third configuration of the gating ring, promoted by ADP ($_{D}$RM), in which the four RCK dimers can visit each of the three states S_1, S_2 and S_3 independently from one another (Figure 3.10):

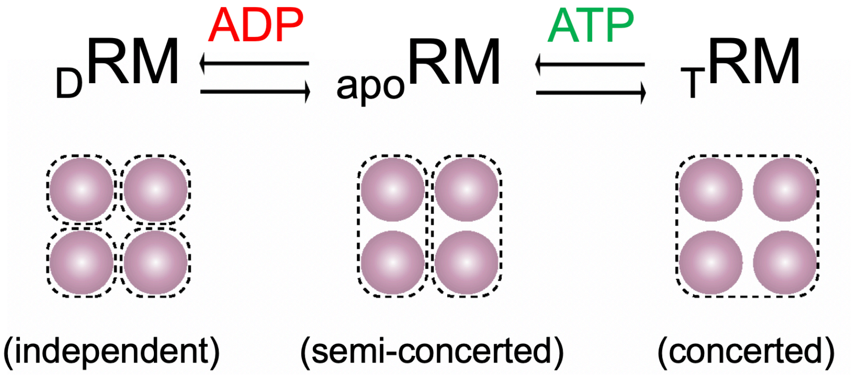

Figure 3. 10 – Proposed effects of ATP and ADP on TrkA's inter-subunit coupling

Each violet circle represents a dimer of RCK units. In the absence of ligand, the regulatory module is in the $_{apo}$RM configuration with two independent structural components, each composed of two coupled RCK dimers. ATP promotes further coupling, yielding the $_{T}$RM configuration in which all RCK dimers transition concertedly between S_2 and combinations of S_1 and S_3. ADP uncouples the dimers in each $_{apo}$RM ring half, thus promoting the $_{D}$RM configuration of four independent RCK dimers.

Bear in mind that, in principle, models other than the one summarized in Figure 3.10 can be invoked to reconcile our fluorescence polarization data with previously reported electrophysiology measurements. For the purposes of all subsequent derivations, we will assume the model in Figure 3.10. We will further assume that, like in the MthK regulatory module, "coupled" components are allowed to either all be in S_2 or any combination of S_1 and S_3. We define a "tetramer" as a pair of coupled RCK dimers and an octamer as a pair of coupled RCK tetramers. Hence, depending on the level of inter-RCK coupling, the Trk gating ring can be thought of as a tetramer of independent dimers, a dimer of independent tetramers, or a single concerted octameric species.

3.3.2.3 Analytic solution for the TrkAH open probability in the absence of ligand

As explained in Section 3.3.2.1 above, we have concluded that in the absence of ligand, TrkA is in a semi-concerted state, whereby the two RCK dimers in each ring half are coupled, but the two ring halves are independent, i.e. a dimer of independent tetramers. In this configuration, three general regulatory module types are present: $({}_{apo}S_{1,3})({}_{apo}S_{1,3})$, $({}_{apo}S_{1,3})({}_{apo}S_2)$ and $({}_{apo}S_2)_2$, with only the $({}_{apo}S_2)_2$ combination promoting channel opening. The concentration of the open regulatory module species is given by:

$$\left[{}_{apo}RM_o\right] = \left[\left({}_{apo}S_2\right)_2\right] = {}_{a1}K\left[{}_{apo}S_2\right]^2$$

3. 7

with ${}_{a1}K$ representing the association constant between ring halves. The total regulatory module concentration is given by:

$$\left[{}_{apo}RM\right] = \left[\left({}_{apo}S_{1,3}\right)\left({}_{apo}S_{1,3}\right)\right] + 2\left[\left({}_{apo}S_{1,3}\right)\left({}_{apo}S_2\right)\right] + \left[\left({}_{apo}S_2\right)_2\right]$$

$$\left[{}_{apo}RM\right] = {}_{a1}K\left[{}_{apo}S_{1,3}\right]^2 + 2{}_{a1}K\left[{}_{apo}S_{1,3}\right]\left[{}_{apo}S_2\right] + {}_{a1}K\left[{}_{apo}S_2\right]^2$$

$$\left[{}_{apo}RM\right] = {}_{a1}K\left(\left[{}_{apo}S_1\right] + \left[{}_{apo}S_2\right] + \left[{}_{apo}S_3\right]\right)^2$$

3. 8

where we have taken into account that each of the subunit combination $(S_{1,3})(S_2)$ can arise from two distinct permutations. Thus, in the absence of ligand, the TrkAH open probability is:

$${}_{apo}P_o = \frac{\left[{}_{apo}RM_o\right]}{\left[{}_{apo}RM\right]} = \frac{\left[{}_{apo}S_2\right]^2}{\left(\left[{}_{apo}S_1\right] + \left[{}_{apo}S_2\right] + \left[{}_{apo}S_3\right]\right)^2}$$

$${}_{apo}P_o = \frac{1}{\left(K_{1,2} + 1 + K_{3,2}\right)^2}$$

3. 9 – Model-derived open probability expression for the ligand-free TrkAH channel

Substituting our experimentally determined values for $K_{1,2}$ and $K_{3,2}$ (Table 3.1) into the equation above, predicts ${}_{apo}P_o = 0.14$, closely approximating the previously measured ${}_{apo}P_o = 0.17$ for the apo state of the channel.

3.3.2.4 Analytic solution for the TrkAH open probability dependence on [AMP-PNP]

In the derivations below, we will assume that, at saturating ligand concentration, the number of unbound RCK units is negligible, i.e. $[{}^{obs}S_i] \approx [S_i.L_n] = [{}_LS_i]$. As suggested by our initial findings, binding to AMP-PNP (or ATP) increases the TrkAH open probability by enhancing inter-RCK coupling in TrkA, such that the entire gating ring can be thought of as a single concerted species that exists in either an open state S_2 or a closed state $S_{1,3}$. The concentrations of the open and closed regulatory module species can be expressed in terms of the experimentally observed subunit concentrations at saturating AMP-PNP as follows:

$$[{}_MRM_o] = [{}_MS_2]$$

$$[{}_MRM_c] = [{}_MS_1] + [{}_MS_3]$$

3. 10

The total concentration of the regulatory module is:

$$[{}_MRM] = [{}_MS_1] + [{}_MS_2] + [{}_MS_3]$$

3. 11

Therefore, the TrkAH open probability at maximum AMP-PNP is:

$${}_MP_{o,max} = \frac{[{}_MRM_o]}{[{}_MRM]} = \frac{[{}_MS_2]}{[{}_MS_1] + [{}_MS_2] + [{}_MS_3]}$$

$$_{M}P_{o,max} = \frac{1}{_{M}K_{1,2} + 1 + {_{M}K_{3,2}}}$$

3. 12 – Model-derived maximum P$_o$ expression for the AMP-PNP-bound TrkAH channel

Evaluating the expression above using the experimentally determined parameters $_{M}K_{1,2}$ and $_{M}K_{3,2}$ at a saturating concentration of AMP-PNP (Table 3.1), we predict a maximum TrkAH open probability $_{M}P_o = 0.57$, comparable to the previously measured $_{M}P_{o,max} = 0.70$ with the same ligand (Cao et al., 2013).

At intermediate AMP-PNP concentrations, the regulatory module population will be a mixture of the $_{apo}$RM and $_{M}$RM configurations described above, so the general expression for the TrkAH open probability in response to AMP-PNP is given by:

$$_{M}P_o = \frac{[_{apo}RM_o] + [_{M}RM_o]}{[_{apo}RM_o] + [_{M}RM_o] + [_{apo}RM_c] + [_{M}RM_c]}$$

$$_{M}P_o = \frac{1 + \left(\frac{[M]}{_{M}K_{D2}}\right)^n}{1 + \left(\frac{[M]}{_{M}K_{D2}}\right)^n + (K_{1,2} + K_{3,2})(K_{1,2} + 2 + K_{3,2}) + ({_{M}K_{1,2}} + {_{M}K_{3,2}})\left(\frac{[M]}{_{M}K_{D2}}\right)^n}$$

3. 13 – Whole-channel energetic model for ligand-induced activation of TrkAH

where we have expressed the concentrations of AMP-PNP-bound states in terms of the concentration of $_{apo}S_2$ by utilizing the relationship:

$$[_{M}S_2] = [_{apo}S_2]^2 \left(\frac{[M]}{_{M}K_{D2}}\right)^n$$

3. 14

Equation 3.13 above describes the activation energetics of TrkAH with not only AMP-PNP, but also genuine ATP, as long as the appropriate ligand-specific numerical values are assigned to the equilibrium constants. Substituting the equilibrium constants from the subunit model fit (Table 3.1) into Equation 3.13, we calculated the model-based P_o vs [AMP-PNP] curve illustrated in Figure 3.11A. Despite underestimating the experimentally observed ${}_{apo}P_o$ and ${}_{T}P_{o,max}$, our model produces a curve, whose slope and EC50 values are comparable to those from the experimental graph (Table 3.3).

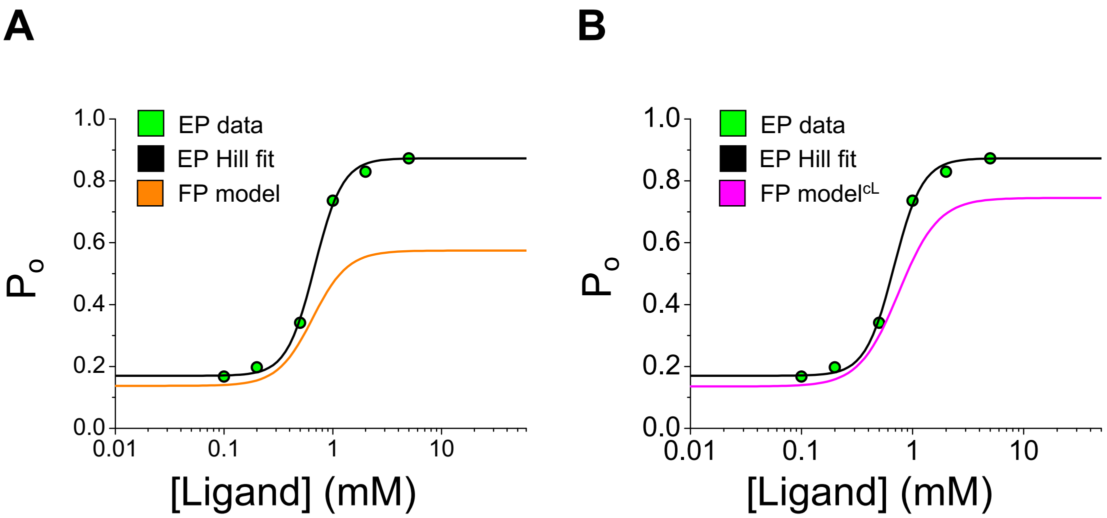

Figure 3. 11 – Comparison between observed and modeled TrkAH P_o dependence on [ATP] and [AMP-PNP]

Experimentally observed P_o vs [ATP] dose response (green circles; Cao et al., 2013), fit with the Hill equation (black trace), and plotted against: **(A)** a P_o vs [AMP-PNP] model curve, calculated from Equation 3.13 or **(B)** a P_o vs [AMP-PNP] model curve scaled by the c_L factor according to Equation 3.15. EP = electrophysiology, FP = fluorescence polarization.

Table 3. 3 – Hill fit parameter summary

	$_{apo}P_o$	$_{L}P_{o,\,max}$	n	EC50 (mM)
Data Hill fit[a]	0.17	0.86	3.4	0.68
Hill fit to Model$_{\text{Eqn.3.13}}$[b]	0.13	0.57	2.7	0.62
Hill fit to Model$_{\text{Eqn.3.16}}$[c]	0.17	0.86	3.4	0.67

[a] Values generated from the fit of Eqn. 3.1 to electrophysiology data

[b] Values generated from the fit of Eqn. 3.1 to a dataset, simulated from Eqn. 3.13

[c] Values generated from the fit of Eqn. 3.1 to a dataset, simulated from Eqn. 3.16

As mentioned in Section 3.1.2, ATP stabilizes the O.L channel state more efficiently than AMP-PNP does, and this difference in ligand efficacy is reflected by the equilibrium constant ratio c_L (see Equation 3.3). It would have been more informative to compare our model curve to an experimentally derived P_o versus [AMP-PNP] dose-response plot, which is unfortunately unavailable. Alternatively, we can utilize the c_L ratio as a scaling factor that can be incorporated into Equation 3.13 to account for the difference in ligands:

$$_{T}P_o = \frac{1 + \left(\frac{[M]}{_{M}K_{D2}}\right)^n}{1 + \left(\frac{[M]}{_{M}K_{D2}}\right)^n + \left(K_{1,2} + K_{3,2}\right)\left(K_{1,2} + 2 + K_{3,2}\right) + \left(c_L^n\,{}_{M}K_{1,2} + c_L^n\,{}_{M}K_{3,2}\right)\left(\frac{[M]}{_{M}K_{D2}}\right)^n}$$

3. 15 – Energetic model for AMP-PNP-induced activation of TrkAH, scaled by c_L

From Equation 3.15 above we calculated the magenta P_o curve in Figure 3.11B, using the experimentally determined numerical value for $c_L = 0.733$ (see Equation 3.3). This scaled trace reflects what the P_o ligand dependence calculated from our model would have looked like, were we to use genuine ATP instead of AMP-PNP.

After implementing the c_L scaling factor, any remaining discrepancies between the observed and model P_o dose responses reflect the random and systematic errors associated with each type of experiment. So far, we have not accounted for two notable distinctions between the fluorescence- and electrophysiology-based experiments: (1) unlike our single-molecule measurements, the single-channel recordings were likely obtained at nonzero membrane potential ($V_m \neq 0$); and (2) we used highly pure TrkAH, reconstituted in nanodiscs, containing the PC:^{bio}PE:PG lipid mix in proportions described in Section 3.2.3.1, while single-channel data were obtained from *E. coli* giant spheroplasts with lipid composition ~75% PE, ~20% PG and ~5% cardiolipin (CL) (Rowlett et al., 2017). In order to estimate the combined random and systematic errors for the two types of experiments, we introduce two additional scaling factors c_{Ea} and c_{EI}, whose proper placement in Equation 3.15 above yields a scaled trace (Figure 3.12A) that closely matches the observed P_o vs [ATP] dose response:

$$_TP_o = \frac{1 + \left(\frac{[M]}{_MK_{D2}}\right)^n}{1 + \left(\frac{[M]}{_MK_{D2}}\right)^n + c_{Ea}^2\left(K_{1,2} + K_{3,2}\right)\left(K_{1,2} + 2 + K_{3,2}\right) + c_{Ea}^2 c_{El}^n c_L^n\left(_MK_{1,2} + {_MK_{3,2}}\right)\left(\frac{[M]}{_MK_{D2}}\right)^n}$$

3. 16 – Energetic model for AMP-PNP-induced activation of TrkAH, scaled by c_L, c_{Ea} and c_{EI}

Using the relationships below, the value of c_{Ea} can be approximated from the differences between the observed and modeled $_{apo}P_o$ values in Figure 3.11B:

$$K_{1,2} + K_{3,2} = \sqrt{\frac{1}{{}_{apo}P_o}} - 1$$

$$^{EP}K_{1,2} + {}^{EP}K_{3,2} = \sqrt{\frac{1}{{}^{EP}_{apo}P_o}} - 1 = \sqrt{\frac{1}{0.17}} - 1 = 1.425$$

$$^{FP}K_{1,2} + {}^{FP}K_{3,2} = \sqrt{\frac{1}{{}^{FP}_{apo}P_o}} - 1 = \sqrt{\frac{1}{0.135}} - 1 = 1.722$$

$$c_{Ea} = \frac{{}^{EP}K_{1,2} + {}^{EP}K_{3,2}}{{}^{FP}K_{1,2} + {}^{FP}K_{3,2}} = \frac{1.425}{1.722}$$

$$c_{Ea} = 0.828$$

3. 17 – Numerical approximation of the scaling factor c_{Ea}

In the above expressions, the “EP” and “FP” superscripts are used to distinguish parameters that correspond to the electrophysiology experiment from parameters that correspond to the fluorescence polarization experiment, respectively. The effect of applying the c_{Ea} scaling factor alone to the model plot in Figure 3.11B would be to vertically translate the entire magenta curve and match the experimental and model ${}_{apo}P_o$ values. After performing this operation, the remaining gap between the two graphs on the ligand-bound side can be closed by implementing the c_{El} scaling factor, calculated as follows:

$${}_{L}K_{1,2} + {}_{L}K_{3,2} = \frac{1}{{}_{L}P_{o,max}} - 1$$

$$^{EP}_{T}K_{1,2} + {}^{EP}_{T}K_{3,2} = \frac{1}{{}^{EP}_{T}P_{o,max}} - 1 = \frac{1}{0.87} - 1 = 0.149$$

$${}^{FP}_{T}K^{*}_{1,2} + {}^{FP}_{T}K^{*}_{3,2} = \frac{1}{{}^{FP}_{T}P^{*}_{o,max}} - 1 = \frac{1}{0.78} - 1 = 0.282$$

$$c_{El} = \sqrt[3.4]{\frac{{}^{EP}_{T}K_{1,2} + {}^{EP}_{T}K_{3,2}}{{}^{FP}_{T}K^{*}_{1,2} + {}^{FP}_{T}K^{*}_{3,2}}} = \sqrt[3.4]{\frac{0.149}{0.282}}$$

$$c_{El} = 0.829$$

3. 18 – Numerical approximation of the scaling factor c_{El}

where asterisks are used to emphasize that the values in question correspond to the magenta plot after it has already been scaled and vertically translated by the c_{Ea} factor. Re-calculating the model trace using Equation 3.16 and the numerical estimates for c_{Ea} and c_{El} above, yields the blue model curve in Figure 3.12A:

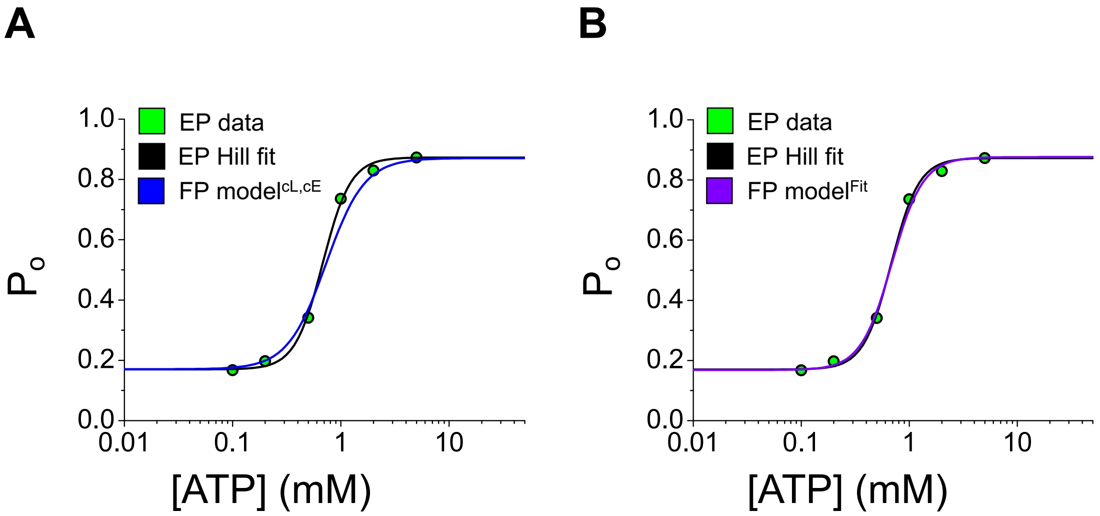

Figure 3. 12 – Estimation of systematic and random errors in EP and FP experiments

Experimentally observed P_o vs [ATP] dose response (green circles; Cao et al., 2013), fit with the Hill equation (black trace), and plotted against: **(A)** a P_o vs [ATP] model curve, calculated from Equation 3.16 or **(B)** a P_o vs [ATP] model curve, generated through the simultaneous fit of Equation 3.6 to the RCK state probability data and Equation 3.16 to the electrophysiological data. EP = electrophysiology, FP = fluorescence polarization.

To obtain a better estimate for the error, we performed a simultaneous fit of Equation 3.6 to the RCK state probability data (Figure 3.8B), and Equation 3.16 to the electrophysiological data, where common parameters were shared and the c_L value was fixed at 0.733; this global fit generated the purple curve in Figure 3.12B. All fitted parameter values, except for c_{Ea} and c_{El}, are summarized in Table 3.4 below, alongside the corresponding values from Table 3.1. The optimized values for the error parameters were c_{Ea} = 0.839+0.054/-0.093 and c_{El} = 0.917+0.177/-0.166. These errors correspond to reasonably small energetic fluctuations on the order of 0.1 to 0.2kT, to be expected, given that our fluorescence polarization measurements detect conformational changes in single subunits, whose states are separated by ~1kT. One possible mechanistic interpretation of the three scaling factors c_L, c_{Ea} and c_{El} is provided in Section 3.4.2.

Table 3. 4 – Fitted parameters of subunit model alone versus both subunit and channel models together and subunit state probabilities at min and max AMP-PNP

	Equilibrium Constants at Zero AMP-PNP			Observed Probabilities at Zero AMP-PNP
	Fit: Subunit[c]	Fit: Subunit and Channel[d]		Observed
$K_{1,2}$	0.777 +0.098/-0.061[b]	0.770 +0.142/-0.062[b]	${}_{apo}P_{1}$	0.313 ± 2.33E-2[a]
$K_{3,2}$	0.940 +0.135/-0.239[b]	0.941 +0.084/-0.142[b]	${}_{apo}P_{2}$	0.372 ± 2.43E-2[a]
$K_{1,3}$	0.826 +0.158/-0.220[b]	0.818 +0.168/-0.140[b]	${}_{apo}P_{3}$	0.315 ± 2.34E-2[a]
	Equilibrium Constants at Saturating AMP-PNP			**Observed Probabilities at 25 mM AMP-PNP**
	Fit: Subunit[c]	Fit: Subunit and Channel[d]		Observed
${}_{M}K_{1,2}$	0.363 +0.089/-0.043[b]	0.377 +0.061/-0.048[b]	${}_{M}P_{1}$	0.193 ± 2.35E-2[a]
${}_{M}K_{3,2}$	0.368 +0.084/-0.055[b]	0.377 +0.085/-0.037[b]	${}_{M}P_{2}$	0.557 ± 2.96E-2[a]
${}_{M}K_{1,3}$	0.986 +0.330/-0.188[b]	1.000 +0.278/-0.161[b]	${}_{M}P_{3}$	0.250 ± 2.58E-2[a]
	${}_{M}K_{D}$ (mM)			
	Fit: Subunit[c]	Fit: Subunit and Channel[d]		
${}_{M}K_{D1}$	0.800 +0.281/-0.692[b]	0.831 +0.227/-0.228[b]		
${}_{M}K_{D2}$	0.374 +0.081/-0.319[b]	0.407 +0.049/-0.093[b]		
${}_{M}K_{D3}$	0.955 +0.330/-0.862[b]	1.016 +0.275/-0.296[b]		
	Exponent of [AMP-PNP]			
	Fit: Subunit[c]	Fit: Subunit and Channel[d]		
n	2.442 +14.970/-0.661[b]	3.240 +0.670/-0.620[b]		

[a] Probabilities calculated from the number of observed events per state, relative to the total. Standard errors calculated based on variance in measurements from multinomial distribution.

[b] 95% confidence intervals from Chi Squared optimization

[c] Fit of Equation 3.6 to the plots in Figure 3.8B

[d] Simultaneous fit of Equation 3.6 to the plots in Figure 3.8B and Equation 3.16 to the P_o versus [ATP] electrophysiological data

3.3.2.5 Analytic solution for the TrkAH open probability dependence on [ADP]

To account for the ADP effect on the open probability, we have assumed that binding to this ligand converts the gating ring into a tetramer of independent dimers, where each RCK dimer is equally likely to adopt any of the three observed states, independently of the behavior of the remaining dimers. In this case, the concentration of regulatory modules that can open the channel is:

$$[{}_DRM_o] = [({}_DS_2)_4] = {}_{a2}K^4[{}_DS_2]^4$$

3. 19

where ${}_{a2}K$ is the association constant between the four TrkA dimers. The total regulatory module concentration is:

$$[{}_DRM] = \sum\nolimits_{k=0}^{4}\sum\nolimits_{j=0}^{4-k} N_{j,k}\left[({}_DS_1)_j({}_DS_2)_k({}_DS_3)_{4-j-k}\right]$$

3. 20

with the coefficient $N_{j,k}$ specifying the number of times a given subunit combination occurs:

$$N_{j,k} = \frac{4!}{(4-j-k)!\,j!\,k!}$$

3. 21

Expressing Equation 3.20 in terms of individual dimer concentrations and the inter-dimer association constant ${}_{a2}K$, and applying the binomial theorem yields:

$$\begin{aligned}[{}_DRM] &= {}_{a2}K^4\sum\nolimits_{k=o}^{4}\sum\nolimits_{j=0}^{4-k}\frac{4!}{(4-j-k)!\,j!\,k!}[{}_DS_1]^j[{}_DS_2]^k[{}_DS_3]^{4-j-k} \\ &= {}_{a2}K^4([{}_DS_1]+[{}_DS_2]+[{}_DS_3])^4\end{aligned}$$

3. 22

The resulting TrkAH open probability at saturating ADP concentration is then:

$$ {}_{D}P_o = \frac{[{}_{D}RM_o]}{[{}_{D}RM]} = \frac{[{}_{D}S_2]^4}{([{}_{D}S_1] + [{}_{D}S_2] + [{}_{D}S_3])^4} $$

$$ {}_{D}P_o = \frac{1}{\left({}_{D}K_{1,2} + 1 + {}_{D}K_{3,2}\right)^4} $$

3. 23 – Model-derived minimum P$_o$ expression for the ADP-bound TrkAH channel

Plugging in the experimentally determined parameters ${}_{D}K_{1,2}$ and ${}_{D}K_{3,2}$ (Table 3.2), we obtain the open probability prediction ${}_{D}P_o$ = 0.017, closely approximating the previously reported minimum ${}_{D}P_o$ = 0.015 in the presence of saturating ADP (Cao et al., 2013).

We can now derive a general expression for the open probability dependence on [ADP]:

$$ {}_{D}P_o = \frac{[{}_{apo}RM_o] + [{}_{D}RM_o]}{[{}_{apo}RM] + [{}_{D}RM]} = \frac{[{}_{apo}S_2]^2 + [{}_{D}S_2]^4}{([{}_{apo}S_1] + [{}_{apo}S_2] + [{}_{apo}S_3])^2 + ([{}_{D}S_1] + [{}_{D}S_2] + [{}_{D}S_3])^4} $$

3. 24

From the known relationship:

$$ [{}_{D}S_2]^4 = [{}_{apo}S_2]^2 \left(\frac{[D]}{{}_{D}K_{D2}}\right)^n $$

3. 25

we can rewrite the above expression for ${}_{D}P_o$ in terms of measurable constants:

$$_{D}P_{o} = \frac{1 + \left(\frac{[D]}{_{D}K_{D2}}\right)^{n}}{\left(K_{1,2} + 1 + K_{3,2}\right)^{2} + \left(\frac{[D]}{_{D}K_{D2}}\right)^{n}\left(_{D}K_{1,2} + 1 + {_{D}K_{3,2}}\right)^{4}}$$

3. 26 – Whole-channel energetic model for ADP-regulated TrkAH gating

Since the observed RCKs in the TrkAH complex showed no state probability dependence on ADP, we could not experimentally determine the value of the dissociation constant $_{D}K_{D2}$ and, as a result, did not calculate a model-based plot for ADP's effect on TrkAH. In Chapter 2, we demonstrate that the subunit state probabilities depend on [ADP] in the absence of the pore module. Generating a complete dose-response plot for the isolated TrkA with ADP may, in the future, provide us with the information we currently lack.

3.4 Discussion

3.4.1 Implications of the TrkAH energetic model

According to the whole-channel model derived above, the pore will only open when all RCK dimers in the regulatory module are in S_2. In addition, we envision an equilibrium between three configurations – ${}_{D}$RM, ${}_{apo}$RM and ${}_{T}$RM, with different degrees of inter-RCK coupling (Figure 3.13):

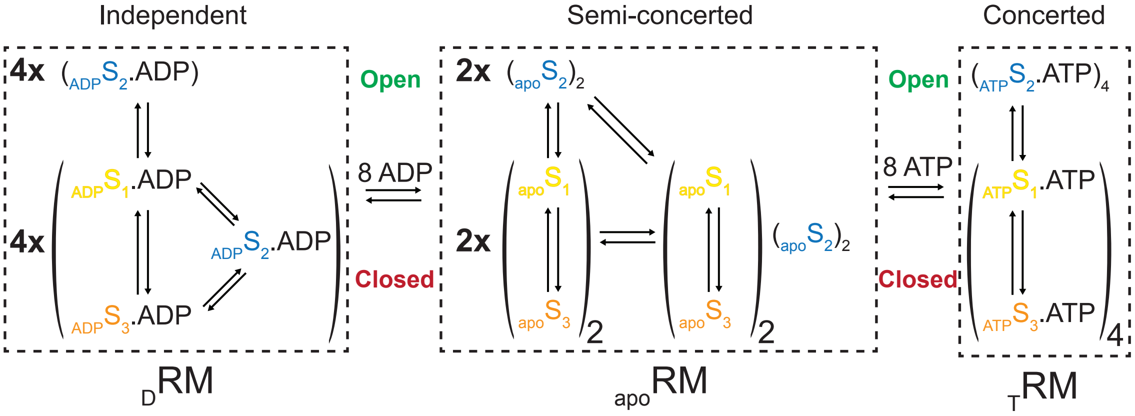

Figure 3. 13 – Model of the TrkA regulatory module in three configurations

In this state diagram, the regulatory module configurations ${}_{D}$RM, ${}_{apo}$RM and ${}_{T}$RM are at equilibrium that is under ADP and ATP control. The channel is open when all four RCK dimers adopt S_2, regardless of whether they are bound to ligand. In the ${}_{D}$RM closed states, four RCK dimers independently adopt any of the three conformations. In the ${}_{apo}$RM closed states, two RCK tetramers independently adopt the $(S_2)_2$ or $(S_1)_j(S_3)_{2-j}$ conformations. In configuration ${}_{T}$RM, S_2 is excluded from the closed channel state. Note that a very recent publication (Zhang et al., 2020) has shown that in the whole-channel structure, TrkA likely binds 8 ATP molecules but only 4 ADP molecules.

In configuration ${}_{D}$RM, individual RCK dimers can visit each state independently; as a result, the subunit combination $(S_2)_4$ is one out of 3^4 allowed subunit permutations, rendering the TrkAH open probability extremely low. In configuration ${}_{apo}$RM, TrkA behaves like a dimer of tetramers, and the RCK dimers in each ring half visit S_2 in a concerted fashion, or else reside in some combination of S_1 and S_3. Relative to ${}_{D}$RM, the ${}_{apo}$RM configuration is much more likely to randomly visit the $(S_2)_4$ subunit combination and open the pore. Lastly, in configuration ${}_{T}$RM, the four RCK dimers, comprising the gating ring, are fully coupled with each other and transition concertedly between S_2 and combinations of S_1 and S_3. The ${}_{T}$RM configuration maximizes the probability of observing the $(S_2)_4$ subunit combination and hence the TrkAH open probability. Just as in the MthK gating ring example, ligand binding to TrkA regulates the number and identity of allowed subunit state combinations, thus controlling the probability of a desired outcome (Lewis and Lu, 2019b).

3.4.2 Mechanistic interpretation of the c_L, c_{Ea} and c_{EI} scaling factors

The model-derived expression, relating P_o to [AMP-PNP] (Equation 3.13) was scaled by three factors prior to achieving near perfect agreement with the experimental P_o vs [ATP] dose response. As stated earlier, the c_L factor accounts for the difference in efficacy of the ATP and AMP-PNP channel activators, whereas c_{Ea} and c_{EI} reflect the energetic differences between the fluorescence- and electrophysiology-based experiments and provide a straightforward way to estimate random and systematic error.

To gain a better understanding of the physical meaning behind the three scaling factors, we re-derived the model P_o expression in terms of the equilibrium constants for the ligand-free TrkA subunits and the three dissociation constants ${}_{M}K_{D1}$, ${}_{M}K_{D2}$ and ${}_{M}K_{D3}$ that describe the affinity of each subunit state for AMP-PNP:

$${}_{M}P_o = \frac{1+\left(\frac{[M]}{{}_{M}K_{D2}}\right)^n}{1+\left(\frac{[M]}{{}_{M}K_{D2}}\right)^n + \left(K_{1,2}+K_{3,2}\right)\left(K_{1,2}+2+K_{3,2}\right) + \left[K_{1,2}^2\left(\frac{[M]}{{}_{M}K_{D1}}\right)^n + K_{3,2}^2\left(\frac{[M]}{{}_{M}K_{D3}}\right)^n\right]}$$

3. 27 – Alternative representation of the energetic model for TrkAH activation by AMP-PNP

Our initial model curve (Figure 3.11A) consistently underestimates the observed P_o vs [ATP] dose response plot, suggesting that unliganded TrkAH is somewhat more likely to be closed in our experiment than in the electrophysiology experimental setup. This is equivalent to saying that in the absence of ligand the individual TrkA subunits are slightly more likely to visit S_1 and S_3 in our fluorescence-based experiment than they are in the electrophysiology experiment:

$$K = \frac{[C]}{[O]}$$

$$^{EP}K < {}^{FP}K \Leftrightarrow {}^{EP}K_{1,2} + {}^{EP}K_{3,2} < {}^{FP}K_{1,2} + {}^{FP}K_{3,2}$$

3. 28

The c_{Ea} scaling factor accounts for this phenomenon and provides an estimate for the corresponding energetic difference between the two experiment types:

$$^{EP}K_{1,2} + {}^{EP}K_{3,2} = c_{Ea}{}^{FP}K_{1,2} + c_{Ea}{}^{FP}K_{3,2}$$

$$\Delta\Delta G_{Ea} = -kTln(c_{Ea})$$

3. 29 – Mechanistic interpretation of the c_{Ea} scaling factor

After accounting for the difference in protein conformational energetics discussed above, any remaining discrepancy between model and observation is due to differences in ligand binding energetics. Our model P_o vs [AMP-PNP] ligand dependence trend predicts a lower $P_{o,max}$ value than the one predicted by electrophysiology, consistent with the C.L species being slightly more favored in the fluorescence- than in the electrophysiology-based experiments. In other words, there is a slightly greater affinity of the ligand for TrkA subunits in S_1 and S_3 in our experimental setup than in the electrophysiology one:

$$K' = \frac{[C.L]}{[O.L]}$$

$${}^{EP}_{T}K' < {}^{FP}_{M}K'$$

$$\frac{{}^{EP}_{T}K_{D2}}{{}^{EP}_{T}K_{D1}} + \frac{{}^{EP}_{T}K_{D2}}{{}^{EP}_{T}K_{D3}} > \frac{{}^{FP}_{M}K_{D2}}{{}^{FP}_{M}K_{D1}} + \frac{{}^{FP}_{M}K_{D2}}{{}^{FP}_{M}K_{D3}}$$

3. 30

This difference in ligand binding energetics is partially accounted for by the c_L factor, reflecting the difference in efficacy between ATP and AMP-PNP:

$$\frac{{}^{FP}_{T}K_{D2}}{{}^{FP}_{T}K_{D1}} + \frac{{}^{FP}_{T}K_{D2}}{{}^{FP}_{T}K_{D3}} = c_L\,\frac{{}^{FP}_{M}K_{D2}}{{}^{FP}_{M}K_{D1}} + c_L\,\frac{{}^{FP}_{M}K_{D2}}{{}^{FP}_{M}K_{D3}}$$

3. 31 – Mechanistic interpretation of the c_L scaling factor

The c_{El} scaling factor provides an estimate for ligand binding energetic differences, arising from random and systematic errors in the two experimental setups:

$$\frac{{}^{EP}_{T}K_{D2}}{{}^{EP}_{T}K_{D1}} + \frac{{}^{EP}_{T}K_{D2}}{{}^{EP}_{T}K_{D3}} = c_{El}\,\frac{{}^{FP}_{T}K_{D2}}{{}^{FP}_{T}K_{D1}} + c_{El}\,\frac{{}^{FP}_{T}K_{D2}}{{}^{FP}_{T}K_{D3}}$$

$$\Delta\Delta G_{El} = -kTln(c_{El})$$

3. 32 – Mechanistic interpretation of the c_{El} scaling factor

Applying all three scaling factors discussed above to Equation 3.27, yields a version of Equation 3.16 that clearly reflects the physical meanings of c_L, c_{Ea} and c_{El}:

$$
{}_{T}P_o = \frac{1 + \left(\frac{[M]}{{}_{M}K_{D2}}\right)^n}{1 + \left(\frac{[M]}{{}_{M}K_{D2}}\right)^n + \left(c_{Ea}K_{1,2} + c_{Ea}K_{3,2}\right)\left(c_{Ea}K_{1,2} + 2 + c_{Ea}K_{3,2}\right) + \left[\left(c_{Ea}K_{1,2}\right)^2\left(c_{El}c_L\frac{[M]}{{}_{M}K_{D1}}\right)^n + \left(c_{Ea}K_{3,2}\right)^2\left(c_{El}c_L\frac{[M]}{{}_{M}K_{D3}}\right)^n\right]}
$$

3. 33 – Model for TrkAH activation, reflecting the mechanistic meanings of c_L, c_{Ea} and c_{El}

3.4.3 Regulation of inter-RCK coupling by ATP and ADP

Ligand-regulated inter-RCK coupling of the type predicted by our model is not clearly reflected by the two known TrkA structures, but is illustrated very convincingly by the high-resolution structures of the regulatory module from the related K^+ transporter Ktr (Vieira-Pires et al., 2013). Ktr belongs to the same superfamily of transporters as Trk and utilizes a K^+-selective two-pore module, structurally homologous to TrkH. The Ktr gating ring, KtrA, is an octamer of identical RCK units, each of which can bind the ligands ATP or ADP, affecting pore opening. The ATP- and ADP-bound KtrA structures, resolved to 3.2 Å and 2.9 Å, respectively, display different ring conformations (Figure 3.14A, B). Importantly, the binding pockets of sister RCK units can become coupled by ATP and uncoupled by ADP, with the critical involvement of residues R16 and K103 (Figure 3.14C, D). When an ATP molecule occupies a particular RCK unit's binding pocket, the γ-phosphate interacts with the R16 and K103 side chains from the same binding pocket (P_{site1}), while the β-phosphate contacts the R16 side chain from the sister binding pocket (P_{site2}). Since each sister RCK unit binds to one ATP molecule, this kind of binding pocket sharing occurs twice per RCK pair. These inter-RCK interactions, mediated by ATP, bring the two sister RCK cores closer together by 5 Å and increase the hinge angle by 16°. Conversely, in the ADP-bound structure, P_{site1} is occupied by the ligand's β-phosphate, while P_{site2} is vacant, causing the two sister RCK units to disengage. As explained next, TrkA may employ a similar mechanism of ligand-regulated inter-RCK coupling.

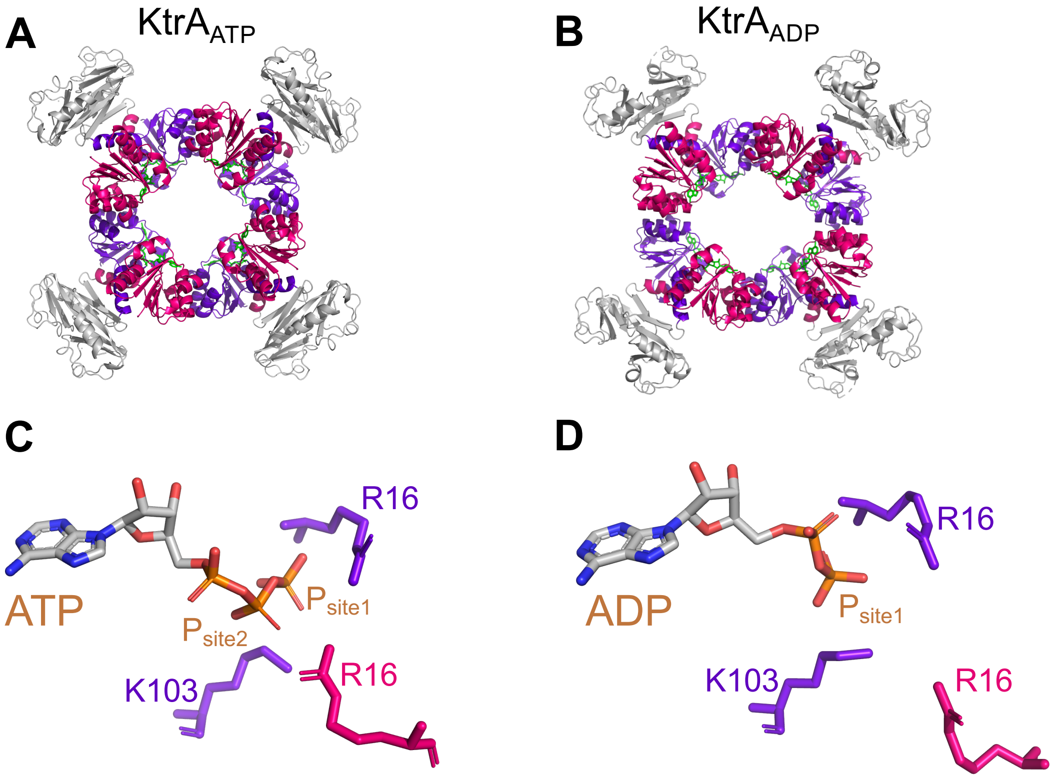

Figure 3. 14 – ATP and ADP effects on inter-RCK coupling in the KtrA gating ring

(A) Crystal structure of the ATP-bound isolated KtrA regulatory module (PDB: 4J90). **(B)** Crystal structure of the ADP-bound isolated KtrA regulatory module (PDB: 4J91). **(C)** Binding pocket from the ATP-bound KtrA structure with two phosphate binding sites: P_{site1}, occupied by a γ-phosphate and P_{site2}, occupied by a β-phosphate. This ligand-binding mode promotes coupling between sister RCK units. **(D)** Binding pocket from the ADP-bound KtrA structure with a single phosphate binding site, P_{site1}, occupied by the ligand's β-phosphate. This ligand-binding mode disrupts coupling between sister RCK units.

The critical amino acid R16 introduced above, is the 4th residue in the GXGXXG phosphate binding consensus sequence of KtrA (see Section 1.3). The same position in TrkA's RCK1 and RCK2 fingerprint regions is occupied by residues Q10 and N242, respectively. The second mentioned residue, K103, is located at the C-terminal tip of the βE strand in KtrA and is conserved in both RCK motifs of TrkA, where the tips of βE1 and βE2 harbor residues R100 and R332, respectively. Although TrkA contains all necessary residues to recreate the binding pocket sharing scheme employed by KtrA, neither the $\mathrm{TrkA_{twist}}$ nor the $\mathrm{TrkA_{flat}}$ structures supports such a scheme (Figure 3.15A-D). In the ATP-γS-bound structure, $\mathrm{TrkA_{twist}}$, the positions of Q10 and N242 do not allow these residues to bridge two sister ligand binding sites (Figure 3.15A, B). Furthermore, the β-phosphate of ATP-γS in the RCK1 binding pocket interacts with R100 but not Q10, while the β-phosphate of ATP-γS in the RCK2 binding pocket interacts with neither N242 nor R332. Instead of participating in ligand binding, residues Q10, N242 and R332 point away from the binding sites. In the NADH-bound $\mathrm{TrkA_{flat}}$ structure, both residues Q10 and N242 are directed towards their own binding pockets, the R100 side chain points towards the sister RCK2 binding pocket, and R332 is once again too far from either ligand binding site (Figure 3.15C, D). The apparent unavailability of R332 for ligand binding in both structures may be a crystallization artifact or reflect a real difference in the ligand binding schemes of TrkA and KtrA. Given the latter possibility, an alternative mechanism for sister RCK unit coupling can be proposed for TrkA, whereby residue R100, approximately equidistant from two sister binding pockets, plays a similar role to KtrA's R16 and is shared by the RCK1 and RCK2 ligand binding sites in the presence of ATP, but exclusively serves the RCK1 site in the presence of ADP. In fact, it was previously demonstrated that the R100A mutation in TrkA completely abolishes the whole-channel ATP sensitivity (Cao et al., 2013).

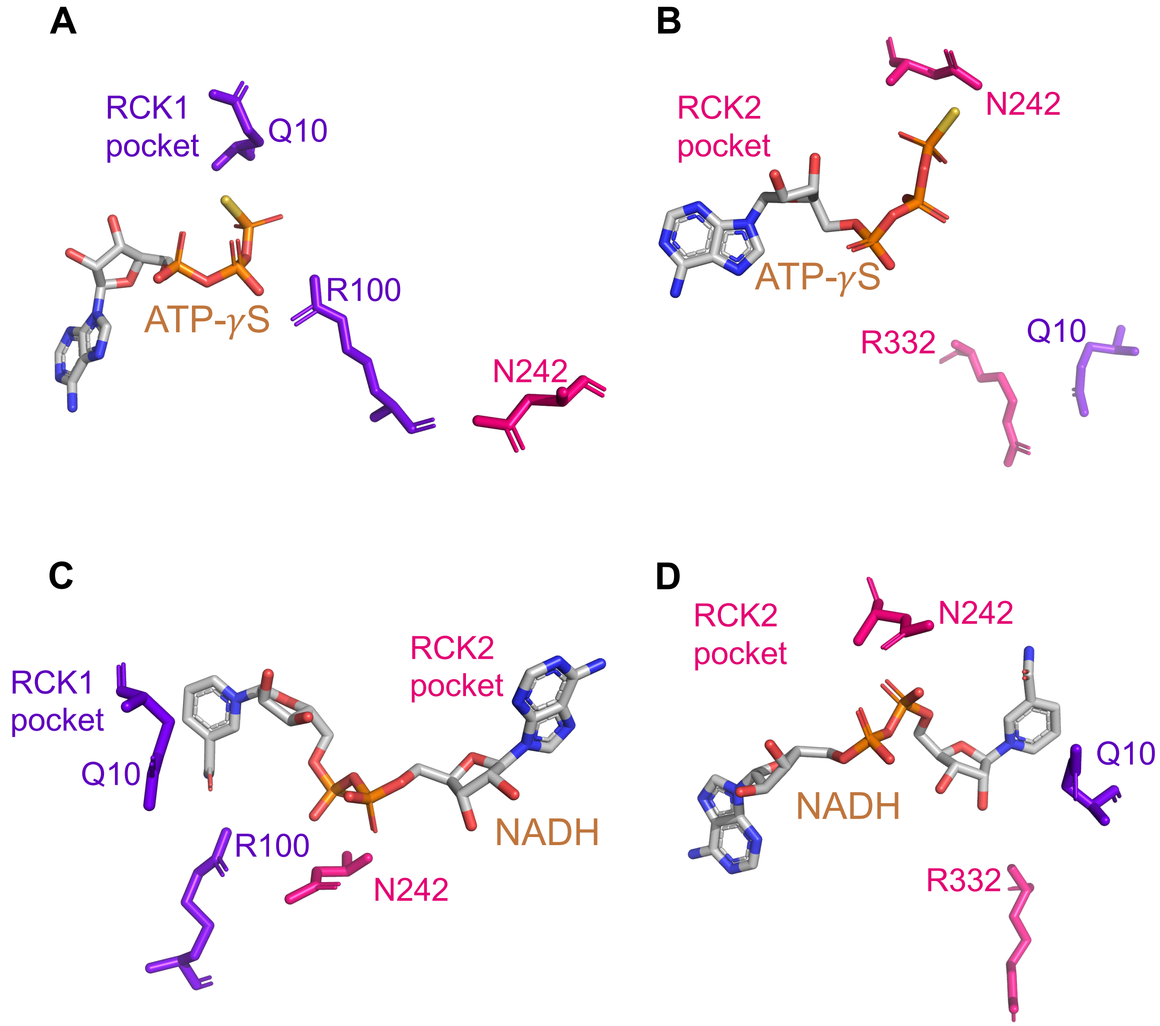

Figure 3. 15 – Exploring potential inter-RCK coupling in the TrkA gating ring

(A) RCK1 binding pocket, occupied by ATP-γS (PDB: 4J9V). R100 points towards the binding pocket of its own RCK unit and coordinates the ligand's β-phosphate. **(B)** RCK2 binding pocket, occupied by ATP-γS. No residues make critical contacts with the ligand's phosphate groups. **(C)** Vacant RCK1 and NADH-bound RCK2 binding pockets (PDB: 4J9U). Residue N242 contacts one of the ligand's phosphate groups. R100 points towards the binding pocket of the sister RCK unit and is properly positioned for potential inter-RCK coupling. **(D)** RCK2 binding pocket, occupied by NADH. Residue R332 has no notable involvement in ligand binding.

While this thesis was in its final preparation stages, an update was published on the whole-channel TrkAH structure bound to ATP-, ADP- or ATP-γS (Zhang et al., 2020). Many of the findings, detailed in this publication, support our model-based predictions, but time restrictions and the current unavailability of the structures on the Protein Data Bank website prevent us from providing an adequate discussion here. Of note, this paper confirms our prediction that the number of independent structural components in TrkA is increased by ADP and decreased by ATP, an effect that may involve ligand-dependent regulation of inter-RCK coupling. Like the previously published structure of TrkA-ATPγS ($\text{TrkA}_{\text{twist}}$, PDB: 4J9V), TrkAH-ATPγS also contains 8 copies of the ligand, albeit with better coordination at each binding site. In RCK1, conserved residues R98 and R100 form salt bridges with the γ- and β-phosphate, respectively, and in RCK2, N242 coordinates the β-phosphate, while no residue coordinates the γ-phosphate of ATP-γS. The TrkAH-ATP structure has a different conformation from TrkAH-ATPγS, but is only partially resolved, preventing detailed inspection of the binding pockets. Importantly, the pore is open in TrkAH-ATP and partially open in TrkAH-ATPγS, which may be the result of incomplete inter-RCK coupling in the case of the latter structure. We suspect that were the TrkAH-ATP structure better-resolved, if may have reflected the role of R100 in the coordination of the γ-phosphate of ATP in the sister RCK2 ligand-binding site. Notably, TrkA-ADP harbors only 4 ADP molecules, one in each RCK2 pocket, and the ligand coordination scheme is nearly identical to that of ATP-γS, including the involvement of N242 in β-phosphate coordination. This gating ring conformation likely disengages R100 from the RCK2 binding site and promotes sister RCK uncoupling. Future access to the recently deposited structures will enable us to make better mechanistic predictions about ligand-regulated inter-RCK coupling and pore gating. Guided by these new structural insights, we can generate suitable Trk mutants to use as targets in future single-molecule fluorescence-based studies.

The main model equations from this chapter are summarized in the box below:

Equation 3.6:
Model for RCK state probability dependence on ligand concentration

$$P_i = \frac{K_{i,2} + {}_{M}K_{i,2}\left(\frac{[M]}{{}_{M}K_{D2}}\right)^n}{\left(K_{1,2} + 1 + K_{3,2}\right) + \left(\frac{[M]}{{}_{M}K_{D2}}\right)^n \left({}_{M}K_{1,2} + 1 + {}_{M}K_{3,2}\right)}$$

Equation 3.13:
Whole-channel energetic model for ligand-induced activation of TrkAH

$${}_{M}P_o = \frac{1 + \left(\frac{[M]}{{}_{M}K_{D2}}\right)^n}{1 + \left(\frac{[M]}{{}_{M}K_{D2}}\right)^n + \left(K_{1,2} + K_{3,2}\right)\left(K_{1,2} + 2 + K_{3,2}\right) + \left({}_{M}K_{1,2} + {}_{M}K_{3,2}\right)\left(\frac{[M]}{{}_{M}K_{D2}}\right)^n}$$

Equation 3.16:
Energetic model for AMP-PNP-induced activation of TrkAH, scaled by c_L, c_{Ea} and c_{El}

$${}_{T}P_o = \frac{1 + \left(\frac{[M]}{{}_{M}K_{D2}}\right)^n}{1 + \left(\frac{[M]}{{}_{M}K_{D2}}\right)^n + c_{Ea}^2\left(K_{1,2} + K_{3,2}\right)\left(K_{1,2} + 2 + K_{3,2}\right) + c_{Ea}^2 c_{El}^n c_L^n\left({}_{M}K_{1,2} + {}_{M}K_{3,2}\right)\left(\frac{[M]}{{}_{M}K_{D2}}\right)^n}$$

Equation 3.26:
Whole-channel energetic model for ADP-regulated TrkAH gating

$${}_{D}P_o = \frac{1 + \left(\frac{[D]}{{}_{D}K_{D2}}\right)^n}{\left(K_{1,2} + 1 + K_{3,2}\right)^2 + \left(\frac{[D]}{{}_{D}K_{D2}}\right)^n \left({}_{D}K_{1,2} + 1 + {}_{D}K_{3,2}\right)^4}$$

CHAPTER 4: MECHANISTIC COMPARISON BETWEEN THE TRKAH AND MTHK ION CHANNELS

4.1 Structure-function comparison between TrkAH and MthK

The overarching goal of this thesis has been to compare the gating energetics of two bacterial K^+-selective systems – TrkAH and MthK. These two nonhomologous systems have different structures and very little in common functionally, other than the fact that both conduct K^+. TrkAH consists of the two-pore module TrkH and the two-fold symmetric regulatory module TrkA that binds to ATP or ADP to increase or decrease the channel's open probability, respectively (Cao et al., 2013; Figure 4.1A, B).

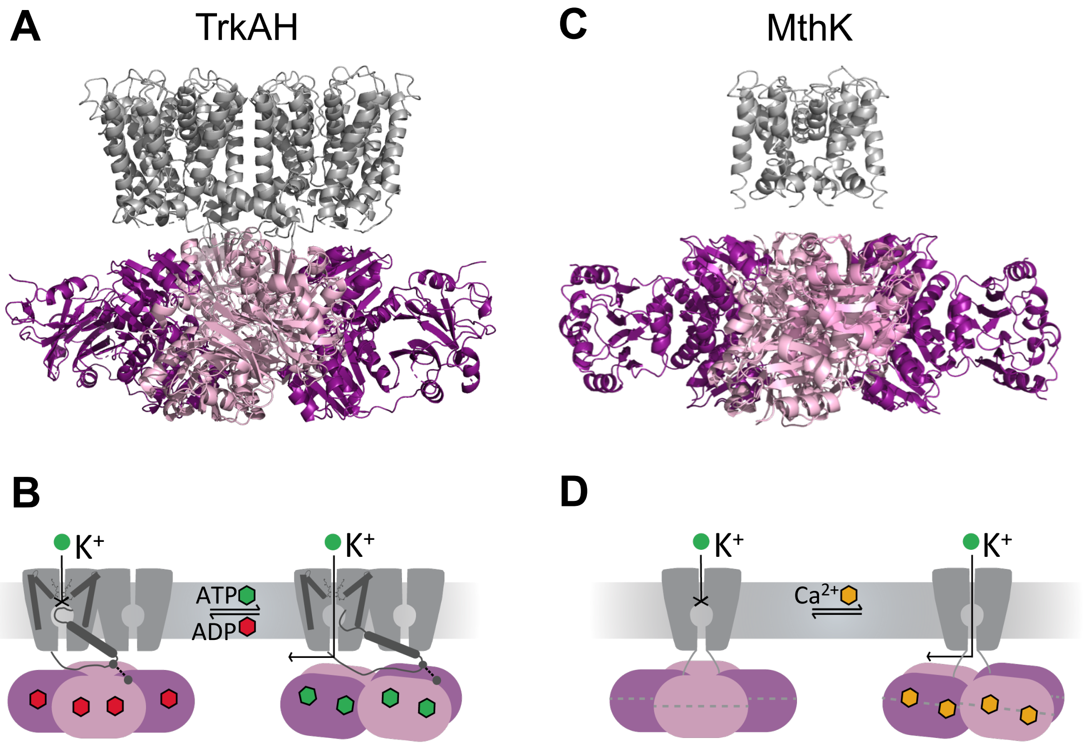

Figure 4. 1 – Structural comparison between the TrkAH and MthK ion channels

(A) Whole-channel structure of the closed TrkAH complex (PDB: 4J9U). **(B)** Proposed gating mechanism for TrkAH by ATP and ADP. **(C)** Whole-channel structure of MthK in the open state (PDB: 1lnq). **(D)** Proposed gating mechanism for MthK by Ca^{2+}. This figure was partially adapted from Cao et al., 2013.

The closed TrkAH structure predicts that this channel's opening mechanism likely involves the displacement of a long pore-occluding intramembrane loop from the pore vestibule. MthK, on the other hand, is a Ca^{2+}-gated K^+ channel with a four-fold symmetric single-pore module, built from four identical subunits (Jiang et al., 2002a; Figure 4.1C). Each pore subunit in MthK contains two membrane-spanning segments, followed by a C-terminal sequence, encoding the RCK unit fold. In addition to the four RCK units covalently linked to the pore-forming peptide chains, the MthK gating ring contains four RCK copies, expressed from an internal transcription start site within the full-length *MthK* gene. Thus, the MthK gating ring is assembled from eight identical RCK units and the top ring layer contains four RCK units that are covalently attached to the pore module (Jiang et al., 2002a; Ye et al., 2006). In order to open the MthK channel, four pore-lining helices must bend at a conserved glycine residue below the pore's selectivity filter, causing a symmetrical widening of the pore vestibule (Jiang et al., 2002b).

To accommodate the different types of gating involved in each system, the Trk and MthK regulatory modules undergo remarkably different conformational changes. Compared to the pronounced transitions between the $TrkA_{flat}$ and $TrkA_{twist}$ structures discussed in Chapter 2 (Figure 2.3), the MthK regulatory module experiences very subtle ligand-induced conformational changes, whereby the ring flattens evenly and expands symmetrically to exert a lateral opening force on the channel's pore (Ye et al., 2006). Given that each regulatory module is an octameric RCK assembly of the type described in Chapter 1, the differences in plasticity between the two gating rings likely arise from the differences in stiffness at the various inter-RCK interfaces (Figure 4.2). The conformational flexibility at sister RCK interfaces is significantly more constrained by the peripheral subdomain in MthK than in Trk, causing the MthK hinge angle to span a narrower mobility range (129-138°) than the TrkA hinge angle (93-120°). In addition, all neighbor RCK interfaces in the isolated MthK gating ring are of the fixed type, whereas the isolated TrkA has only two diametrically opposed fixed interfaces (Figure 4.2C, D). Importantly, since MthK's RCK1 and RCK2 units are identical, the four neighbor RCK interfaces in the gating ring are the same. Thus, the isolated MthK gating ring has four identical sister RCK interfaces and four identical neighbor RCK interfaces; this continues to be true even in the presence of the pore module as the latter contacts every RCK unit core at the top half of the gating ring. In contrast, TrkA has three distinct types of interfaces when isolated and four in the presence of the pore module (Figure 2.2B, C). Overall, despite their nearly identical architectures, the MthK and Trk gating rings differ in their patterns of energy storage at individual RCK interfaces and, as a result, generate different force outputs.

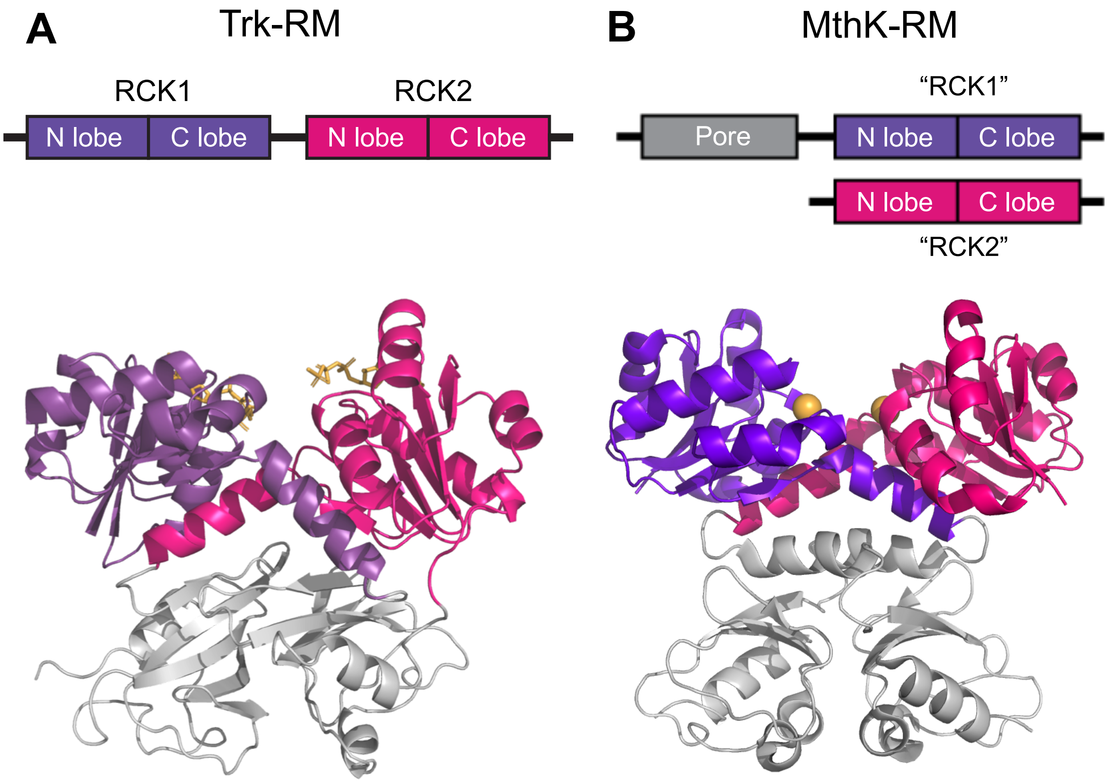

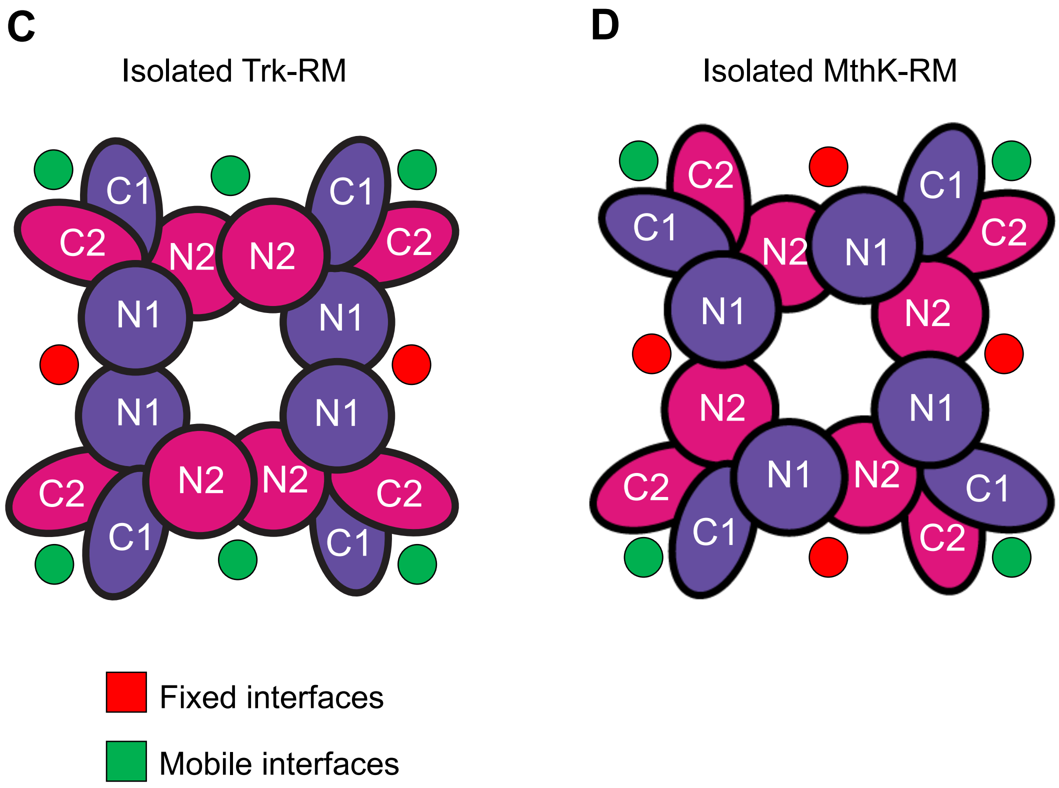

Figure 4. 2 – Comparison of inter-RCK interfaces in the isolated Trk and MthK gating rings

(A) The Trk RCK dimer contains a tandem pair of homologous RCK units (PDB: 4J9V). **(B)** The MthK RCK dimer is built from two identical RCK units (PDB: 1lnq). **(C)** The isolated Trk gating ring contains six mobile and two diametrically opposed fixed interfaces. **(D)** The isolated MthK gating ring contains four identical fixed interfaces and four identical mobile interfaces. This figure was partially adapted from Cao et al., 2013.

Not surprisingly, TrkAH and MthK, with their different pore architectures, ligand preferences and gating ring flexibilities, exhibit distinct P_o dose-response relationships to ligand. In the absence of ligand, TrkAH is already active with an open probability of 0.17; ATP further activates the channel by both reducing the closed-state and lengthening the open-state lifetimes. As the ATP concentration increases, so does the channel's P_o, reaching a maximum value of 0.87 with a Hill slope of 3.4; ADP has the opposite effect on the channel, decreasing its P_o to nearly zero with a Hill coefficient of 1.7. In comparison, unliganded MthK almost never visits the open state; Ca^{2+} activates the channel by substantially reducing the lifetime of the closed state and modestly increasing the lifetime of the open state (Pau et al., 2010; Zadek and Nimigean, 2006). MthK displays a steep Ca^{2+}-dependent P_o increase from 0 to 1 with a Hill coefficient of 4. Despite the many structural and functional differences between the two ion channels, their gating is ultimately regulated by ligand-induced conformational changes in individual RCK motifs, whose structure is conserved. Therefore, we hypothesized that the gating energetics of TrkAH and MthK follow the same fundamental principles.

4.2 Gating energetics of TrkAH and MthK

The work detailed in this thesis has been guided by the following research questions, regarding the Trk and MthK regulatory modules: (1) In each RCK octamer, what are the intrinsic energetics of an individual RCK component, in the absence or presence of ligand? (2) In each gating ring, how must an individual RCK motif energetically relate to the remaining seven, in order to generate the desired functional output, i.e. to regulate the open probability of a particular pore? (3) What are the energetic commonalities between the gating mechanisms for the Trk and MthK whole-channel systems, from an RCK-centered point of view?

With our single-molecule fluorescence-based approach, we have observed ligand-induced conformational changes of individual RCK motifs in the Trk and MthK regulatory modules; a summary of our findings is presented in Table 4.1 below:

Table 4. 1 – Fitted parameters of the Trk and MthK RCK models and subunit state probabilities at min and max ligand

Trk Result Summary:				MthK Result Summary:			
Equilibrium Constants at Zero AMP-PNP		Probabilities at Zero AMP-PNP		Equilibrium Constants at Zero Ca^{2+}		Probabilities at Zero Ca^{2+}	
$K_{1,2}$	0.777+0.098/-0.061	P_1	0.313±2.33E-2	$K_{1,2}$	0.768+0.042/-0.084	P_1	0.298±7.14E-3
$K_{3,2}$	0.940+0.135/-0.239	P_2	0.372±2.43E-2	$K_{3,2}$	0.808+0.068/-0.087	P_2	0.388±7.69E-3
$K_{1,3}$	0.826+0.158/-0.220	P_3	0.315±2.34E-2	$K_{1,3}$	0.950+0.095/-0.146	P_3	0.314±7.37E-3
Equilibrium Constants at Saturating AMP-PNP		Probabilities at 25 mM AMP-PNP		Equilibrium Constants at Saturating Ca^{2+}		Probabilities at 50 mM Ca^{2+}	
${}_{M}K_{1,2}$	0.363+0.089/-0.043	${}_{M}P_1$	0.193±2.35E-2	${}_{ca}K_{1,2}$	0.374+0.012/-0.036	${}_{ca}P_1$	0.239±7.57E-3
${}_{M}K_{3,2}$	0.368+0.084/-0.055	${}_{M}P_2$	0.557±2.96E-2	${}_{ca}K_{3,2}$	0.219+0.021/-0.037	${}_{ca}P_2$	0.607±8.46E-3
${}_{M}K_{1,3}$	0.986+0.330/-0.188	${}_{M}P_3$	0.250±2.58E-2	${}_{ca}K_{1,3}$	1.708+0.173/-0.332	${}_{ca}P_3$	0.154±5.79E-3
${}_{M}K_D$ (mM)				${}_{ca}K_D$ (mM)			
${}_{M}K_{D1}$	0.800+0.281/-0.692			${}_{ca}K_{D1}$	0.501+0.285/-0.159		
${}_{M}K_{D2}$	0.374+0.081/-0.319			${}_{ca}K_{D2}$	0.244+0.138/-0.069		
${}_{M}K_{D3}$	0.955+0.330/-0.862			${}_{ca}K_{D3}$	0.900+0.522/-0.312		
Exponent of [AMP-PNP]				Exponent of [Ca^{2+}]			
n	2.442+14.970/-0.661			n	0.643+0.073/-0.092		

Our result comparison supports the prediction that the structurally conserved RCK motif exhibits essentially the same intrinsic energetics in the Trk as in the MthK gating ring. In each system, the unliganded RCK component visits one of three states, with probabilities $P_1 \approx 0.3$, $P_2 \approx 0.4$ and $P_3 \approx 0.3$; saturating concentrations of an activating ligand favor a new equilibrium with ${}_{L}P_1 \approx 0.2$, ${}_{L}P_2 \approx 0.6$ and ${}_{L}P_3 \approx 0.2$. Despite their different ligand preferences, the Trk and MthK RCK units bind to their respective activators with comparable binding affinities. The ligand dependence of the RCK unit states in Trk is steeper than that in MthK, possibly because, unlike the MthK data, the Trk data were collected in presence of the pore module. Having described the intrinsic RCK unit energetics, we set out to understand and compare the energetic relationships between all eight RCK units in each gating ring in the context of pore gating.

In Chapter 3 of this thesis, we derive an energetic model for TrkAH gating by ATP and ADP, summarized in Figure 4.3 below:

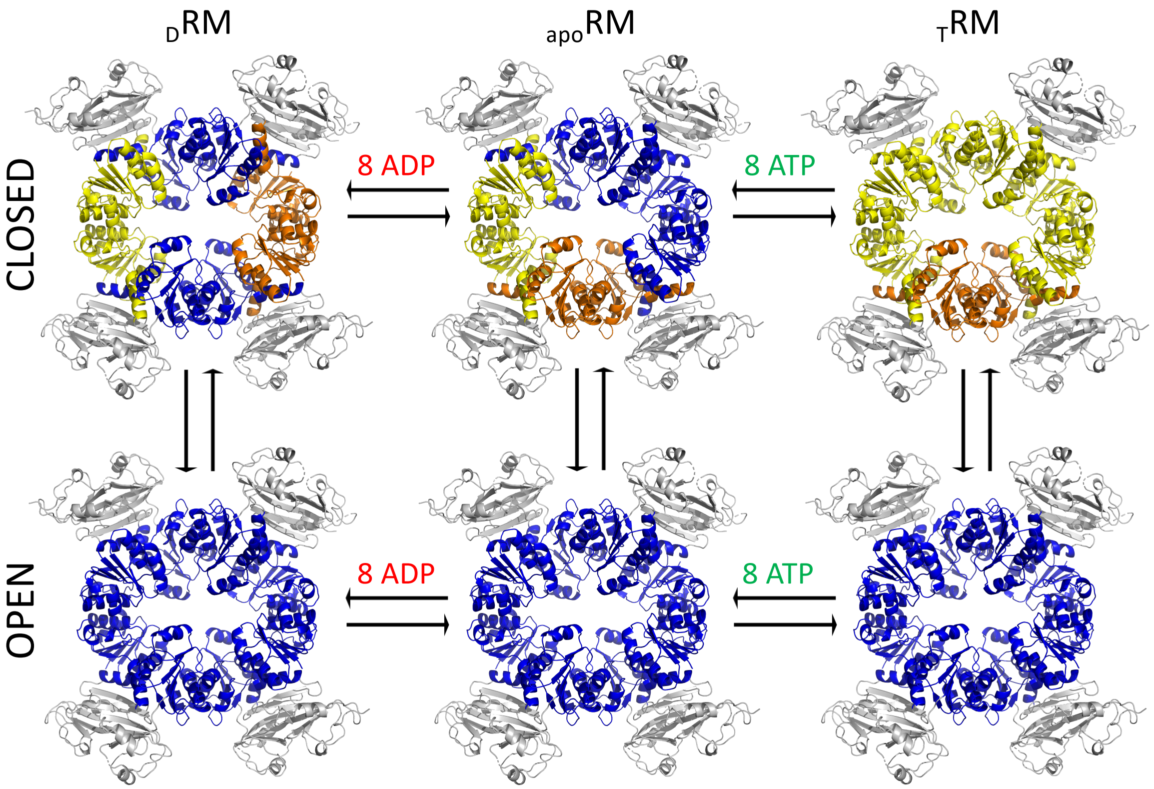

Figure 4. 3 – Summary of the TrkAH whole-channel energetic model

RCK dimers in S_1, S_2 or S_3 are colored in yellow, blue or orange, respectively. Note that a very recent publication (Zhang et al., 2020) has shown that the regulatory module in the TrkAH complex likely binds 8 ATP molecules but only 4 ADP molecules.

According to this model, individual RCK units in the regulatory module exist in one of three states, S_1, S_2 or S_3 with probabilities P_1, P_2 and P_3, respectively. The model assumes that the channel only opens when all eight RCK units are simultaneously in S_2 and that the smallest possible independent component of the regulatory module is the RCK dimer. Our model predicts an equilibrium between three regulatory module configurations: the ADP-bound $_{D}$RM, the ligand-free $_{apo}$RM and the ATP-bound $_{T}$RM configurations. In $_{D}$RM, individual RCK dimers can visit each of the three states independently of one another, resulting in a low probability of observing the $(S_2)_4$ gating ring conformation and thus a low open probability for the channel. Conversely, the $_{T}$RM configuration completely excludes S_2 from the channel's closed state; in other words, individual RCK dimers can either all adopt S_2 or be any combination of S_1 and $S_{3.}$ When the regulatory module is in $_{T}$RM, channel opening involves the concerted transition of all four RCK dimers from the $(S_2)_4$ to the $(S_1)_j(S_3)_{4-j}$ subunit combination. The $_{T}$RM configuration maximizes the probability of observing the all-S_2 gating ring state and hence the channel's open probability. Our model accounts for the significant activity of the unliganded channel by predicting a third, intermediate configuration $_{apo}$RM, in which the gating ring is split into two independent halves. In $_{apo}$RM, S_2 does not coexist with S_1 and S_3 in either of the two independent ring halves, setting the probability of obtaining the $(S_2)_4$ subunit combination at an intermediate value. Note that each ligand regulates the coupling between gating ring components, so that the energy of ligand binding is used to change the system's entropy.

The energetic model for Ca^{2+}-regulated MthK gating was derived previously and is based on observations from the isolated regulatory module in absence of pore (Lewis and Lu, 2019b; Figure 4.4):

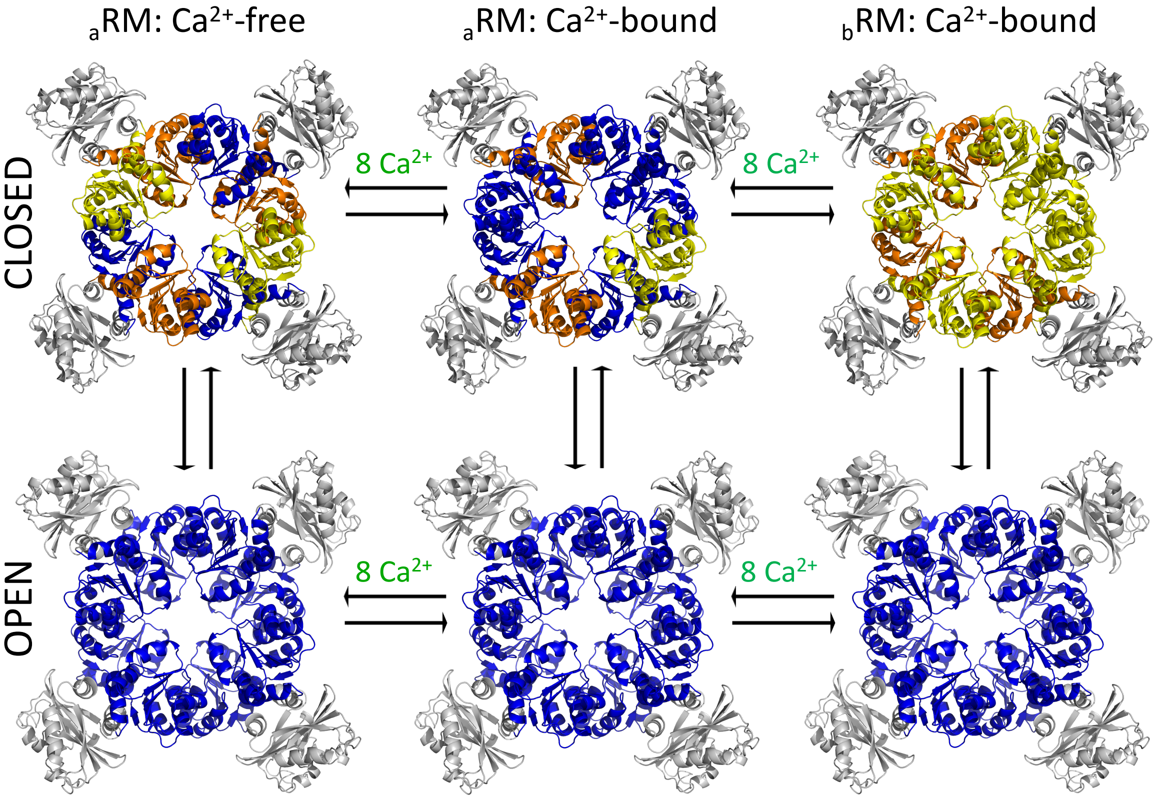

Figure 4. 4 – Summary of the MthK whole-channel energetic model

RCK motifs in S_1, S_2 or S_3 are colored in yellow, blue or orange, respectively.

As in TrkA, the RCK units in MthK can adopt one of three states and only the all-S_2 subunit combination opens the pore module. The MthK model envisions an equilibrium between two gating ring configurations, $_a$RM and $_b$RM, where the former configuration can exist in an unliganded form or bound to Ca^{2+}. MthK's Ca^{2+}-free $_a$RM and Ca^{2+}-bound $_b$RM configurations are identical to TrkA's $_D$RM and $_T$RM, respectively, except that in MthK the RCK unit and not the RCK dimer is considered the gating ring's minimal possible independent component. The effect of Ca^{2+} on the pore open probability is exerted by two routes: changing the intrinsic RCK unit equilibrium in favor of S_2 and strengthening inter-subunit coupling to promote $_{b}$RM. The MthK model accounts for the possibility that Ca^{2+} may exert these parallel effects by binding at distinct gating ring locations. An important prediction from the MthK model is that the $_{b}$RM configuration is energetically inaccessible to the gating ring in the absence of the pore module.

4.3 Fundamental energetic principles derived from comparing the MthK and TrkAH ion channels

Our energetic comparison between the Trk and MthK ion channels shows that despite their many structural and functional differences, the two systems are governed by the same set of energetic rules. First of all, we have demonstrated that the intrinsic energetics of individual RCK components in each gating ring are strikingly similar. The comparable state probabilities and equilibrium constants between the Trk and MthK systems strongly suggest that regardless of which regulatory module it belongs to, the RCK motif resides on essentially the same energy landscape. A second unifying principle, reflected by our comparison, is that the ligand exerts its effect on pore opening by regulating inter-subunit coupling in the regulatory module. In both systems, a desired functional outcome is conditioned upon a particular combination of subunit states and ligand binding affects the probability of observing this combination by controlling the number of independent components. The more independent components a regulatory module contains, the lower the probability of observing a desired subunit state combination. In energetic terms, the energy derived from ligand binding changes the system's entropy by changing the number of possible combinatorial species; the resulting entropic change then fuels the desired functional outcome. This mode of operation inherently requires the presence of multiple copies of the RCK unit that can become coupled or uncoupled in a ligand-dependent fashion. It is therefore not surprising that most structurally characterized RCK-containing proteins include eight copies of the RCK motif.

The energetic principles derived by comparing Trk and MthK may be universal for all existing octameric RCK assemblies. Several such octamers have been structurally characterized and await further mechanistic exploration (Hite et al., 2017; Kong et al., 2013; Vieira-Pires et al., 2017). Given how common the RCK motif is in bacterial ligand-gated K^+-selective systems, our work provides valuable mechanistic insight into a large and diverse group of prokaryotic proteins.

BIBLIOGRAPHY

Adachi, K., Yasuda, R., Noji, H., Itoh, H., Harada, Y., Yoshida, M., & Kinosita, K., Jr. (2000). Stepping rotation of F1-ATPase visualized through angle-resolved single-fluorophore imaging. Proc. Natl. Acad. Sci. U. S. A, 97(13), 7243-7247.

Albright, R. A., Ibar, J. L., Kim, C. U., Gruner, S. M., & Morais-Cabral, J. H. (2006). The RCK domain of the KtrAB K+ transporter: multiple conformations of an octameric ring. Cell, 126(6), 1147-1159. doi:10.1016/j.cell.2006.08.028

Armstrong, C. M. (2015). Packaging life: the origin of ion-selective channels. Biophys J, 109(2), 173-177. doi:10.1016/j.bpj.2015.06.012

Axelrod, D. (1979). Carbocyanine dye orientation in red cell membrane studied by miscroscopic fluororescence polarization. Biophysical Journal, 26, 557-574.

Axelrod, D. (1984). Total internal reflection fluoroscence. Annu. Rev. Biophys. Bioeng, 13, 247-268.

Beausang, J. F., Goldman, Y. E., & Nelson, P. C. (2011). Changepoint analysis for single-molecule polarized total internal reflection fluorescence microscopy experiments. Methods Enzymol, 487, 431-463.

Bellamacina, C. R. (1996). The nicotinamide dinucleotide binding motif: a comparison of nucleotide binding proteins. FASEB J, 10(11), 1257-1269. doi:10.1096/fasebj.10.11.8836039

Bevington, P. R., & Robinson, D. K. (2003). Data Reduction and Error Analysis for the Physical Sciences (P. R. Bevington & D. K. Robinson Eds. 3rd ed.). New York: McGraw-Hill.

Brocchieri, L., & Karlin, S. (2005). Protein length in eukaryotic and prokaryotic proteomes. Nucleic Acids Res, 33(10), 3390-3400. doi:10.1093/nar/gki615

Cao, Y., Jin, X., Huang, H., Derebe, M. G., Levin, E. J., Kabaleeswaran, V., . . . Zhou, M. (2011). Crystal structure of a potassium ion transporter, TrkH. Nature, 471(7338), 336-340. doi:10.1038/nature09731

Cao, Y., Pan, Y., Huang, H., Jin, X., Levin, E. J., Kloss, B., & Zhou, M. (2013). Gating of the TrkH ion channel by its associated RCK protein TrkA. Nature, 496(7445), 317-322. doi:10.1038/nature12056

Chen, J., & Gupta, A. K. (2001). On change point detection and estimation. Communications in Statistics-Simulation and Computation, 30(3), 665-697.

Corratge-Faillie, C., Jabnoune, M., Zimmermann, S., Very, A. A., Fizames, C., & Sentenac, H. (2010). Potassium and sodium transport in non-animal cells: the Trk/Ktr/HKT transporter family. Cell Mol Life Sci, 67(15), 2511-2532. doi:10.1007/s00018-010-0317-7

Corrie, J. E. T., Craik, J. S., & Munasinghe, V. R. N. (1998). A homobifunctional rhodamine for labeling proteins with defined orientations of a fluorophore. Bioconjugate Chemistry, 9(2), 160-167.

Dong, J., Shi, N., Berke, I., Chen, L., & Jiang, Y. (2005). Structures of the MthK RCK domain and the effect of Ca2+ on gating ring stability. J Biol Chem, 280(50), 41716-41724. doi:10.1074/jbc.M508144200

Dosch, D. C., Helmer, G. L., Sutton, S. H., Salvacion, F. F., & Epstein, W. (1991). Genetic analysis of potassium transport loci in Escherichia coli: evidence for three constitutive systems mediating uptake potassium. J Bacteriol, 173(2), 687-696. doi:10.1128/jb.173.2.687-696.1991

Emsley, P., Lohkamp, B., Scott, W. G., & Cowtan, K. (2010). Features and development of Coot. Acta Crystallogr. D Biol. Crystallogr, 66, 486-501.

Epstein, W. (2003). The roles and regulation of potassium in bacteria. Prog Nucleic Acid Res Mol Biol, 75, 293-320. doi:10.1016/s0079-6603(03)75008-9

Erickson, H. P. (2009). Size and shape of protein molecules at the nanometer level determined by sedimentation, gel filtration, and electron microscopy. Biol Proced Online, 11, 32-51. doi:10.1007/s12575-009-9008-x

Forkey, J. N., Quinlan, M. E., & Goldman, Y. E. (2000). Protein structural dynamics by single-molecule fluorescence polarization. Prog. Biophys. Mol. Biol, 74(1-2), 1-35.

Forkey, J. N., Quinlan, M. E., & Goldman, Y. E. (2005). Measurement of single macromolecule orientation by total internal reflection fluorescence polarization microscopy. Biophys. J, 89(2), 1261-1271.

Forkey, J. N., Quinlan, M. E., Shaw, M. A., Corrie, J. E., & Goldman, Y. E. (2003). Three-dimensional structural dynamics of myosin V by single-molecule fluorescence polarization. Nature, 422(6930), 399-404.

Fourkas, J. T. (2001). Rapid determination of the three-dimensional orientation of single molecules. Optics Letters, 26(4), 211-213.

Ha, T., Glass, J., Enderle, T., Chemla, D. S., & Weiss, S. (1998). Hindered rotational diffusion and rotational jumps of single molecules. Physical Review Letters, 80(10), 2093-2096.

Harms, C., Domoto, Y., Celik, C., Rahe, E., Stumpe, S., Schmid, R., . . . Bakker, E. P. (2001). Identification of the ABC protein SapD as the subunit that confers ATP dependence to the K+-uptake systems Trk(H) and Trk(G) from Escherichia coli K-12. Microbiology, 147(Pt 11), 2991-3003. doi:10.1099/00221287-147-11-2991

Hecht, E. (2016). Optics (5th ed.): Addison Wesley.

Hill, A. V. (1910). Possible Effects of the Aggregation of the Molecules of Hemoglobin on Its Dissociation Curves. Journal of Physiology, 40, iv-vii.

Hille, B. (2001). Ion Channels of Excitable Membranes (Third ed.). Sunderland, MA: Sinauer Associates, Inc.

Horn, R. (1987). Statistical methods for model discrimination. Applications to gating kinetics and permeation of the acetylcholine receptor channel. Biophys. J, 51(2), 255-263.

Jiang, Y., Lee, A., Chen, J., Cadene, M., Chait, B. T., & MacKinnon, R. (2002a). Crystal structure and mechanism of a calcium-gated potassium channel. Nature, 417(6888), 515-522.

Jiang, Y., Lee, A., Chen, J., Cadene, M., Chait, B. T., & MacKinnon, R. (2002b). The open pore conformation of potassium channels. Nature, 417(6888), 523-526.

Jiang, Y., Pico, A., Cadene, M., Chait, B. T., & MacKinnon, R. (2001). Structure of the RCK domain from the E. coli K+ channel and demonstration of its presence in the human BK channel. Neuron, 29(3), 593-601. doi:10.1016/s0896-6273(01)00236-7

Kong, C., Zeng, W., Ye, S., Chen, L., Sauer, D. B., Lam, Y., . . . Jiang, Y. (2012). Distinct gating mechanisms revealed by the structures of a multi-ligand gated K(+) channel. Elife, 1, e00184. doi:10.7554/eLife.00184

Lakowicz, J. R. (1999). Principles of fluorescence spectroscopy (J. R. Lakowicz Ed. 2nd ed.): Kluwer Academic/Plenum Publishers.

Lewis, J. H., & Lu, Z. (2019a). Energetics of angstrom-scale conformational changes in an RCK domain of the MthK K(+) channel. Nat Struct Mol Biol, 26(9), 808-815. doi:10.1038/s41594-019-0275-1

Lewis, J. H., & Lu, Z. (2019b). Integrating spatiotemporal features of a ligand-regulated, multi-state allosteric protein. Nat Struct Mol Biol, 26(9), 816-822. doi:10.1038/s41594-019-0276-0

Lewis, J. H., & Lu, Z. (2019c). Resolution of angstrom-scale protein conformational changes by analyzing fluorescence anisotropy. Nat Struct Mol Biol, 26(9), 802-807. doi:10.1038/s41594-019-0274-2

Lippert, L. G., Dadosh, T., Hadden, J. A., Karnawat, V., Diroll, B. T., Murray, C. B., . . . Goldman, Y. E. (2017). Angular measurements of the dynein ring revaeal a stepping mechanism dependent on a flexible stalk. Proc. Natl. Acad. Sci. U. S. A, 114, E4564-E4573.

Nakamura, T., Yamamuro, N., Stumpe, S., Unemoto, T., & Bakker, E. P. (1998). Cloning of the trkAH gene cluster and characterization of the Trk K(+)-uptake system of Vibrio alginolyticus. Microbiology, 144 (Pt 8), 2281-2289. doi:10.1099/00221287-144-8-2281

Ohmachi, M., Komori, Y., Iwane, A. H., Fujii, F., Jin, T., & Yanagida, T. (2012). Fluorescence microscopy for simultaneous observation of 3D orientation and movement and its application to quantum rod-tagged myosin V. Proc. Natl. Acad. Sci. U. S. A, 109(14), 5294-5298.

Pau, V. P., barca-Heidemann, K., & Rothberg, B. S. (2010). Allosteric mechanism of Ca2+ activation and H+-inhibited gating of the MthK K+ channel. J. Gen. Physiol, 135(5), 509-526.

Press, W. H., Teukolsky, S. A., Vetterling, W. T., & Flannery, B. P. (2007). Numerical Recipes: The art of scientific computing (W. H. Press, S. A. Teukolsky, W. T. Vetterling, & B. P. Flannery Eds. 3rd ed.). New York: Cambridge University Press.

The PyMOL Molecular Graphics System, Version 1.5.0.4 Schrödinger, LLC. (2015). http://www. pymol. org/. http://www.pymol.org/

Rao, S. T., & Rossmann, M. G. (1973). Comparison of super-secondary structures in proteins. J Mol Biol, 76(2), 241-256. doi:10.1016/0022-2836(73)90388-4

Rhoads, D. B., & Epstein, W. (1977). Energy coupling to net K+ transport in Escherichia coli K-12. J Biol Chem, 252(4), 1394-1401.

Rhoads, D. B., & Epstein, W. (1978). Cation transport in Escherichia coli. IX. Regulation of K transport. J Gen Physiol, 72(3), 283-295. doi:10.1085/jgp.72.3.283

Ritchie, T. K., Grinkova, Y. V., Bayburt, T. H., Denisov, I. G., Zolnerciks, J. K., Atkins, W. M., & Sligar, S. G. (2009). Chapter 11 - Reconstitution of membrane proteins in phospholipid bilayer nanodiscs. Methods Enzymol, 464, 211-231.

Roosild, T. P., Castronovo, S., Miller, S., Li, C., Rasmussen, T., Bartlett, W., . . . Booth, I. R. (2009). KTN (RCK) domains regulate K+ channels and transporters by controlling the dimer-hinge conformation. Structure, 17(6), 893-903. doi:10.1016/j.str.2009.03.018

Roosild, T. P., Miller, S., Booth, I. R., & Choe, S. (2002). A mechanism of regulating transmembrane potassium flux through a ligand-mediated conformational switch. Cell, 109(6), 781-791. doi:10.1016/s0092-8674(02)00768-7

Rowlett, V. W., Mallampalli, V., Karlstaedt, A., Dowhan, W., Taegtmeyer, H., Margolin, W., & Vitrac, H. (2017). Impact of Membrane Phospholipid Alterations in Escherichia coli on Cellular Function and Bacterial Stress Adaptation. J Bacteriol, 199(13). doi:10.1128/JB.00849-16

Sase, I., Miyata, H., Ishiwata, S., & Kinosita, K., Jr. (1997). Axial rotation of sliding actin filaments revealed by single-fluorophore imaging. Proc. Natl. Acad. Sci. U. S. A, 94(11), 5646-5650.

Schmidt, T. G., & Skerra, A. (2007). The Strep-tag system for one-step purification and high-affinity detection or capturing of proteins. Nat Protoc, 2(6), 1528-1535. doi:10.1038/nprot.2007.209

Schultz, S. G., & Solomon, A. K. (1961). Cation transport in Escherichia coli. I. Intracellular Na and K concentrations and net cation movement. J Gen Physiol, 45, 355-369. doi:10.1085/jgp.45.2.355

Shin, W. H., & Kihara, D. (2019). 55 Years of the Rossmann Fold. Methods Mol Biol, 1958, 1-13. doi:10.1007/978-1-4939-9161-7_1

Sosa, H., Peterman, E. J., Moerner, W. E., & Goldstein, L. S. (2001). ADP-induced rocking of the kinesin motor domain revealed by single-molecule fluorescence polarization microscopy. Nat. Struct. Biol, 8(6), 540-544.

Stewart, L. M., Bakker, E. P., & Booth, I. R. (1985). Energy coupling to K+ uptake via the Trk system in Escherichia coli: the role of ATP. J Gen Microbiol, 131(1), 77-85. doi:10.1099/00221287-131-1-77

Vieira-Pires, R. S., Szollosi, A., & Morais-Cabral, J. H. (2013). The structure of the KtrAB potassium transporter. Nature, 496(7445), 323-328. doi:10.1038/nature12055

Warshaw, D. M., Hayes, E., Gaffney, D., Lauzon, A. M., Wu, J., Kennedy, G., . . . Berger, C. (1998). Myosin conformational states determined by single fluorophore polarization. Proc. Natl. Acad. Sci. U. S. A, 95(14), 8034-8039.

Woody, M. S., Lewis, J. H., Greenberg, M. J., Goldman, Y. E., & Ostap, E. M. (2016). MEMLET: An Easy-to-Use Tool for Data Fitting and Model Comparison Using Maximum-Likelihood Estimation. Biophys J, 111(2), 273-282. doi:10.1016/j.bpj.2016.06.019

Ye, S., Li, Y., Chen, L., & Jiang, Y. (2006). Crystal structures of a ligand-free MthK gating ring: insights into the ligand gating mechanism of K+ channels. Cell, 126(6), 1161-1173.

Yuan, P., Leonetti, M. D., Hsiung, Y., & MacKinnon, R. (2012). Open structure of the Ca2+ gating ring in the high-conductance Ca2+-activated K+ channel. Nature, 481(7379), 94-97.

Zadek, B., & Nimigean, C. M. (2006). Calcium-dependent gating of MthK, a prokaryotic potassium channel. J. Gen. Physiol, 127(6), 673-685.

Zhang, H., Pan, Y., Hu, L., Hudson, M. A., Hofstetter, K. S., Xu, Z., . . . Zhou, M. (2020). TrkA undergoes a tetramer-to-dimer conversion to open TrkH which enables changes in membrane potential. Nat Commun, 11(1), 547. doi:10.1038/s41467-019-14240-9

Zhang, Y., Werling, U., & Edelmann, W. (2012). SLiCE: a novel bacterial cell extract-based DNA cloning method. Nucleic Acids Res, 40(8), e55. doi:10.1093/nar/gkr1288

Zhou, Y., Morais-Cabral, J. H., Kaufman, A., & MacKinnon, R. (2001). Chemistry of ion coordination and hydration revealed by a K+ channel-Fab complex at 2.0 A resolution. Nature, 414(6859), 43-48.